One Shell, Two Shell, Red Shell, Blue Shell: Numerical Modeling to Characterize the Circumstellar Environments of Type I Supernovae

by

Chelsea E. Harris

A dissertation submitted in partial satisfaction of the

requirements for the degree of

Doctor of Philosophy

in

Astrophysics

and the Designated Emphasis

in

Computational and Data Science and Engineering

in the

Graduate Division

of the

University of California, Berkeley

Committee in charge:

Professor Daniel Kasen, Chair
Professor Alex Filippenko
Professor Peter Nugent
Professor Per-Olof Persson

Summer 2018

One Shell, Two Shell, Red Shell, Blue Shell: Numerical Modeling to Characterize the Circumstellar Environments of Type I Supernovae

Abstract

One Shell, Two Shell, Red Shell, Blue Shell: Numerical Modeling to Characterize the Circumstellar Environments of Type I Supernovae

by

Chelsea E. Harris

Doctor of Philosophy in Astrophysics

University of California, Berkeley

Professor Daniel Kasen, Chair

Though fundamental to our understanding of stellar, galactic, and cosmic evolution, the stellar explosions known as supernovae (SNe) remain mysterious. We know that mass loss and mass transfer are central processes in the evolution of a star to the supernova event, particularly for thermonuclear Type Ia supernovae (SNe Ia), which are in a close binary system. The circumstellar environment (CSE) contains a record of the mass lost from the progenitor system in the centuries prior to explosion and is therefore a key diagnostic of SN progenitors. Unfortunately, tools for studying the CSE are specialized to stellar winds rather than the more complicated and violent mass-loss processes hypothesized for SN Ia progenitors.

This thesis presents models for constraining the properties of a CSE detached from the stellar surface. In such cases, the circumstellar material (CSM) may not be observed until interaction occurs and dominates the SN light weeks or even months after maximum light. I suggest we call SNe with delayed interaction SNe X;n (i.e. SNe Ia;n, SNe Ib;n). I performed numerical hydrodynamic simulations and radiation transport calculations to study the evolution of shocks in these systems. I distilled these results into simple equations that translate radio luminosity into a physical description of the CSE. I applied my straightforward procedure to derive upper limits on the CSM for three SNe Ia: SN 2011fe, SN 2014J, and SN 2015cp. I modeled interaction to late times for the SN Ia;n PTF11kx; this led to my participation in the program that discovered interaction in SN 2015cp. Finally, I expanded my simulations to study the Type Ib;n SN 2014C, the first optically-confirmed SN X;n with a radio detection. My SN 2014C models represent the first time an SN X;n has been simultaneous modeled in the x-ray and radio wavelengths.

"All we have to decide is what to do with the time that is given us."

Mithrandir, *The Lord of the Rings* by J.R.R. Tolkien

Contents

List of Figures

List of Tables

Acknowledgments

Much of this work was funded by the Department of Energy Computational Science Graduate Fellowship.

I'd like to thank the people in my life who gave me strength throughout my doctoral work. My parents, Jim and Terry, supported me so much even without knowing what the heck I was doing. They have infinite faith in me, and aren't afraid to Tell It Like It Is. Likewise with my dear friend Linda. And finally, my partner David has done all of my dishes and laundry and cooking and everything for the last few weeks while I put this together. So, please, no one tell him that I'm done – this is comfy living!

Finally, I have to acknowledge the "Managing Stress, Anxiety, and Depression" Skills Group offered for free through the University's Counseling and Psychological Services program. Throughout most of my doctoral work, I suffered severely from mental health issues. Coming in to this program, I simply did not have the coping mechanisms to handle – in a healthy way – the stress and anxiety brought on by the demands of this career and unforeseen challenges in my personal life. In my desperation to escape these overwhelming negative thoughts and feelings, I lapsed into extremely self-destructive behaviors. I knew it was a problem, but it was not until I reached out for professional help that I was able to develop a solution. I cannot emphasize enough how much my productivity and creativity improved after I learned how to overcome the worst of my anxious habits. If you are reading this and you are struggling with anxiety or depression, or if you put aside fulfilling personal relationships to cope with work stress, or habitually feel guilty or ashamed in association with your work, please seek professional help. You are not alone, you are not undeserving, and you can get better.

Chapter 1

Introduction: Welcome to the Jungle

Supernovae (SNe) are the light from exploding stars – now that the theory is well developed, the term "supernova" is used for the stellar explosion itself. But we do not know exactly *why* stars explode. This is a problem because nearly all the elements in our universe come from supernovae, and exploding stars carry mass out of their parent galaxies, and we use stellar explosions to measure the expansion history of the universe. So anything that can give us a handle on why supernovae occur and how diverse they are is something we want to investigate. The desire to get a handle on supernova progenitors is at the core of this thesis.

This work was shaped by the fact that in 2011 a Type Ia supernova (SN Ia) was *caught* crashing into (or as we say, "interacting with") a wall of circumstellar material (CSM). The search for CSM around SNe Ia had been arduous, spanning decades and filled with uncertainty; and here seemed to be the answer: the reason we had not observed interaction is not only that it prefers a rare type of SN Ia but also that the interaction is delayed, not prompt. But the theoretical infrastructure required to make sense of this event did not exist yet. So I launched onto a trajectory to break down the barriers that were limiting our ability to describe – or even *find* – supernovae with delayed interaction.

In this first chapter, I will describe the SN landscape – we will climb the mountains of SN classification, ford the streams of progenitor theory, and follow the rainbow of shock physics. Then I will describe how decades of searching for CSM around SNe Ia to discover their progenitors turned up a surprising dichotomy in SNe Ia that may be a strong hint to the viability of different progenitor channels. Finally I will compare the SN Ia picture with that of its hydrogen-free cousins, SNe Ibc. Branch and Wheeler (2017) and Alsabti and Murdin (2017) are two recent book reviews of supernovae that contain more detail on most of the topics I will cover.

We will see that a key principle in all this is that most SN research focuses on grouping SNe that look the same into "types" (trying to do this in a way that reflects important physical differences) and then hammering away at a model that can explain a given SN type. And that is essentially what I am trying to do with this thesis: hammer at delayed interaction supernovae.

1.1 The Current Supernova Classification System

The title "supernova" is given to any optical transient that rises and falls within about a month, whose spectra have broad line features indicating speeds of $\sim 10,000$ km s^{-1}, and whose peak luminosity is $\sim 10^{42}$ erg s^{-1}. Typically these are extragalactic sources, though their name is derived from the lower-energy Galactic events known as novae. As will be described in the next section, the observed properties of these transients – particularly their locations, inferred energy release, and the timescale of energy release – led to the deduction that they represent stellar eruptions in which new elements are synthesized and all (or most) of the star's mass is unbound from the system. But SNe come in many varieties that we call types or classes, and even within those are sub-classes and groups of even more similar events; Filippenko (1997) is an excellent review of the SN types.

In the beginning there were no supernova types, because the majority of SNe found looked the same. Supernovae were split into Types I and II by Minkowski (1941), based on a sample of only fourteen events. The reason for the split was spectroscopic: some SNe showed hydrogen, while others did not. The more abundant class (nine of the fourteen) was dubbed "Type I." SNe I were most common because they are intrinsically brighter and can occur in the old stellar populations of high-mass galaxies, making them more likely to be discovered in targeted surveys. The Type I class was extremely homogeneous, making it a promising avenue for measuring cosmic expansion to farther distances than Cepheid variable stars allowed.

Like most things introduced in the 1980s, the remaining supernova classes are an annoying but inevitable consequence of rapid technological advancement: with digital spectra, astronomers could quantify more subtle differences between events; and with computers, they could do sophisticated comparisons between real and synthetic spectra. The division of SNe I into "Ia" and "Ib" is often attributed to Panagia (1985), who recognized that SNe I in late-type galaxies had a much higher luminosity dispersion than those in early-type galaxies and much redder colors [1]; but the naming scheme itself was presented in a slightly later study of the near-infrared color evolution (Elias et al., 1985). The definition we use today for SNe Ib – lacking hydrogen, but having helium – is the result of radiation transport modeling efforts to explain SN Ib spectra (Branch and Nomoto, 1986). Wheeler and Harkness (1986) identified the Type Ic division, in which "the spectrum consists essentially entirely of Fe moving at -20,000 km/s," without the intermediate-mass elements seen in SNe Ia. Shortly after, the SN IIb class was proposed as a label for objects that intially resemble SNe II but evolve into an SN Ib (Filippenko, 1988).

The first classification of interacting supernovae was in the 1990s. The class "IIn" was proposed by Schlegel (1990) to describe supernovae with narrow hydrogen emission lines (both a very narrow component $\lesssim 100$ km s^{-1} and an intermediate width emission component of ~ 1000 km s^{-1}) and a strong blue thermal continuum. A newer related class, SNe Ibn, are

[1] They say, "it is ... likely that spiral galaxies contain a sub-class of Type I SNe which does not exist in early type galaxies," and suggest ignoring all SNe I in late-type galaxies for cosmological measurements.

like SNe IIn except that these SNe have no signs of hydrogen, instead having narrow *helium* emission lines (Matheson et al., 2000; Pastorello et al., 2007). The class of interacting SNe Ia, a sub-group of SNe IIn, was only recently defined, labeled SNe Ia-CSM (Silverman et al., 2013a).

Aside from delineating the nomenclature, it is important to note that *most* SN classification criteria are based on compositional differences indicated by the broad absorption lines in their optical spectra near maximum light. It is also important to remember that Type I SNe do not have hydrogen in their spectra; they are often called "stripped envelope" supernovae. These SNe are excellent for studying pre-explosion mass loss because the hydrogen in their spectra must trace the CSM.

1.1.1 91T-like Type Ia Supernovae

An important sub-group of SNe Ia in the discussion of CSM is often called "91T-like." Since there is currently no universal definition of this group, here we describe the distinguishing features of SN 1991T and codify the use of the "91T-like" label in this work. This group has three distinguishing characteristics from normal SNe Ia: their spectra, photometry, and host environments.

The primary feature of 91T-likes is spectroscopic. A normal SN Ia spectrum evolves from being dominated by features of intermediate-mass elements (e.g., Si, Mg, Ca) near photometric peak to those of iron-peak elements (e.g., Fe, Co) by the nebular phase (Branch et al., 1993). SN 1991T deviated from normal primarily in that its early-time spectrum was dominated by Fe III, its Si II "6150 Å" (blueshifted 6355 Å line) and "5800 Å" (blueshifted 5978 Å line) were very shallow, and it lacked Ca H&K absorption (Filippenko et al., 1992; Phillips et al., 1992). However, it evolved to resemble Branch-normal SNe Ia by three weeks after maximum light (approximately five weeks after explosion). SN 1999aa is like SN 1991T except it did *not have* the strange absence of Ca H&K that SN 1991T did (Garavini et al., 2004). This event is sometimes considered intermediate between normal and SN 1991T because it evolved to a normal spectrum earlier. Using radiation transport calculations, Nugent et al. (1995) discovered that these differences could be attributed primarily to a temperature difference between 91T-like and normal SNe Ia, due to more ^{56}Ni production.

The second difference is photometric. SN 1991T was more luminous than normal SNe Ia and its light curve (luminosity over time) declined more slowly; but it obeys the so-called "Phillips relation," allowing its use for cosmology (Phillips, 1993). This is true of SN 1999aa as well. Based on photometric classification, 91T-like SNe constitute $\sim 10\%$ of all SNe Ia compared to the 70% that are Branch-normal (Li et al., 2011).

The final distinguishing trait of SN 1991T, SN 1999aa, and others like them is that they prefer younger stellar populations, i.e., low-mass host galaxies, or the outskirts of massive spirals.

In this work, the spectroscopic definition will be predominant: a SN is "91T-like" if its spectrum near maximum light is best matched by SN 1991T *or* SN 1999aa. If no spectrum near maximum light is available, the luminosity and decline rate of the SN light curve provide

secondary evidence that the event is "91T-like." Note that if one wanted to define the class narrowly has being Ca-deficient like SN 1991T, a spectrum is *required*. The association with a younger stellar population based on the host-galaxy morphology and global properties is not considered a criterion for the classification; rather, it is more interesting that 91T-like SNe Ia reside in such hosts.

1.1.2 Type IIn and Ia-CSM Supernovae

The radiation signatures of interaction will be discussed in §1.3 and §1.4, but here I would like to remark on how I will be using the SN IIn and Ia-CSM labels.

SNe IIn have slowly evolving spectra, a strong blue continuum, and narrow – though not necessarily unresolved – Hα emission lines, sometimes with broad Lorenzian wings, indicating that this light is from high-density gas at much lower speeds than the SN ejecta. The optical depth of the CSM is so high that the broad absorption lines of the underlying SN – normally used to determine the SN type – are smothered. For this work an important specification for SNe IIn is that they show these spectroscopic features from the earliest times of observation. SNe IIn represent only the most dense circumstellar environments; yet they account for 5% of all supernovae in a given volume (being 9% of all SNe II, and SNe II being 57% of all SNe; Li et al., 2011). A prototypical SN IIn is SN 1988Z (Stathakis and Sadler, 1991).

SNe Ia-CSM in this work will refer to SNe IIn with underlying signatures of an SN Ia spectrum. In a way this is a sub-class of SN IIn, but Leloudas et al. (2015) determined that one can tell when an SN Ia spectrum is present. I use the SN Ia-CSM label as defined in Silverman et al. (2013a), thus including both prompt and delayed interaction cases (see below). It does not, however, include SNe Ia with time-variable or blueshifted narrow sodium absorption features (§1.4). The relative occurrence rate of SNe Ia-CSM is unknown. Partly this is because the label includes delayed interaction cases whose rate is unknown.

1.1.3 Type "X;n" Supernovae

In this thesis I define a new label appropriate to the type of supernovae I study: those with detached CSM whose strong interaction signatures are only seen weeks or months after optical maximum light. For this phenomenon I chose the grammatically appropriate label of SN X;n, with "X" being a placeholder for the maximum light SN type, e.g. SN Ia;n. I only hope most astronomers appreciate Charles Dickens, and can regard the semicolon fondly. Note that while "n" stands for "[n]arrow lines," interaction need not be identified through lines < 100 km s^{-1} but can simply have $\lesssim 5,000$ km s^{-1} lines (sometimes called "intermediate-width lines"). When discussing these events in a general way, e.g., for the purposes of observational strategies, I use the label SN X;n.

The fact that observations near maximum light do not (or are unlikely to) reveal the presence of CSM for SNe X;n results in three key differences between SNe X;n and promptly-interacting SNe. First, the SN properties, such as ejecta mass, can be determined from observations made within a month after explosion. Second, the rate of SNe X;n is much

more difficult to determine than for any of its associated classes; and as a corollary to this point, unique observational strategies are required to find these objects. Finally, it is unclear what the *physical* connection is between promptly-interacting SNe and SNe X;n, as the CSM may be shaped by different processes.

The prototypical SN Ia;n is PTF11kx, whose transformation was clearly observed spectroscopically and photometrically; in this case the interaction occurred about a month after maximum light, placing the CSM at $\sim 10^{16}$ cm (Dilday et al., 2012). And in fact SN 2002ic, often regarded as the original SN Ia-CSM, was an SN Ia;n. Its light curve was initially identical to that of a 91T-like SN Ia, but about a week after maximum light it diverged and subsequent spectra confirmed signatures of interaction (Wood-Vasey et al., 2004).

1.2 The Progenitors of Type I Supernovae

Even earlier this year, I was at a conference and an observer posed the question to SN Ia theorists, "What is the observable that I should go after that will tell me what the progenitor was?" It is literally the Million Dollar Question.

We know what supernovae are at the simplest level. Hoyle and Fowler (1960) laid out how gravitational collapse and degenerate gas instabilities can trigger the unbinding of a star. Colgate and White (1966) explored the nucleosynthesis of heavy elements in the explosion, and Colgate and McKee (1969) linked the exponential decline of SNe I light curves to the decay of ^{56}Ni. (Non-radioactive models worked well for SNe II, whose light curves are powered by recombination of hydrogen in their extensive, expanding envelopes.) The occurrence of SNe I in old stellar populations led Finzi and Wolf (1967) to hypothesize that these come from WDs, a hypothesis solidified by simulation work by K. Nomoto and S. Woosley in particular through the 1980s. Most SNe I in a magnitude-limited sample are SNe Ia, which can occur in young or old stellar populations. When SNe I were split into SNe Ia, Ib, and Ic, the SNe Ib and Ic were of similar luminosity to SNe II and found only in young stellar populations, motivating their association with massive stars and the core-collapse mechanism.

In this section, I will describe the main competing hypotheses for which star systems create SNe Ia, Ib, and Ic. The general theme is that mass loss and mass transfer are important for these SNe, which is why the circumstellar environment is so informative. For SNe Ia, if the companion is a main sequence (MS), red giant (RG), or helium star at the time of explosion, there *will* be hydrogen or helium in the vicinity of the SN: all MS and RG stars have hydrogen-rich winds and the impact of the SN ejecta with the star will throw mass off as well. For SNe Ibc, the structure of the CSM gives the history of how the outer hydrogen and helium envelopes were stripped from the star – is it a massive star process, or a binary process?

1.2.1 Type Ia Supernovae

SNe Ia were long thought to be the explosions of carbon-oxygen white dwarfs (CO WDs), the endpoints of solar-mass stars. These stars are very old, naturally explaining how these SNe can occur in old stellar populations; they also have the unique properties of being carbon-rich and supported by electron degeneracy pressure. When carbon ignites, a thermonuclear flame front develops and releases a great deal of energy into the star; the degenerate gas will not expand enough to stop the burning front, so runaway burning is possible. The nuclear burning produces enough energy to completely unbind the star; there is no compact remnant from an SN Ia as in CC SNe. The decay of radioactive isotopes, specifically ^{56}Ni, releases gamma rays that thermalize in the expanding ejecta, emerging primarily as optical photons. The association of CO WDs with SNe Ia was recently confirmed by SN 2011fe (Nugent et al., 2011; Bloom et al., 2012) and SN 2014J (Diehl et al., 2015; Churazov et al., 2015).

The outstanding problem for SNe Ia is that they require the CO WD to be in a binary system, and we do not know what the companion is. If the CO WD is near the Chandrasekhar mass so that it is intrinsically unstable and thus explodes, it must grow from its nascent 0.6-0.9 $M_\odot$ to nearly 1.4 $M_\odot$.[2] This can be done by a long phase of mass transfer from a companion to the CO WD, with burning on the WD surface to create more carbon, or through a merger with another CO WD. Whereas if the CO WD has lower mass, closer to 1 $M_\odot$ (a "sub-Chandrasekhar" model), a surface detonation at an accretion hotspot is needed to trigger a central detonation ("double-detonation" models; Arnett, 1968), thus again requiring a companion for explosion.

There is an enormous theoretical range of possible SN Ia companion stars, but the companions are associated with particular mass-transfer mechanisms. RG, MS, and helium star companions would donate mass through Roche-lobe overflow (RLOF) or as mass incidentally accreted from their wind (Branch et al., 1995; Shen and Moore, 2014). CO WD companions are associated with violent mergers, where ignition typically occurs at the point of contact between the stars. Similar to the double-WD merger scenario is the one in which the CO WD is viscously dragged into the center of a post-AGB (asymptotic giant branch) star and merges with its degenerate core (Soker, 2013). Scenarios in which the companion is a non-degenerate star are called "single degenerate" (SD) and those with a degenerate star "double degenerate" (DD).

An interesting consideration for the SD channel is that mass transfer is rarely steady. In fact, a long-standing problem with this channel is that for most accretion rates the process is unstable and creates novae. Whether the novae necessarily take away more material than was accreted, thus preventing mass growth, is an open question. Models of novae place the mass ejected per outburst at only $\sim 10^{-6}$ $M_\odot$; but novae can be recurrent and thus build up many times this mass around the progenitor (Moore and Bildsten, 2012). Regardless of whether the eruption is due to the nova mechanism, novae are an example of eruptive mass loss expected from the SD channel that can create detached CSM.

[2]It is important to keep in mind that the CO WD explodes *before* reaching the Chandrasekhar limit in this scenario – achieving the limit would collapse the WD into a neutron star.

1.2.2 Type Ibc Supernovae

Although spectroscopically very similar to SNe Ia, Type Ic were linked to Types II and Ib due to the association with young stellar populations and the similar luminosities of SNe Ib and Ic. SNe Ibc are explosions from massive stars, core-collapse (CC) SNe. There is likely a continuum between SNe II, IIb, Ib, and Ic, with each class representing a further-stripped version of the one preceding it.

CC SNe occur in association with the collapse of a massive star core into a neutron star (NS) or black hole (BH). The mechanism for driving the explosion is unknown. Initially it was proposed that the stellar envelope would fall into the void created by the CC and reach conditions for a thermonuclear explosion (Hoyle and Fowler, 1960), but this explanation is now unfashionable. Instead, the explosion is typically linked to a shock sweeping through the envelope, energized by either neutrinos from the proto-NS or a magnetic field (e.g., Couch, 2017, for a review).

For SNe Ibc, the progenitor question is how these massive stars lost their outer envelopes. If these SNe come from isolated stars, the stripping of the envelope is either caused by winds or yet unidentified eruptive instabilities. In the wind scenario, the progenitors of SNe Ibc would be Wolf-Rayet (WR) stars, which are more massive than the red supergiant progenitors of normal SNe II. However another possibility is that these CC SNe represent those that occur in binary star systems, and the companion is responsible for stripping the envelope.

Podsiadlowski et al. (1993) presents seminal work on binary population synthesis that studies mass transfer in massive star binaries to show that RLOF can strip massive stars of their outer envelopes to produce SNe Ib. The importance of this process is dependent on how often massive stars are near enough to their companion to undergo mass transfer, which relies on our understanding of stellar multiplicity and the distribution of orbital parameters. Sana et al. (2012) showed that most O-type (massive) stars are in mass-transfer binaries, and 33% will have their envelope stripped by their companion. This is in agreement with the finding that 34% of CC SNe are of Types IIb, Ib, or Ic (Li et al., 2011). In the particular case of Type IIb SN 1993J, the presence of a binary companion is favored based on modeling as well as direct imaging (Smartt, 2009).

The probable importance of binary processes in creating SNe Ibc is one of the main reasons I became interested in these events. While the explosion mechanism is distinct, these special CC SNe may be another way to investigate binary mass transfer instabilities relevant to SNe Ia.

1.3 Shocks and Their Radiation Signatures

The primary method for constraining the CSE of an SN is by looking for signatures of the impact of the ejecta with the CSM. Interpreting these signatures relies on models of the propagation of a shock wave through the CSM and SN ejecta.

A very nice review of non-relativistic shocks can be found in Jones and Ellison (1991),

as well as nearly any book on astrophysical hydrodynamics. In this section I will review some of the basic hydrodynamics of shocks so that we can understand why they produce panchromatic signatures. The main hydrodynamic takeaways are that shocks convert bulk kinetic into internal energy and amplify magnetic fields. The effects on the observed radiation are increased brightness compared to a non-interacting SN, unique signatures of a relativistic, non-thermal electron population, and the reprocessing of high-energy shock emission by outlying gas. Because the radiation energy comes from conversion of mechanical energy, the luminosity of a shock depends on the hydrodynamic evolution of the shock front.

1.3.1 Strong Shock Hydrodynamics

By introducing a perturbation to the density, pressure, or velocity in the hydrodynamic equations, linear analysis reveals that such disturbances are communicated through the gas via waves. The Mach number ($\mathcal{M}$) is the ratio of the wave propagation speed to the local sound speed (c_s). It is possible for waves to travel faster than c_s, creating a discontinuity between the post-shock and pre-shock gas density and velocity; such waves are called shocks. Gas that has not yet been shocked is called "upstream" or "pre-shock" gas and that which has been shocked is "downstream" or "post-shock." Treating a shock wave as a discontinuity and analyzing the hydrodynamic equations then produces the Rankine-Hugoniot relations, which for an adiabatic (not cooling) shock are

$$\rho_u v_u = \rho_d v_d \tag{1.1}$$

$$\rho_u v_u^2 + p_u = \rho_d v_d^2 + p_d \tag{1.2}$$

$$\frac{1}{2}v_u^2 + \mathcal{E}_u + \frac{p_u}{\rho_u} = \frac{1}{2}v_d^2 + \mathcal{E}_d + \frac{p_d}{\rho_d} \tag{1.3}$$

where ρ is the mass density, v the speed, p the pressure, and $\mathcal{E}$ the internal energy per unit mass of the gas; the subscript u indicates upstream gas and the subscript d is for downstream gas.

If a gamma-law equation of state is assumed,

$$p \propto \rho^{-\gamma_{\rm ad}}, \tag{1.4}$$

then these equations can be manipulated to show that the compression ratio in the case of a strong shock is

$$\frac{\rho_{\rm post}}{\rho_{\rm pre}} = \frac{\gamma_{\rm ad}+1}{\gamma_{\rm ad}-1}\ . \tag{1.5}$$

This factor is called the "compression ratio." For gas dominated by relativistic particles, $\gamma_{\rm ad} = 4/3$ and the compression ratio is 7; for non-relativistic gas $\gamma_{\rm ad} = 5/3$ and the ratio is 4. In my work, since I assume low densities with inefficient photon trapping and relativistic particle energy contribution of only 10%, I use $\gamma_{\rm ad} = 5/3$.

Because shocks are powered by ram pressure (ρv_s^2) and because the size of an emitting/absorbing region is a key parameter for luminosity calculations, knowing the radius of

a shock over time is crucial for studies of interaction. One of the most popular solutions to this problem is the Chevalier self-similar solution (Chevalier, 1982a), sometimes called the "mini-shell model" because the shocked region is very thin. The assumptions when using this solution are that (1) the ejecta involved in the interaction have $\rho \propto r^{-n}$ with $n \geq 5$, (2) the CSM has $\rho \propto r^{-s}$ with $0 \leq s < 3$, and (3) the time is well after the start of interaction ($t \gg t_{\rm imp}$). This solution gained extreme popularity when it was found to be a good descriptor of radio supernovae (core-collapse) and to support the hypothesis that the CSM in these cases is like a stellar wind. The solution applies in this case because a constant mass-loss rate $\dot{M}$ from a wind of speed v_w establishes a CSM density profile

$$\rho_w = \frac{\dot{M}}{4\pi v_w} r^{-2} \ . \tag{1.6}$$

The fact that the self-similar results are analytical made the model very flexible, and infrastructure was relatively rapidly developed for fitting radio light curves that could even account for multiple absorption processes.

I must stress here that it is impossible to interpret radiation from interaction without a hydrodynamic model of the shock evolution. This is a large part of the reason why the easy to use, though asymptotic, mini-shell model has found such wide success. But because it is an asymptotic solution, it cannot be applied to SNe X;n where the interaction is observed shortly after it begins and can transition between different density profiles in both the CSM and ejecta.

1.3.2 Electron Acceleration in Shocked Gas

An important aspect of shocked regions is that they generate relativistic particles (Jones and Ellison, 1991). Originally to determine the origin of cosmic rays, physicists discovered that scattering with magnetic fields will accelerate particles into power-law distributions and up to relativistic speeds (Fermi, 1949). Observations of these particles (see next section) seem to require that the magnetic fields in shock regions are somehow substantially amplified, though the process for achieving this is not fully understood and may be different at different stages of the interaction. For example, the parameterization I use is that the magnetic field energy density is proportional to the gas energy density, which implicitly assumes the magnetic field has been amplified by turbulence (Chevalier, 1996).

The parameterization that I use for the non-thermal population is the following. I assume a fraction $f_{\rm NT}$ of electrons are accelerated into a non-thermal power-law distribution

$$dn_{e,{\rm NT}} = C\gamma^{-p} d\gamma, \tag{1.7}$$

with γ the electron Lorentz factor. Data for stripped-envelope core-collapse supernovae favor $p \approx 3$ (Chevalier and Fransson, 2006), while $p = 2$ is expected for a gas with $\gamma_{\rm ad} = 5/3$ (Jones

and Ellison, 1991). The normalization C is given by

$$f_{\rm NT} n_e = n_{e,\rm NT} = \int_{\gamma_{\rm min}}^{\infty} C\gamma^{-p} d\gamma \tag{1.8}$$

$$\Rightarrow C = n_{e,\rm NT}(p-1)\gamma_{\rm min}^{p-1} . \tag{1.9}$$

If the energy density in relativistic electrons (u_e) is a fraction ϵ_e of the gas energy density ($u_{\rm gas}$), then

$$u_e \equiv \epsilon_e u_{\rm gas} = \int_{\gamma_{\rm min}}^{\infty} (\gamma m_e c^2)\ C\gamma^{-p} d\gamma . \tag{1.10}$$

which we can combine with Equation 1.9 to show that

$$\gamma_{\rm min} = \frac{u_e}{n_{e,\rm NT} m_e c^2} \left(\frac{p-2}{p-1} \right) . \tag{1.11}$$

For the special case $p = 3$ which I assume in my work,

$$\gamma_{\rm min} = \frac{1}{2} \frac{u_e}{n_{e,\rm NT} m_e c^2}, \tag{1.12}$$

$$C = \frac{1}{2} n_{e,\rm NT} \left(\frac{u_e}{n_{e,\rm NT} m_e c^2} \right)^2 . \tag{1.13}$$

1.3.3 Radiation from Shocks

It is the radiation from a shock that we must observe and use to determine, from a hydrodynamic model, the conditions of the CSM. Amazingly, shocks radiate across the electromagnetic spectrum, providing ample footholds for our understanding. Radiation tied to the relativistic electron population is the clearest indicator that the radiation comes from a shock, and is therefore the gold standard of interaction. But shocks also produce high-energy emission, both from the relativistic populations and the high temperatures, that the SN does not; so indicators of a high-energy radiation field are also a good indicator that interaction is occurring. The final indicator of shock powering is simply the increased continuum emission at optical wavelengths. To complete this section I will review the radiation processes associated with shocks, and provide the equations I (and other authors) use to calculate the emission and absorption from these processes. These processes are illustrated in Figure 1.1. The next section will then describe observational efforts to look for any of these processes at work in SNe Ia, and how that compares to the case of SNe Ibc.

Synchrotron

In the synchrotron process, relativistic electrons circling in a magnetic field radiate; it is the relativistic version of cyclotron radiation. As in cyclotron emission, each electron traces a

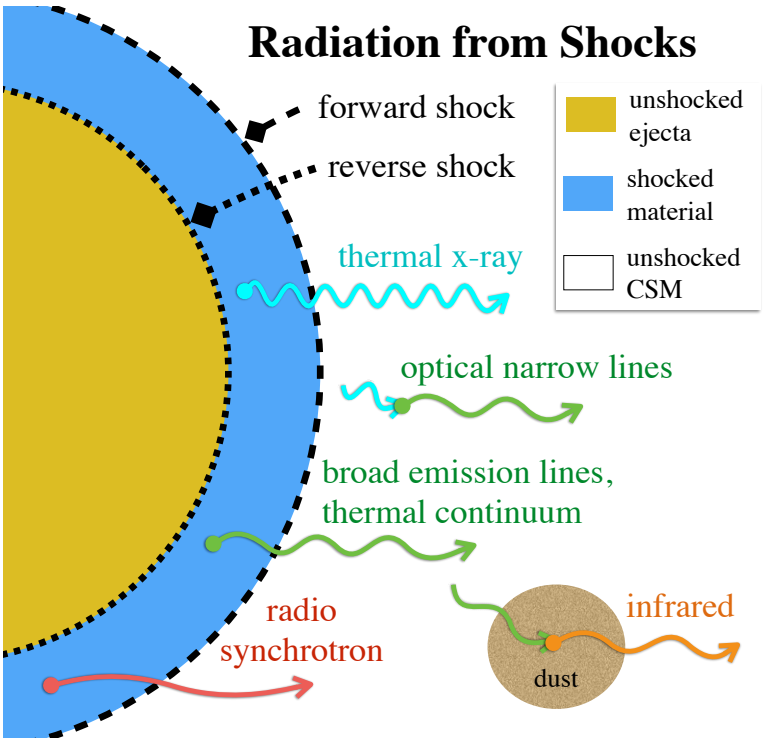

Figure 1.1: A simple reference guide for the radiation processes important for SNe X;n. Radio and x-ray emission are clean tracers of the shocked gas. Note that radio emission may come from the thermal free-free process, and x-ray emission may come from synchrotron or inverse Compton processes; the labels in the diagram only indicate the processes most commonly important for interacting supernovae.

circular path in the magnetic field, with a Larmor frequency

$$\nu_B = \frac{2\pi q_e B}{\gamma m_e c} \, , \tag{1.14}$$

with q_e the electron charge, B the magentic field amplitude, γ the Lorenz factor, m_e the electron mass, and c the speed of light. The characteristic photon frequency when relativistic beaming is accounted for is

$$\nu_c = \gamma^2 \nu_B \, . \tag{1.15}$$

The power emitted by a single electron through this process is

$$P_{\rm sync} = \frac{4}{3} \sigma_T c \beta^2 \gamma^2 u_B \, , \tag{1.16}$$

with σ_T the Thomson scattering cross section, $\beta = v/c$ the normalized electron speed, and u_B the magnetic field energy density. In general, the magnetic field energy density is

$$u_B = \frac{B^2}{8\pi} \tag{1.17}$$

and in my work I assume the magnetic field is created by turbulence in the gas (even only on microscopic scales) such that

$$u_B = \epsilon_B u_{\rm gas} \ . \tag{1.18}$$

The emission coefficient – which for reference as cgs units erg s^{-1} cm^{-3} Hz^{-1} str^{-1} – for a power-law population of electrons (Equation 1.7), with the simplifcation $\beta \approx 1$, is

$$j_\nu(\nu > \nu_B) = \frac{\sigma_T c}{6\pi}\ C\ u_B\ \nu_B^{-1}\ \left(\frac{\nu}{\nu_B}\right)^{(1-p)/2} \ , \tag{1.19}$$

which for $p = 3$ is simply

$$j_\nu(\nu > \nu_c \mid p = 3) = \frac{\sigma_T}{12\pi m_e^2 c^3}\ \epsilon_e^2\ \epsilon_B\ n_e^{-1}\ u_{\rm gas}^3\ \nu^{-1} \ . \tag{1.20}$$

The inverse absorption process, synchrotron self-absorption (SSA), has an associated extinction coefficient as given by Rybicki and Lightman (1979):

$$\alpha_{\rm SSA} = \frac{\sqrt{3} q_e^3}{8\pi m_e}\left(\frac{3q_e}{2\pi m_e^3 c^5}\right)^{p/2} C_E (B\sin\theta)^{(p+2)/2} \Gamma\left(\frac{3p+2}{12}\right)\Gamma\left(\frac{3p+22}{12}\right)\nu^{-(p+4)/2} \ , \tag{1.21}$$

where Γ is the gamma function and C_E is from $n(E) = C_E E^{-p} dE$ and is thus related to the C of Equation 1.9 by $C_E = (mc^2)^{p-1} C$. The $\sin\theta$ term represents the relative orientation of the electron and magnetic field; in our situation, we expect both the magnetic fields and the electron velocities to be randomly oriented and we adopt the angle-averaged value $\langle \sin\theta \rangle_\theta = 2/\pi$.

Inverse Compton

Inverse Compton emission represents photons that have gained energy by scattering off of electrons, and thus requires electrons to have similar energies to the incident photons (otherwise the photons will primarily give energy to the electrons, the Compton scattering process). SN photons are primarily at optical energies of $\sim 1keV$ and thus the scattering requires a relativistic electron population. This process of electrons scattering off an electromagnetic field is similar to synchrotron radiation; and in fact the power from a single scattering in the inverse Compton process is

$$\frac{P_{\rm comp}}{P_{\rm sync}} = \frac{u_B}{u_{\rm ph}} \ , \tag{1.22}$$

where $u_{\rm ph}$ is the photon energy density. Typically this process is treated in a more refined way than just supposing the above. Or one can find a treatment of multiple scatterings for instance in Fransson (1982).

Inverse Compton emission is important for SN interaction that occurs while the SN is still bright: the relativistic electrons in the shock regions energize the optical ($\sim$ eV) photons from the SN to x-ray ($\sim$ keV) energies. At early times, it can be an efficient coolant for

the gas and source of x-rays. But for the work I do, which focuses on times after SN peak brightness, inverse Compton emission is unimportant. I will mention however that the radiation toolkit I developed during my thesis work (§2) includes a calculator for optically thin inverse Compton scattering, calculating the inverse Compton emission from an input electron energy spectrum and photon energy spectrum using a random rejection scheme.

Free-Free (Bremsstrahlung)

Free-free radiation or Bremsstrahlung (literally "braking radiation") is produced by free electrons having their course altered by surrounding ions but maintaining their freedom. The change in direction is acceleration and thus the Larmor formula tells us again that a photon is produced.

The angle-integrated emissivity of free-free emission of thermal electrons, with the relativistic approximation for high temperatures, is

$$\epsilon_{\rm ff} = 1.43 \times 10^{-27}\ Z^2 n_I\ n_e\ T^{1/2}\ \bar{g}_B \left(1 + 4.4 \times 10^{-10} T\right) \tag{1.23}$$

in cgs units (Rybicki and Lightman, 1979). For the gaunt factor, I use the thermally averaged value for each ν and T as calculated by van Hoof et al. (2014).

The absorption is

$$\alpha_{\rm ff} = 0.018 Z^2 n_e n_i \nu^{-2} T^{-3/2} \bar{g}_{\rm ff} \quad . \tag{1.24}$$

This equation neglects the non-thermal approximation because it is the external, cold CSM that will absorb via free-free.

Atomic Lines

Atomic lines are in principle an incredibly important diagnostic for interaction, but are in practice difficult to use precisely. Typically when we talk about atomic lines we mean bound-bound transitions: the movement of an electron from one state in the potential field of a nucleus to another, with the energy transfer mediated by photons. Calculating the strength of a given atomic line, however, requires knowing the population density of each atomic level, the density distribution of free electrons, the density of each ion species, and the photon energy distribution. Here I must trust that my reader has enough familiarity with radiation processes to know what a headache those various distributions can pose – providing a *brief* summary is, in my opinion, impossible. Instead I will point out what we gain by the calculation.

Compositional information is arguably the most important. In SNe I, the appearance of hydrogen emission is clearly tied to the presence of CSM. In the case of SNe Ia or Ic, the hydrogen emission must be tracing the CSM itself. For SNe Ib, it is important to determine whether the SN was actually an SN IIb, with some of its hydrogen envelope intact; if so, the hydrogen emission may be coming from the highest-velocity ejecta.

The calculation of atomic lines, particularly the ratio of line strengths, is also a sensitive probe of the gas temperature and density. The detection of lines that require different

temperatures and densities can be used to indicate the radial profile of the gas. Atomic line calculations assuming photoionization and radiative recombination (based on a Stromgren sphere) have been explored in several works for SNe II (Fransson, 1984b,a; Chevalier and Fransson, 1994)

Finally, atomic lines can trace asphericity much better than continuum emission can (when polarization measurements are lacking). The shape of a line profile changes depending on the gas speed, extent, and equatorial concentration. For example, Chugai and Danziger (1994) used the Hα line of SN 1988Z to argue that the wind CSM in this event was clumpy.

Dust Heating

If there is dust around a SN, whether circumstellar or interstellar, the SN light will irradiate and heat it. The temperature that the dust reaches depends on the luminosity of the source, so this is a window into the luminosity of the SN; in the case of an interacting SN, it records the luminosity of interaction. The convenient aspect of this probe is that because the dust is so far from the SN, it has a large light-crossing time and the signal can be seen for a long time. The use of dust emission to describe CSM and constrain dust properties is described very well in Fox et al. (2013).

1.4 Searches for Circumstellar Material in Type Ia Supernovae

Now I will describe the historical efforts to constrain the presence of CSM in SNe Ia. In addition to the research that had been completed by the time I started my PhD, I will include many interesting studies published only in the last few years. At the end I will discuss the picture for SNe Ibc, which show many of the interaction signatures that SNe Ia lack.

Throughout this section I will highlight a common theme: observations have not been appropriate to searching for short-duration and/or delayed interaction in 91T-like SNe Ia. There are several reasons for this: theory was not saying there *ought* to be an island of CSM at $\sim 10^{16}$ cm; without models of the interaction it was hard to find or use Type Ia;n SNe; 91T-like SNe Ia are only $\sim 10\%$ of the population, and many investigation paths require nearby SNe so the statistics are against finding a substantial number of them; efforts have generally focused on the prize of discovering the progenitors of *normal* SNe Ia due to concerns over accurate cosmology; and frankly, Nugent et al. (1995) quelled initial fears that 91T-likes and normal SNe Ia had different progenitors in the first place. Yet I must point out that many of the studies in this seciton were done after SN 2002ic was in the mix and after PTF11kx had confirmed SN 2002ic as a 91T-like SN Ia and after Leloudas et al. (2015) had been published; so I think there should at least be some reprimand for not labeling 91T-likes in searches for CSM around SNe Ia published after 2012.

1.4.1 Radio

Radio synchrotron emission is one of the gold standards for interaction, being necessarily the result of an accelerated electron population unique to shock regions. However, it requires events that are relatively nearby: as a rule of thumb, < 300 Mpc for any hope, but the closer the better.

Efforts to find radio emission in SNe Ia, all resulting in non-detections, are reported in such works as Boffi and Branch (1995), Eck et al. (1995), Panagia et al. (2006),Chomiuk et al. (2012),Pérez-Torres et al. (2014), and most recently Chomiuk et al. (2016).

As occurring before my work, all of these non-detections have been interpreted in the framework proceeding from Chevalier (1982a) to limit the density of a stellar wind (Equation 1.6 – particularly, a slow, dense RG wind. I will quote the limits given for $\epsilon_B = 0.1$. Assuming a wind speed of 10 km s^{-1}, Panagia et al. (2006) limit (at 2σ confidence) the wind mass-loss rate to $\dot{M} < 10^{-6}\ M_\odot\ \mathrm{yr}^{-1}$ for 26 normal SNe Ia; for SN 1991T (at 28 days), their limit is $\dot{M} < 10^{-7}\ M_\odot\ \mathrm{yr}^{-1}$. The Chomiuk et al. (2016) 3σ limit is that $< 10\%$ of normal SNe Ia can have symbiotic progenitors (RG companions), and for SN 2012cg, the authors report that for a 100 km s^{-1} wind, the mass-loss rate must be $\dot{M} \lesssim 5 \times 10^{-9}\ M_\odot\ \mathrm{yr}^{-1}$. Unfortunately, the only 91T-like SN Ia in their sample was SN 1991T itself. For SN 2011fe, the limit is $\dot{M} \lesssim 6 \times 10^{-10}\ M_\odot\ \mathrm{yr}^{-1}$ (Chomiuk et al., 2012).

The work of Chomiuk et al. (2012) was particularly inspiring to me because the authors attempted to calculate the probability that they could have missed an interaction with a thin, low-mass nova shell. They were forced to assume a particular nova shell structure and could only approach the problem crudely because no general model of the interaction existed. Yet they put the probability of detection at only 30%. This was one of the earliest signs to me that nova shell interaction modeling had to be done. I have already mentioned how stringent a limit the authors were able to put on a wind; I wanted the same kinds of limits for a nova shell.

1.4.2 X-ray

The second gold standard for interaction is x-ray emission. At early times in particular, this is dominated by the inverse Compton process and therefore traces the relativistic population. At later times, thermal free-free emission is the dominant process but can still be used to constrain the gas temperature and density.

Normal SNe Ia have never been detected in x-rays (Margutti et al., 2012, 2014). For SN 2011fe, Margutti et al. (2012) limit the mass-loss rate for a 100 km s^{-1} wind to $\dot{M} < 2 \times 10^{-9}\ M_\odot\ \mathrm{yr}^{-1}$ (assuming inverse Compton emission, with $\epsilon_e = 0.1$) for the region within 5×10^{16} cm of the event.

Only recently – for the first time ever – have x-rays been observed for an SN Ia-CSM, SN 2012ca at about 600 days post-explosion using the *Chandra* observatory (Bochenek et al., 2018). The authors estimate that the x-ray luminosity at these times is similar to that of normal SNe IIn, somewhat surprising since other signs indicate that SNe Ia-CSM have much

higher density CSM (Silverman et al., 2013a). Being at late times, this is thermal emission; unfortunately the spectra are not of sufficient quality or span to say much about the gas properties.

1.4.3 Infrared: Dust

Interaction will create an infrared (IR) excess due to additional heating of surrounding dust above the level that the SN itself would heat it. Moreover, it is unclear whether dust can form in cooled, shocked gas. Studies of SNe Ia in the infrared to constrain dust properties typically focus on understanding the origin of dust in the universe, and find disappointingly low dust masses rather than surprising infrared excesses. But in line with SNe IIn, Fox and Filippenko (2013) find that interacting SNe Ia – both the prompt SN 2005gj and the Type Ia;n SN 2002ic – have significant mid-IR excess from the heating of pre-existing dust.

1.4.4 Optical: Bemusing Narrow Absorption Lines

In some SNe Ia, high-resolution optical spectra have revealed the presence of blueshifted, narrow absorption lines (NALs) that get deeper over time. The first report of this was Patat et al. (2007) with SN 2006X, and since then there have been more discovered (e.g., Simon et al., 2009; Patat et al., 2011). It is estimated the 20% of SNe Ia in late-type hosts (the hosts of 91T-likes) have time-variable NALs, but observing the variability is difficult due to the technical constraints but also because the lines eventually stop changing. Some authors have focused instead on the fact that in these cases the NALs have been blueshifted relative to the host lines. Based on single-epoch spectra, both Sternberg et al. (2014) and Maguire et al. (2016) find there is an excess of SNe Ia with blueshifted NALs; in fact, the frequency they find is consistent with the prior 20% rate.

The origin of the blueshifted/time-variable NALs is a matter of debate. One explanation is that these lines are formed in CSM, and the time variability is an effect of recombination in gas that was ionized by the SN (Patat et al., 2011). Calculations show that the CSM would need to be at a distance of $10^{16} - 10^{17}$ cm to explain the observed time evolution. However, other authors argue that the NALs are actually interstellar in origin, and the time variability is some kind of geometric effect; this is a more conservative position supported by the fact that NAL SNe Ia are all in dust-rich hosts. Very recently, Bulla et al. (2018) presented a nice geometric ISM explanation for the variable NALs.

Because the evidence is inconclusive, I do not take the presence of time-variable or blueshifted NALs as evidence for CSM; but I am deeply interested in determining whether it is CSM, and my models do apply to these cases.

1.4.5 Optical: Hydrogen Emission Lines

Obviously, searching for time-variable hydrogen emission lines in near-maximum-light spectra, akin to the optical signatures of SNe IIn, is one way to search for CSM. In introducing

SNe Ia-CSM (§1.1), I already mentioned that SNe Ia interacting with dense CSM are known, but they are rare.

Since uncertainty in the rate of SN Ia interaction comes from the fact that we do not know how often interaction is missed because it occurs after maximum light, I will review searches for hydrogen emission lines in spectra around 300 days after maximum light. The motivation for these observations was not to look for delayed interaction, but rather for mass that was stripped off the companion star by the SN ejecta. According to simulations, in SD scenarios $> 0.01\ M_\odot$ of material is caught up in the inner layers of the ejecta, with speeds of $< 1,000\ \mathrm{km\ s^{-1}}$ (Livne et al., 1992; Marietta et al., 2000). Initially hidden beneath the SN photosphere, this material becomes visible in the nebular spectra. For some SNe Ia there exist spectroscopic observations in the nebular phase that can rule out the presence of such material. Seven cases were reported individually (Mattila et al., 2005; Leonard, 2007; Shappee et al., 2013; Lundqvist et al., 2015) and Maguire et al. (2016) presented a sample of eleven objects. Although these authors constrain the stripped hydrogen mass in their work, the detailed modeling of Botyánszki et al. (2018) more strongly argues against any hydrogen or helium-rich companion (including an MS companion) for these SNe.

Unfortunately, however, none of the observed SNe were 91T-like. Fourteen of these SNe were normal or subluminous; one was between normal and 91T-like but strange (SN 2012fr); and in three cases I could not determine the sub-group from published data (SN 2012ht, SN 2013aa, and SN 2013ct).

1.4.6 Optical: Early-Time Excess from Impact with a Companion

Sometimes when I mention that I model "interacting SNe Ia," I am misunderstood to mean the interaction of the ejecta with the companion star itself. Technically I suppose this *is* circumstellar material, but I hope the reader is sympathetic to my exasperation at such a claim. Nevertheless I will describe these searches; because the signature of impact with a companion is similar to the signature of an impact with very compact, finite-extent CSM as might be left over from the merger of two WDs (Raskin and Kasen, 2013), and because I think we should continue these searches with an emphasis on 91T-like SNe Ia.

Kasen (2010) modeled the radiation signatures of SN Ia ejecta colliding with an MS or RG companion donating mass to the CO WD through RLOF. For a short while there is a "shadow" behind the companion through which high-energy photons from the shocked ejecta and stellar envelope can escape, creating a blue excess in the early-time light curve. But to see this, SNe Ia must be observed within days if not hours after explosion, which is rare. In addition, there is a viewing-angle effect: the signal is strongest for a line of sight down the cone, and invisible if the companion is on the opposite side from the observer. If such a signal were discovered, it would give information about the companion radius. Unfortunately, early-time excesses can be caused by other processes as well, such as interaction with CSM or the mixing of radioactive isotopes to the surface of the SN ejecta (Noebauer et al., 2017;

Piro and Morozova, 2016) that are not exclusive to the SD channel (Kromer et al., 2016).

Despite detections of short-duration early-time excesses (Cao et al., 2015; Marion et al., 2016; Hosseinzadeh et al., 2017; Miller et al., 2018), they are all either ambiguous in their association with companion interaction or that explanation is ruled out entirely (Liu and Stancliffe, 2016; Ferretti et al., 2017; Shappee et al., 2018; Sand et al., 2018). Yet the large sample of non-detections is itself interesting. For two SNe Ia with exquisite cadence in their early-time spectra, Olling et al. (2015) can exclude companions of $M_\star > 2M_\odot$ at the 68% confidence level for over 3/4 of the possible viewing angles. Bianco et al. (2011, Supernova Legacy Survey) and Hayden et al. (2010, Sloan Digital Sky Survey) ruled out RGs as the companions for the *majority* of SNe Ia. Unfortunately these data cannot comment on the SD channel for 91T-like SNe, as all events were normal or sub-luminous, or samples were not split into normal and 91T-like.

1.4.7 Comparison to SNe Ibc

Like SNe Ia, SNe Ibc show no evidence for hydrogen in their spectra; nor helium, in the case of SNe Ic. SNe Ibc do not show narrow hydrogen emission features to indicate the presence of CSM; yet they *are* detected in the radio and x-ray (Van Dyk et al., 2000; Dwarkadas and Gruszko, 2012). This exemplifies the point that interaction signatures may be evident at radio and x-ray wavelengths that are invisible in the optical. The detection of SNe at these energies was made possible by the completion of the VLA radio instrument in 1980 and the launch of the *ROSAT* x-ray imaging satellite in 1990. The first SN Ibc to be detected by a radio instrument was SN 1983N (Sramek et al., 1984), and the first with x-rays was SN 1994I (Immler et al., 1998).

Because of the success of the "mini-shell" model at explaining this radio emission as a wind (e.g., Chevalier, 1982b, 1998), the CSM of SNe Ibc is typically assumed to be a wind. In turn, the progenitors of these SNe were assumed to be Wolf-Rayet stars which have a high mass-loss rate, and the synchrotron parameter ϵ_B was set to $\epsilon_B = 0.1$ to match the winds of those objects: $\dot{M}_w \approx 10^{-4}\ M_\odot\ \mathrm{yr}^{-1}$, $v_w \approx 1,000\ \mathrm{km\ s}^{-1}$.

1.5 This Thesis: Modeling the Gaps

PTF11kx settled the debate (at least for *most* researchers) about whether events like SN 2002ic were really SNe Ia muffled by CSM – they were. In doing so, it settled the debate about whether any SNe Ia have hydrogen-rich companions – they must. But the CSM of PTF11kx was nothing like a wind, with its densest region nearest to the star. Instead, it had a low-density cavity before it hit a wall of CSM. The Chevalier (1982a) models and their extensions were asymptotic and could only describe times long after interaction had begun; but now we were seeing the very first stages of interaction. The "likely" models for how dense CSM shells would look placed them at 10^{18} cm and focused on detections decades after explosion; but we were seeing interaction within months, placing the shell at 10^{16} cm.

A nova shell leaves a 10^{16} cm cavity, but such shells are nowhere near the $\sim 1 M_{\odot}$ of material reported by Dilday et al. (2012). And the mystery of the SNe Ia-CSM remained: why are their environments so dense, pushing the limits of known star systems? Essentially, we were off track: our stellar evolution theory, our explosion theory, our interaction theory – none of it applied.

Looking at this situation, I determined that our understanding of interaction in SNe Ia was most limited by the lack of models: PTF11kx and the SNe Ia-CSM, which should have been a revolution in our field, were basically being ignored by the community because we couldn't *decipher* them! Which, as a theorist, and one who wanted to focus on radiation transport no less, I found unconscionable. So I decided to fix it. Stellar evolution couldn't tell me a likely CSM configuration, so I needed to explore a huge parameter space of properties, leading me to one-dimensional modeling. We were seeing detached shells of material, so I started with those. And I knew that I needed to produce everything – radio, x-ray, optical – because they all tell a part of the story and corroborate pieces of each other's narrative.

In the next chapter I will describe these simulations: their birth, their growth, and where they are heading. Chapters 2-6 describe how I have applied these models to elucidate the beguiling observations of PTF11kx, SN 2015cp, and the Type Ib;n SN 2014C. To give an idea for how different my modeling is, Figure 1.2 compares some of the densities I explore in this thesis to the profiles that had been exhaustively explored before I started my work. Finally, I dedicate Chapter 7 to discussing what has been illuminated by this work, how my findings can be applied to find and characterize more SNe Ia;n, and where I think we will be ten years from now in understanding SNe Ia.

Table 1.1: Glossary of Acronyms

Acronym	Expansion	Comment
AGB	asymptotic giant branch	star; possible companion of SNe Ia
AMI	*Arcminute Microkelvin Imager*	radio telescope at the Mullard Radio Astronomy Observatory (University of Cambridge, United Kingdom)
CO WD	carbon-oxygen WD	star that explodes as an SN Ia
CC SN	core-collapse SN	supernova associated with the collapse of a massive star core
CSE	circumstellar environment	
CSM	circumstellar medium, mass, or material)	
DD	double degenerate	progenitor scenario for SNe Ia
He WD	helium WD	star; possible companion of SNe Ia
IR	infrared	photon energy range
MS	main sequence	star
NUV	near-ultraviolet	photon energy range
RLOF	Roche-lobe overflow	binary star mass transfer mechanism
SD	single degenerate	progenitor scenario for SNe Ia
SN(e)	supernova(e)	
SN X	type X SN	
SN X;n	type X SN with delayed interaction	
SSA	synchrotron self-absorption	
RG	red giant	star; possible companion for SNe Ia
VLA	*Very Large Array*	telescope at the National Radio Astronomy Observatory (National Science Foundation; United States)
WD	white dwarf	star; possible progenitor (or companion) of SNe Ia
WR	Wolf-Rayet	star; possible progenitor of SNe Ibc

Note: For supernova class and sub-class descriptions see Ch 1.

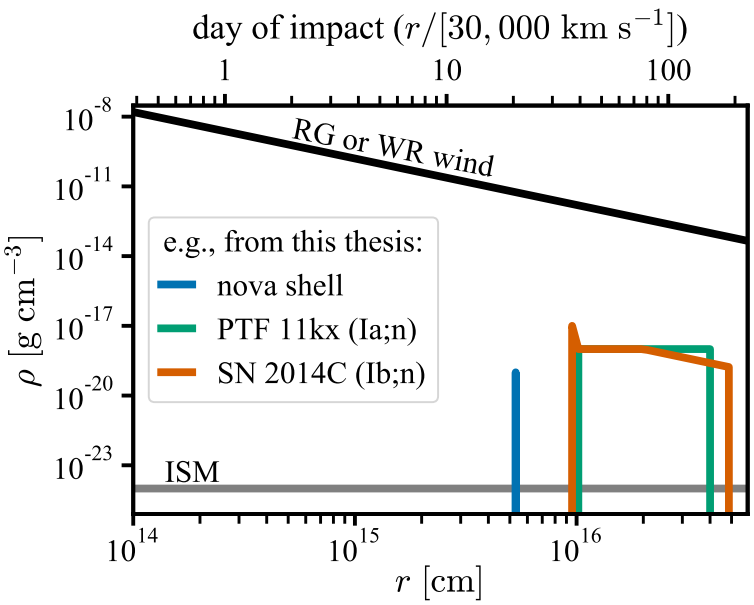

Figure 1.2: An example of the types of models I explore in this thesis for novae in general and two SNe X;n in particular, compared to the wind and ISM density profiles that were foundational to previous studies. The wind profile is for $\dot{M}/v_w = (10^{-6}\ M_\odot\ \mathrm{yr}^{-1})/(10\ \mathrm{km\ s}^{-1})$, appropriate for either a RG or WR star – WR stars have faster winds compensated by higher mass-loss rates. Note that the top axis is an approximation for the day of impact, showing when the outermost ejecta would reach a given radius.

Chapter 2

Ghost is the Shell: Hydrodynamic Simulations and Radiation Signatures of Ephemeral Interaction Scenarios

In this chapter I will describe the programs that I developed for this thesis and the simulations that I ran. The first section describes the physical problem being considered to give an understanding of the hydrodynamic and radiation regimes that the simulations exist in. The next two sections review the hydrodynamic solver used for my simulations and the setup of the simulations themselves, and then the radiation transport codes that I wrote and use in this work. The code developed by me – scripts for initializing a model as well as performing the radiation calculations – are available for viewing or download online[1]. Finally, I will discuss how I plan to move forward with the code development in the next year.

2.1 The Physical Problem: Transitional Stages of Interaction

The Chevalier self-similar solution is asymptotic, applying only long after interaction has begun. This is a good approximation for winds, which are at the progenitor surface and so can carry the initial supernova shock; but it is entirely wrong for SNe X;n. The other limitation of the self-similar solution is that it only describes the evolution of the shock fronts while they are inside the original power-law density profiles. This means that if the density profile steepens or flattens in the CSM, the solution no longer applies. For a scenario like a nova shell, the shock will quickly sweep over the shell; this means that not only does the shock not have time to reach the self-similar solution, but this solution cannot describe the evolution of the CSM once it has been swept over by the shock. For these reasons, ephemeral interaction scenarios require numerical modeling to describe the evolution of the shock fronts

[1] `https://github.com/chelseaharris/csmpy`

and the long-term evolution of the shocked gas. The other limitation of the second point is that if the reverse shock reaches the inner ejecta, the solution no longer applies. This will happen once the shock has traversed the CSM, if the CSM mass is greater than the outer ejecta mass. The outer ejecta mass is $\sim 10\%$ of the total ejecta mass; so if $M_{\rm csm} \gtrsim 0.1 M_{\rm ej}$, the self-similar solution will ultimately fail.

2.2 Initial Conditions

The simulations used in this thesis all have the same basic form for their initial conditions. The input to the code is a one-dimensional grid where the upper and lower radial boundaries of each grid cell are specified as well as the density, temperature, and velocity of the gas in that cell.

Because I am simulating a shock, which is driven by ram pressure of SN ejecta, the important quantities for the grid are the density profile of the freely expanding ejecta and the density profile of the nearly-static CSM. I group cells into "zones" in which the density and velocity have a given profile. Each zone represents either ejecta, CSM, or vacuum. It is not required that the density or velocity be continuous across zone boundaries.

The first (innermost) two zones describe the SN ejecta. These zones are freely expanding with speed related to position (r) and time (t) by

$$v_{\rm ej} = r/t \tag{2.1}$$

and have a density structure described by a broken power law as in Kasen (2010),

$$\rho_{\rm inner} = \zeta_\rho \frac{M_{\rm ej}}{(v_t t)^3} \left(\frac{r}{v_t t}\right)^{-\delta} \tag{2.2}$$

$$\rho_{\rm outer} = \zeta_\rho \frac{M_{\rm ej}}{(v_t t)^3} \left(\frac{r}{v_t t}\right)^{-n} , \tag{2.3}$$

where $M_{\rm ej}$ is the ejecta mass and v_t is the transition velocity between the inner and outer ejecta (typically around $10,000$ km s^{-1}). For all SNe in this thesis I use $\delta = 1$; but for SNe Ia, I use $n = 10$ and for SNe Ib, I use $n = 9$. The parameters ζ_ρ, v_t, and ζ_v are given by

$$\zeta_\rho = \frac{1}{4\pi} \frac{(n-3)(3-\delta)}{n-\delta} \tag{2.4}$$

$$v_t = \zeta_v \sqrt{\frac{E_K}{M_{\rm ej}}} = 6 \times 10^8 \zeta_v \sqrt{\left(\frac{E_{\rm K,tot}}{10^{51}\ {\rm erg}}\right)\left(\frac{M_{\rm Ch}}{M_{\rm ej}}\right)}\ {\rm cm\ s^{-1}} \tag{2.5}$$

$$\zeta_v = \sqrt{\frac{2(5-\delta)(n-5)}{(3-\delta)(n-3)}} . \tag{2.6}$$

Note that the values of ζ_ρ and ζ_v ensure that integration returns a total ejecta mass of $M_{\rm ej}$ and kinetic energy $E_{\rm K,tot}$.

Outside the ejecta zones are CSM zones. CSM zones have a constant velocity $v = v_{\rm csm} \leq 100$ km s^{-1} and in a given simulation, all CSM zones have the same velocity. Each CSM zone density profile is a power-law,

$$\rho_{\rm csm} = qr^{-s} \ . \tag{2.7}$$

For example, a steady wind has $s = 2$ and $q = \dot{M}/(4\pi v_w)$, with $\dot{M}$ the mass-loss rate and v_w the wind speed. A constant-density shell has $s = 0$. A simulation can then have a series of CSM zones with different power laws to create a complex CSM structure.

Finally, I may include a pseudo-vacuum or "interstellar medium" (ISM) zone beyond the last CSM zone. This zone has very low density (for ISM, 10^{-24} g cm^{-3}) and large extent. It is a buffer zone to ensure that there are no problems related to the grid boundary, and has low enough density that it does not affect the hydrodynamics of the simulation.

In my simulations, the initial temperature of the gas is unimportant and I set it to $10^3 - 10^4$ K.

One of the main advantages of dividing the simulations into zones is that my work is easier to reproduce and easier to track. With the "zone" organizational structure, I can distill the initial conditions into just a few parameters. I can recreate any grid if I know for each zone the temperature, total mass, velocity (and velocity power law or constant), density power-law index, and number of cells in that zone. I established PostgreSQL databases hosted by the National Energy Research and Scientific Computing (NERSC) center that store the model information for quick reproduction of my results.

2.3 The Hydrodynamics Solver

To model the shell interactions, I used the 1D spherically symmetric Lagrangian hydrodynamics code of Roth and Kasen (2015). The code solves the Euler equations using a standard staggered-grid Von Neumann-Richtmyer technique, and includes an artificial viscosity term to damp out post-shock oscillations (see, e.g., Castor, 2007). In an algorithm like this, grid cells (hereafter "cells") correspond to fixed-mass fluid elements, and radial boundaries of the cell change with each time step. This is attractive for my work because it naturally provides higher spatial resolution in the shock regions; with a spatially fixed grid, adaptive mesh refinement techniques are needed to get the same effect.

The code takes as input a User-defined grid and so it does not require that the mass resolution (mass per cell) be uniform throughout the grid. However, in early tests of the outer ejecta impacting one zone of CSM, I found that correct shock propagation requires these two zones to have the same mass resolution. Therefore I use a fixed mass resolution for all zones through which the shock will pass, except the vacuum zones (for which this is infeasible; this does not affect the hydrodynamics of the zones of interest). The exact number of cells used in my calculations varies, but is typically of order 10^4 total.

Although this code can treat radiative transport via Monte Carlo methods, I did not exercise the radiation capabilities in this thesis. Instead the calculations are purely hydro-

dynamical with an adiabatic index of an ideal gas, $\gamma_{\rm ad} = 5/3$, as radiative loses are small for the CSM densities considered.

The hydrodynamics code outputs files containing tables of gas properties at user-defined, linearly-spaced time intervals. I call these output files "snapshots," and they represent only a subset of the numerical time steps taken by the code.

2.3.1 Convergence

Simulations are approximations of nature, not only because we have the luxury of omitting physics that we think is unimportant, but also because we discretize continuous domains. As one may easily imagine, the more coarsely you represent the domain, the worse your solution will be. Therefore in numerical work it is important to ensure that one understands the accuracy of solutions by performing grid convergence studies.

With complex problems it is not always clear, however, what the benchmark quantity ought to be or even how to evaluate error. For the purposes of my work, I decided that the main hydrodynamic parameters whose accuracy affects my results are the gas density, temperature, and energy density. There are two regions that are concerning for my results. First is near the contact discontinuity, where the density in particular can change drastically (in multiple dimensions, there would usually be a Rayleigh-Taylor instability for the situations I consider). Second is near each shock front: the shock front ought to be a discontinuity but in the solver will be spread over a finite number of cells (and in fact this is true in nature as well, since relativistic particles will diffuse into the pre-shock gas). For example, if the shock front is spread over five cells, then I want to make sure I have at least five cells of CSM.

The results of my convergence study are shown in Figure 2.1. I show how the three gas properties of interest compare in low-resolution simulations to the high-resolution benchmark, for different times and different resolutions. I only show the results for the CSM cells, because the ejecta cells cannot be compared without extrapolation which introduces its own error; but the ejecta should be similar. I calculate the error for each cell, and what is shown is the median error, maximum error, and minimum error over all cells. I do not consider the maximum error to be representative for this case because they represent only the one or few cells nearest to the contact discontinuity; the median error is more reflective of how the resolution will affect derived quantities like light curves. For each resolution, I show how the error changes over time – each circle is a different time, progressing left to right. The leftmost point is not the initial conditions, but shortly after; the second point is when the shock is within the CSM; and the last points are as the CSM expands into the vacuum.

The median error quickly drops below 10% for even modest resolutions; but in my work I demand $N \geq 50$ for any zone that will be involved in interaction.

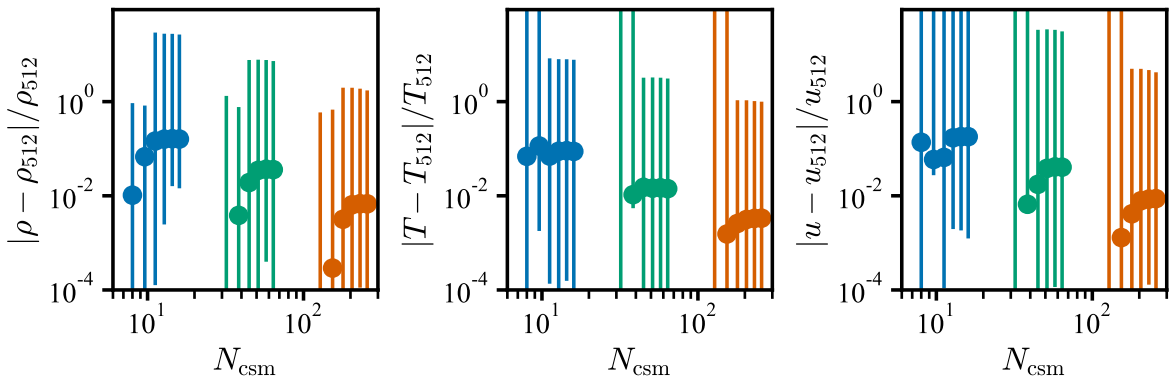

Figure 2.1: The convergence of the hydrodynamic solution with increasing mass resolution. The highest resolution simulation with 512 CSM cells ($N_{\rm csm} = 512$) is the benchmark to which we compare lower-resolution simulations of $N_{\rm csm} = 8$ (blue), $N_{\rm csm} = 32$ (green), and $N_{\rm csm} = 128$ (orange). Shown is the median error in the CSM cells (circle) with vertical lines showing the span (minimum to maximum) of the CSM cell errors. For each resolution we show how the error changes over time, separating the points in the x-direction for display purposes. In my simulations I ensure $N_{\rm csm} \geq 50$.

2.4 The Shock Front Finding Algorithm

The shock front finding algorithm is based on the idea that at the shock fronts there is a discontinuity in the gas speed, density, and pressure. I look for the discontinuities in the pressure because it is continuous across the contact discontinuity, whereas the density is not.

The shock front finding algorithm accepts any one-dimensional real-valued array $y = y_i$, and the User defines how many shock fronts to look for. The algorithm compares the array smoothed with a boxcar average of window size Δi to the array smoothed with a window size $\Delta i/2$. The large window will spread the discontinuity over a wider extent than the small window, so the two smoothed arrays will be the same except at the discontinuity. The algorithm identifies a shock front as the location of maximum difference between the two arrays. The second front is the location of the second-largest difference, and so forth.

Since in some simulations the energy density profile can be quite complicated and we are working with a one-dimensional code without mixing, the shock front algorithm occasionally misidentifies shock fronts. This is clearly seen in the evolution of the shock front over time: for one (or a few contiguous) snapshot the shock front will jump to a different location in the gas. When this misbehavior is identified, I linearly interpolate the index of the shock front according to its position in adjacent snapshots.

2.5 Radiation Calculations

After running the hydrodynamic simulations, I perform time-independent radiation calculations on the output snapshots. These calculations assume that the radiation field does not significantly affect the state of the gas; since the temperatures are very high and the shock produces ionizing radiation, it is a good approximation at these densities that the gas is fully ionized. They also do not account for the light-crossing time of the gas, but since the light crossing time is short relative to the hydrodynamic timescale this should be a small effect. Finally, my calculations do not explicitly account for the velocity field of the gas, because the gas has sub-relativistic speed and the processes are continuum processes.

The equations for the emission and absorption processes were given in the previous chapter; this section simply describes how they are applied to the models.

2.5.1 Particle Populations and the Equation of State

The relativistic particle population is as described in §1.3. The parameters $p, \epsilon_e, \epsilon_B$, and $f_{\rm nt}$ (Equations 1.7-1.10) are constant in time. This is certainly an oversimplification, but unfortunately reflects the current state of the art.

2.5.2 Optically Thin Emission

When absorption can be neglected, the specific luminosity is

$$\mathcal{L}_\nu = 4\pi j_\nu V \ , \tag{2.8}$$

where j_ν is the emission coefficient from all processes and V is the volume of the emitting gas. The hydrodynamic calculation gives the radial profile of the gas properties that go into the calculation of the emission coefficient and extinction coefficient for each process. So the luminosity is

$$\mathcal{L}_\nu = 4\pi \int (4\pi r^2) j_\nu(r) dr \rightarrow \mathcal{L}_\nu = (4\pi)^2 \sum_i \left[r_i^2 j_{\nu,i} (\Delta r)_i \right] \quad . \tag{2.9}$$

This calculation applies to the optically thin radio light curves of Chapter 3 and the free-free light curve of Chapter 4.

2.5.3 Ray-Tracing Algorithm to Include Absorption

When I began to model SN 2014C (Chapter 6), I finally had to confront absorption. There are various methods for accomplishing this and I chose ray tracing.

As illustrated in Figure 2.2, ray tracing is when one chooses representative paths to calculate the equation of radiation transport

$$\frac{dI_\nu}{ds} = -\alpha I_\nu + j_\nu \ , \tag{2.10}$$

where ds represents an infinitesimal segment of the path s and I_ν is the specific intensity of the beam. Rewritten in terms of the optical depth,

$$\tau = \int_0^S \alpha ds \ , \tag{2.11}$$

with $\tau = 0$ corresponding to the part of the path closest to the observer and $\tau = \tau_{\max}$ being the farthest, the radiation transport equation is

$$\frac{dI_\nu}{d\tau} = -I_\nu + S_\nu \ , \tag{2.12}$$

where S_ν is the source function

$$S_\nu = \frac{j_\nu}{\alpha} \quad . \tag{2.13}$$

Thus, assuming that at $I_\nu(\tau_{\max}) = 0$, the specific intensity is

$$I_\nu = \int_0^\tau S_\nu e^{\tau' - \tau} d\tau' \ . \tag{2.14}$$

The specific flux F_ν is the first moment of the specific intensity:

$$F_\nu = \int I_\nu \cos\theta d\Omega = 2\pi \int_0^1 I_\nu \cos\theta d(\cos\theta) \ , \tag{2.15}$$

where $d\Omega$ is the solid angle and θ is the angle between the line of sight and THE surface normal. For spherically symmetric cases,

$$\mathcal{L}_\nu = F_\nu \left(4\pi R^2\right) \ , \tag{2.16}$$

where R is the radius at which $\tau = 0$.

My method for translating this to a numerical calculation with a discrete grid is shown in Figure 2.2. When I evaluate these integrals numerically, of course, the simulation snapshot has defined radial boundaries for each cell and within a cell the gas properties (density, pressure) are constant. I determine the number of angles I want to sample in a grid that has uniform spacing in $\cos\theta$. Each θ defines a path through the sphere; this path either ends at the "absorbing core" (if $\theta < \theta_t$) or at the outer edge. The special angle θ_t is defined by

$$\sin\theta_t = r_{\mathrm{in},0}/r_{\mathrm{out},N} \ , \tag{2.17}$$

where the index 0 represents the innermost cell in the radiation calculation and N the outermost. I calculate $j_{\nu,i}(\vec{\nu})$ and $\alpha_i(\vec{\nu})$ for each cell (where I am using $\vec{\nu}$ to represent the array of frequencies at which the radiation field is being calculated), summing the contribution of all processes. Then the source function is $S_{\nu,i} = j_{\nu,i}/\alpha_i$ and the contribution to the optical depth of the path segment through each cell is

$$(\Delta\tau)_i = \alpha_i(\Delta s)_i \ . \tag{2.18}$$

These then are used in the discrete form of Equations 2.14-2.16 to calculate the luminosity of the snapshot.

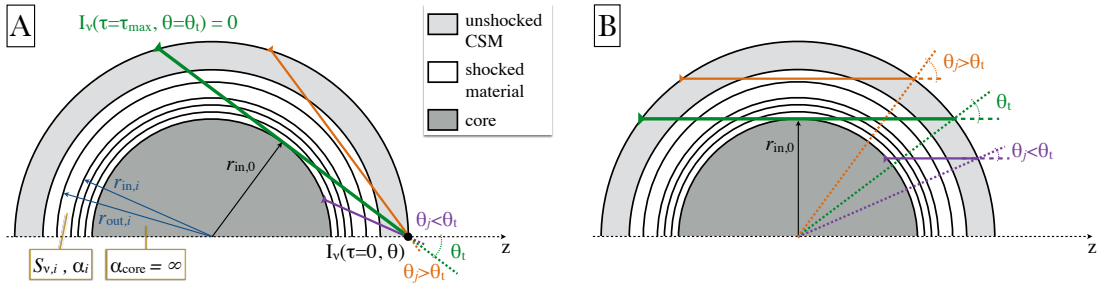

Figure 2.2: An illustration of the ray-tracing algorithm, with three different radiation paths (or "rays") shown (purple, green, orange). The z-axis represents the observer line of sight. Since the calculation is one-dimensional, there are two equivalent ways of conceptualizing the algorithm, shown in panels A and B. Panel A: For any point on the surface of the simulation, consider how different paths (specified as different angles θ) are contributing to the intensity at that point. Panel B: Consider the contribution to the observed radiation from different annuli of the projected circle seen by the observer; paths are still defined by θ which represents the angle between the line of sight and the spherical surface. Each cell of the hydrodynamic simulation (index i) has a source function $S_{\nu,i}(r_i)$ and extinction coefficient $\alpha_i(r_i)$ that defines those quantities for $r_{\mathrm{in},i} \leq r < r_{\mathrm{out},i}$. Because the hydrodynamics are on a Lagrangian grid, the cells are of non-uniform radial extent. As a simplification, the calculations in this thesis assume that the unshocked ejecta will completely absorb radio and x-ray emission. Paths that intersect the core ($\theta < \theta_t$) have a contribution from all cells. The special angle θ_t defines the maximum path length. Most paths with $\theta > \theta_t$ do not contain light from the innermost cells of the calculation. For cells representing shocked material, both free-free and synchrotron processes contribute to the radiation; for unshocked CSM, only free-free contributes.

2.6 Future Improvements and Extensions

I would like to address the optical (especially the atomic line) signatures of interaction simultaneously and self-consistently with the radio and x-ray light. I believe the best way to do this would be to incorporate the shock-specific aspects of the calculations into the radiation transport code `sedona` and its hydrodynamic solver. This means adding my shock front finder into the code, probably by introducing a scalar field representing the relativistic electron population. The synchrotron emission will then be straightforward to add, but needs to be added in a way that allows for further sophistication in the treatment of the magnetic field strength. I would also like to incorporate a one-dimensional approximation for the Rayleigh-Taylor instability (Duffell, 2016) in the hydrodynamic calculation.

Table 2.1: Glossary of Variables

Symbol	Meaning	Defining Equation
μ	mean molecular weight	$\rho = \mu m_p n$
σ_T	Thomson scattering cross section	
A	atomic mass number	
c	speed of light (in vacuum)	
k_B	Boltzmann constant	
m_e	electron mass	
m_p	proton mass	
q_e	electron charge	
Z	atomic number	
α	extinction coefficient [cm^{-1}]	
β	speed normalized to speed of light in vacuum	
ϵ_e	ratio of u_e to the gas internal energy density	Equation 1.10
ϵ_B	ratio of u_B to the gas internal energy density	Equation 1.18
γ	Lorenz factor	$(1-(v/c)^2)^{-1/2}$
γ_{ad}	adiabatic index	Equation 1.4
ν_B	synchrotron gyration frequency	
ρ	mass density	
ρ_{inner}, ρ_{in}	inner ejecta density	Equation 2.2
ρ_{outer}, ρ_{out}	outer ejecta density	Equation 2.3
ρ_{csm}	CSM density	Equation 2.7
τ	optical depth	Equation 2.11
A_R	CSM-to-ejecta density ratio at contact discontinuity	Equation 3.4
B	magnetic field amplitude	
c_s	sound speed	
$E_{\mathrm{K,tot}}$	ejecta kinetic energy	
f_R	fractional width of a CSM zone	Equation 3.3
I_ν	specific intensity [erg cm^{-2} Hz^{-1} ster^{-1}]	
j_ν	emission coefficient [erg cm^{-3} Hz^{-1} ster^{-1}]	
n	particle density [cm^{-3}]	
n_e	electron density [cm^{-3}]	
$n_{e,\mathrm{nt}}$	non-thermal electron density [cm^{-3}]	Equation 1.7
n_I	ion density [cm^{-3}]	
$\mathcal{L}$	luminosity [erg s^{-1}]	
$\mathcal{L}_\nu$	specific luminosity [erg s^{-1} Hz^{-1}]	
$\mathcal{L}_{\nu,\mathrm{p,ss}}$	radio peak luminosity for fiducial model family	Equation 3.28

Table 2.1: continued

Symbol	Meaning	Defining Equation
$\mathcal{M}$	Mach number	ratio of flow speed to sound speed in gas
$M_{\rm ej}$	ejecta mass	
p	gas pressure (per unit volume) *or* non-thermal power-law index	as index: Equation 1.7
r	radius or distance [cm]	
$R_{c,0}$, $R_{\rm in}$	initial contact discontinuity radius, CSM inner radius [cm]	
$R_{c,0,\rm ss}$	$R_{c,0}$ for fiducial model family	Equation 3.4
S_ν	source function [erg cm^{-2} Hz^{-1} ster^{-1}]	Equation 2.13
$t_{\rm imp}$	impact time of SN with CSM	
$t_{\rm cool}$	radiative cooling time	Equation 3.12
$t_{\rm dyn}$	dynamical time	Equation 3.6
$t_{\rm diff}$	radiative diffusion time	Equation 3.9
u	thermal energy density	
u_B	magnetic field energy density	
u_e	relativistic electron energy density	
v	speed	
v_t	transition velocity between inner and outer ejecta	Equation 2.5

Chapter 3

The Bradio Bunch: A Family of Synchrotron Light Curve Models for Nova Shell Interaction

Here, I introduce the "fiducial model set" of nova shell interactions. This is interaction of an SN Ia with a thin, constant-density CSM shell at $> 10^{15}$ cm and density $10^{-21}-10^{-18}$ g cm^{-3}. The "fiducial" family is defined by the ejecta and CSM being in a particular density ratio at the start of interaction. Prior to this work, it was impossible to quantitatively assess such a scenario in an ensemble of radio non-detections to rule out nova shells. I find that the optically thin radio synchrotron light curves of these simulations rise and fall with a predictable timescale and normalization, such that the light curves are governed by just three parameters: the CSM shell width, density, and inner radius. Using this parameterization, it is simple to analyze radio non-detections to determine the observability of different nova shell configurations to limit the CSM properties. In this chapter I perform such analysis on the non-interacting normal SN 2011fe and SN 2014J. In Chapter 5, I apply the same analysis to SN 2015cp. At the end of the chapter, I extend the modeling to interactions of multiple shells and find that there is interesting behavior worth future investigation. This chapter is largely a reproduction of Harris et al. (2016).

3.1 The Fiducial Model Family

Previous work on CSM interaction has used the self-similar formalism of Chevalier (1982a, hereafter, C82a). In that model, freely expanding ejecta described by a power-law density profile $\rho_{\rm ej} = g^n t^{n-3} r^{-n}$ runs into stationary CSM with density $\rho_{\rm csm} = q r^{-s}$. The notations of these expressions are as in C82: g and q are scaling parameters, t is the time since explosion, r the distance from the supernova center, and n and s are the power-law indices describing the interacting media. The self-similar evolution allows various quantities, including shock position and velocity, to be simply calculated at any time. This formalism has been applied

to various core-collapse supernova data with favorable results, and for this reason, as well as its ease of use, the C82 framework is prevalent in studies of interacting SNe. The well-deserved popularity of this model has motivated its use as a foundation for the "fiducial model set" of this study.

As described in §2.2, we adopt a broken power law description for the ejecta density profile with

$$\rho_{\rm outer}(r) = \frac{0.124 M_{\rm ej}}{(v_t t)^3} \left(\frac{r}{v_t t}\right)^{-10}, \tag{3.1}$$

$$v_t = (1.014 \times 10^4 \text{ km s}^{-1}) \ (E_{51}/M_{\rm c}), \tag{3.2}$$

where $M_{\rm c} = M_{\rm ej}/M_{\rm Ch}$ is ejecta mass in units of the Chandrasekhar mass and $E_{51} = E/(10^{51} \text{ erg})$ is the explosion energy (in this work, we take $M_{\rm ej} = 1.38\ M_\odot$ and $E_{51} = 1$). We assume that the power-law profile of the ejecta extends to a maximum velocity, $v_{\rm ej,max}$. The ejecta are initially freely expanding with uniform temperature $T_{\rm ej} = 10^4$ K; the value of the preshock ejecta temperature does not play a significant role in the evolution of the shocked gas.

The CSM is taken to be confined to a shell with an inner radius, $R_{c,0}$, and width $\Delta R_{\rm csm}$. We define the fractional width, f_R, as

$$\Delta R_{\rm csm} \equiv f_R R_{c,0} \ . \tag{3.3}$$

In this work a "thin" shell is a shell with $f_R = 0.1$ and a "thick" shell has $f_R = 1$. For example, Moore and Bildsten (2012) predict $f_R \approx 0.1$ for the shells swept up by nova outbursts. In our calculations, we assume that there is no CSM interior to $R_{c,0}$.

The CSM at the start of our simulation (the time of impact) is constant density ($s = 0$), constant velocity ($v_{\rm csm} = 1$ km s^{-1}), and isothermal ($T_{\rm csm} = 10^3$ K). The chosen value of $v_{\rm csm}$ is arbitrary and unimportant as long as it is much less than the ejecta velocities. Observations of variable narrow absorption features in SN Ia spectra demonstrate the possibility of moderate velocities, such as $v_{\rm CSM} \approx 65$ km s^{-1} in PTF 11kx (Dilday et al., 2012).

The ejecta impact the shell at time $t_{\rm imp}$ after explosion. In our set of fiducial models, we set initial conditions such that the ratio of $\rho_{\rm csm}$ to $\rho_{\rm ej}$ at the contact discontinuity is a fixed value. Physically, our motivation is that the interaction typically becomes most prominent once $\rho_{\rm ej} \approx \rho_{\rm csm}$. The value we use is $\rho_{\rm csm}/\rho_{\rm ej} = 0.33$ so that the initial contact discontinuity radius $R_{c,0}$ corresponds to the C82 contact discontinuity radius at the time of impact (Equation 3 of C82)

$$R_{c,0,\rm ss} = \left[A_R \left(\frac{g^n t^{n-3}}{q}\right)\right]^{1/(n-s)} = \left(0.041 M_{\rm ej} v_t^7\right)^{0.1} \ t_{\rm imp}^{0.7} \ \rho_{\rm csm}^{-0.1} \tag{3.4}$$

$$= (5.850 \times 10^{14} \text{ cm}) \left(\frac{t_{\rm imp}}{\rm day}\right)^{0.7} \rho_{\rm csm,-18}^{-0.1}, \tag{3.5}$$

where $A_R = 0.33 = \rho_{\rm csm}/\rho_{\rm ej}$ (for $n = 10, s = 0$) and $\rho_{\rm CSM,-18} = \rho_{\rm csm}/(10^{-18}$ g cm$^{-3})$. Because of this connection to the C82 self-similar solution, we use the subscript "ss" in this work to note when this constraint on the initial conditions is in place. Although our calculations do not assume a self-similar structure, restricting our initial setup in this way turns out to produce a family of light curve models that are amenable to simple parameterization. We explore calculations with different initial conditions in §3.4.

Equation 3.4 shows that, within the fiducial model set, choosing $R_{c,0}$ and $\rho_{\rm csm}$ fixes the impact time $t_{\rm imp}$, and hence the maximum ejecta velocity $v_{\rm ej,max} = R_{c,0}/t_{\rm imp}$. Figure 3.1 illustrates the values of $R_{c,0,\rm ss}$ and $\rho_{\rm csm}$ shown in this work, and shows that the fiducial model set obeys the assumptions of transparency and lack of radiative cooling (quantified below).

Figure 3.2 shows the evolution of the energy and mass density profiles for a supernova impacting a typical $f_R = 0.1$ shell model. Immediately before impact (panel A), the CSM has low energy density, a flat density profile, and is moving slowly. The interaction creates a forward shock moving into the CSM, and a reverse shock propagating backward into the ejecta. The forward shock eventually reaches the outer edge of the shell at a time we call "shock breakout." At this time (panel B), the dynamics have not yet reached a self-similar state; the internal energy density of the gas, $u_{\rm gas}$, is high and the CSM has been accelerated to nearly the ejecta speed. Shock breakout accelerates the CSM such that shortly afterward (panel C), the mass and energy densities have dropped drastically and the outermost CSM has reached speeds over $30,000$ km s^{-1}. At a time 1.41 times the impact time (panel D), the velocity profile has approximately returned to the $v \propto r$ of free expansion. The mass and energy density profiles will thereafter decrease according to adiabatic free expansion.

The impact radius constraint $R_{c,0} = R_{c,0,\rm ss}$ (Equation 3.4) defines a fiducial set of single-shell interaction models. As we will see in §3.3, these models generate a family of light curves from which it is possible to deduce CSM properties.

3.1.1 Diffusion and Cooling Timescale Estimates

We simulate the interaction between ejecta and CSM under the assumptions that (1) the gas is optically thin to electron scattering, so photons can free-stream through it and (2) the gas does not radiatively cool. To investigate the legitimacy of these assumptions, we can compare the timescale for dynamical changes ($t_{\rm dyn}$) to the diffusion time ($t_{\rm diff}$) and the cooling time ($t_{\rm cool}$) in the forward shock region.

The dynamical time is

$$t_{\rm dyn} = R/v \approx R_{c,0}/v_{\rm ej} \approx t_{\rm imp} \ , \tag{3.6}$$

since the shocked gas is quickly accelerated to nearly the ejecta velocity and the ejecta is freely expanding.

The assumption that photons can free-stream requires that the diffusion time be much less than the dynamical time. The diffusion time for electron scattering through a shocked

region of width ΔR_s and optical depth τ is

$$t_{\rm diff} = \frac{\Delta R_s}{c} \min(\tau, 1) \ . \tag{3.7}$$

Assuming that all species are fully ionized within the shocked region, the electron number density (n_e) and ion number density (n_I) are related to the mass density (ρ), atomic number (Z), atomic mass (A), and proton mass (m_p) through $n_e = Z n_I$ and $n_I = \rho/(A m_p)$, so the optical depth to electron scattering is

$$\tau = \sigma_T n_e \Delta R \approx (4 \times 10^{-3}) \left(\frac{Z}{A}\right) \rho_{s,-18} \Delta R_{s,16} \ , \tag{3.8}$$

with $\rho_{s,-18}$ the density of the gas in the shocked region per 10^{-18} g cm^{-3} and $\Delta R_{s,16}$ the width of the shocked region per 10^{16} cm. For the estimates here, we assume the gas is hydrogen dominated so $Z \approx A \approx 1$. Assuming a typical value for the shock width $\Delta R_s \approx 0.1 R_c$ and that the postshock density is related to the initial CSM density as $\rho_s \approx 4\rho_{\rm CSM}$,

$$t_{\rm diff} \approx (1 \text{ min}) \ R_{c,16}^2 \ \rho_{\rm CSM,-18} \ . \tag{3.9}$$

The assumption that the shocked gas does not cool requires that the cooling time be much longer than the dynamical time. The cooling time for any radiative process is given by

$$t_{\rm cool} = u_{\rm gas}/(4\pi j) = 1.5 \ n k_B T/(4\pi j) \ , \tag{3.10}$$

where $u_{\rm gas}$ is the gas internal energy density (which we have assumed is that of a monatomic ideal gas) and j is the angle-averaged, frequency-integrated emissivity of a radiative process. For free-free emission of thermal electrons, the angle-integrated emissivity (corresponding to $4\pi j$ in the above equation) is

$$j_{\rm ff} = 1.43 \times 10^{-27} \ Z^2 n_I \ n_e \ T^{1/2} \ \bar{g}_B \tag{3.11}$$

in cgs units (Rybicki and Lightman, 1979). Choosing a value of 1.2 for the gaunt factor $\bar{g}_B$ gives an accuracy of about 20%. Using n_e, n_I as above and again assuming the shocked material has a density $\rho \approx 4\rho_{\rm csm}$ and $A = Z = 1$,

$$t_{\rm cool,ff} \approx (1600 \text{ yr}) \ \rho_{\rm CSM,-18}^{-1} \ T_9^{1/2} \ , \tag{3.12}$$

where $T_9 = T/(10^9 \text{ K})$. The strong shock jump conditions for an ideal gas link the temperature and shock velocity as

$$\frac{3}{2}\frac{\rho_{\rm csm}}{\mu m_p} k T_s \ = \ u_{\rm gas} = \frac{P}{\gamma_{\rm ad} - 1} = \frac{3}{2}\left(\frac{2}{\gamma_{\rm ad}+1} \ \rho_{\rm csm} v_s^2\right) = 1.125 \rho_{\rm csm} v_s^2 \tag{3.13}$$

$$\Rightarrow \ T_9 \ \approx \ 9 \mu v_{s,9}^2 \ , \tag{3.14}$$

where here $\gamma_{\rm ad}$=5/3 is the adiabatic index and $v_{s,9} = v_s/(10^9$ cm s$^{-1})$ is the shock velocity per 10,000 km s^{-1}. For our models we expect that v_s is similar to the ejecta velocity, so $T_9 \approx 1 - 10$ and thus the cooling timescale is much longer than the dynamical timescale.

For the fiducial model set, we can use Equations 3.4 and 3.14 to recast the diffusion and cooling timescales in terms of physical parameters. Figure 3.1 illustrates these constraints and shows that our models obey them.

3.2 Synchrotron Radiation Calculation

The equations for synchrotron radiation are given in §1.3 and the method for calculating synchrotron emission in the optically thin case is described in §2.5.

Assuming fully ionized hydrogen ($n_e = (Z/A)\rho/m_p$ with $Z/A = 1$ as described for Equation 3.8), the synchrotron emission coefficient (Equation 1.20) is

$$j_\nu(\nu > \nu_c \mid p = 3) = (1.3 \times 10^{-15} \text{ erg s}^{-1} \text{ cm}^{-3} \text{ Hz}^{-1} \text{ sr}^{-1}) \left(\frac{\epsilon_e}{0.1}\right)^2 \left(\frac{\epsilon_B}{0.1}\right) \times \left(\frac{\rho}{10^{-18} \text{ g cm}^{-3}}\right)^{-1} \left(\frac{u_{\rm gas}}{10^2 \text{ erg cm}^{-3}}\right)^3 \left(\frac{\nu}{\text{GHz}}\right)^{-1} . \quad (3.15)$$

For a quantitative discussion of our optically thin assumption as it applies to synchrotron self-absorption, see §3.2.

As discussed in the main text, for a few models we consider the emission from the reverse shock region. This is calculated in the same manner except that the composition is assumed to be dominated by species heavier than hydrogen, in which case $A/Z = 2$.

Synchrotron Self-Absorption

The relativistic electrons that create synchrotron emission also absorb synchrotron radiation (synchrotron self-absorption, SSA). With some substitution we can write Equation 1.21 as

$$\alpha_{\rm SSA} = \frac{1}{64}\left(\frac{6}{\pi}\right)^{(p+3)/2} \Gamma\left(\frac{3p+2}{12}\right) \Gamma\left(\frac{3p+22}{12}\right) \frac{\sigma_T c}{m_e} u_B C \nu_B^{(p-2)/2} \nu^{-(p+4)/2} \quad (3.16)$$

$$= (4.74 \times 10^{-7} \text{ cm}^{-1}) \left(\frac{\epsilon_e}{0.1}\right)^2 \left(\frac{\epsilon_B}{0.1}\right)^{5/4} \times \left(\frac{\rho}{10^{-18} \text{ g cm}^{-3}}\right)^{-1} \left(\frac{u_{\rm gas}}{10^2 \text{ erg cm}^{-3}}\right)^{13/4} \left(\frac{\nu}{\text{GHz}}\right)^{-7/2} , \quad (3.17)$$

where ρ is the mass density of the shocked gas and $u_{\rm gas}$ its internal energy density.

We can estimate the optical depth of a model by assuming $\alpha_{\rm SSA}$ is uniform in the shocked gas. With $\mu \approx 1$ and $\rho = 4\rho_{\rm csm}$ the energy density is

$$u_{\rm gas} \approx \frac{6\rho_{\rm csm}}{m_p} k_B T \approx 0.5 \ \rho_{\rm CSM,-18} T_9 , \quad (3.18)$$

so

$$\alpha_{\rm SSA} \approx (1.6 \times 10^{-14}\ {\rm cm}^{-1})\ \rho^{2.25}_{\rm CSM,-18} T_9^{3.25} \nu_9^{-3.5}\ , \tag{3.19}$$

where $\nu_9 = \nu/{\rm GHz}$. Assuming the shocked region has a width $\Delta R_s \sim 0.1 R_c$, then

$$\begin{aligned} \tau_{\rm SSA} &\sim 0.1 \alpha_{\rm SSA} R_c & (3.20)\\ &\sim 16\ R_{c,16}\ \rho^{2.25}_{\rm csm,-18}\ T_9^{3.25}\ \nu_9^{-3.5}\ . & (3.21) \end{aligned}$$

The optical depth of a model varies with time because of these dependencies on temperature and radius, but we show the line of $\tau = 1$ in Figure 3.1 assuming $T_9 = 20$ and $\nu_9 = 4.9$ for reference.

When fiducial models are optically thin such that the synchrotron luminosity is set by the emissivity, their light curves obey scaling relations that reflect the similar hydrodynamic evolution of the models as described in §3.3. As the models become more optically thick, the light curve is set by the source function $S_{\nu,\rm SSA}$, which from Equations 3.15 and 3.17 we calculate to be

$$\begin{aligned} S_{\nu,\rm SSA} = \frac{j_\nu}{\alpha_{\rm SSA}} &= (2.8 \times 10^{-9}\ {\rm erg\ s^{-1}\ cm^{-2}\ Hz^{-1}\ sr^{-1}}) \\ &\times \left(\frac{u_B}{10\ {\rm erg\ cm^{-3}}}\right)^{-1/4} \left(\frac{\nu}{\rm GHz}\right)^{-5/2}\ . \end{aligned} \tag{3.22}$$

For arbitrary optical depth, the luminosity of a one-dimensional numerical model can be found via the formal solution of the radiative transfer equation using this source function.

3.3 Radio Synchrotron Light Curves for Fiducial Model Set

Radio emission is a tell-tale sign of interaction and commonly used to study astronomical shocks. Here we present radio synchrotron light curves of the models described in the previous section. These models are restricted to low densities where synchrotron self-absorption is not important (Figure 3.1). Calculating light curves requires that we parameterize the fraction of postshock energy in magnetic fields, ϵ_B, and in non-thermal relativistic electrons, ϵ_e. We assume constant values typically used in the literature, $\epsilon_B = 0.1, \epsilon_e = 0.1$, but note that these quantities are a main source of uncertainty in predicting the radio emission. Calculating x-ray and optical line signatures of our models is an exciting possibility for future work, but here we wish to focus on illustrating the radio emission produced by shell interaction and how it differs from the commonly applied self-similar model.

We assume that the CSM is of solar composition and that the conditions in the shocked ejecta are such that only the fully-ionized shocked CSM (temperature exceeding 10^4 K) contributes to the synchrotron emission (Chevalier and Fransson, 2006; Warren et al., 2005).

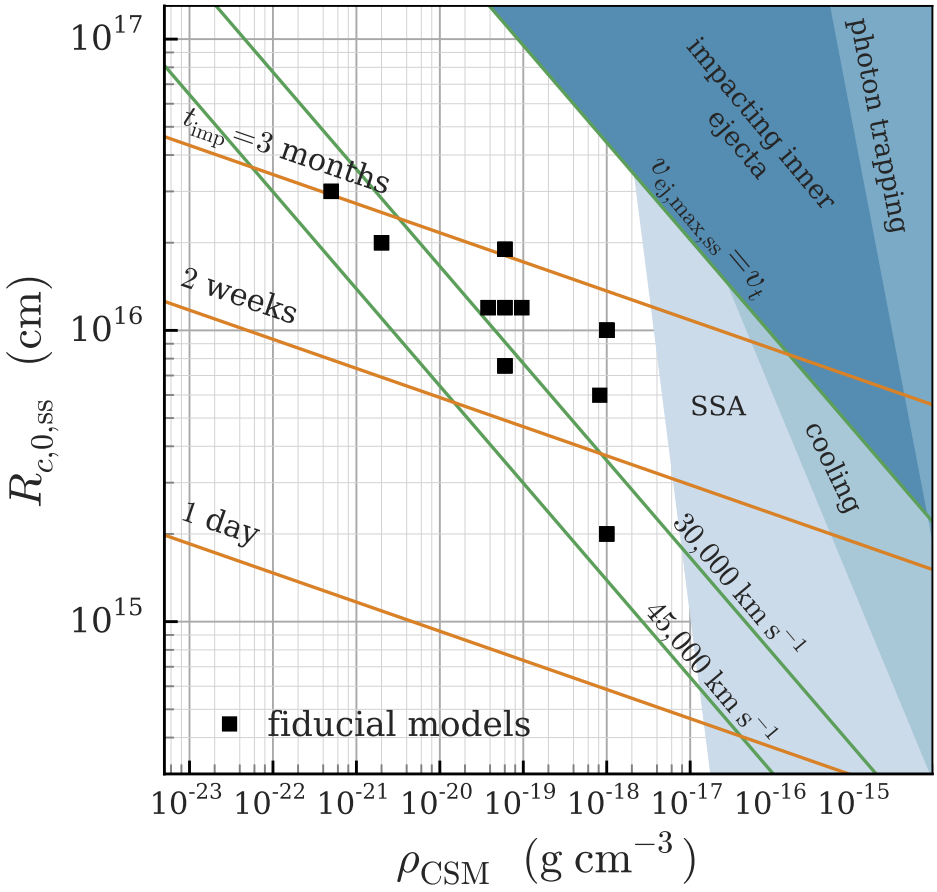

Figure 3.1: A visual representation of the fiducial models presented in this work (black squares) and assumptions (Appendices 3.1.1 and 3.2), depicted in the $\rho_{\rm csm} - R_{c,0,\rm ss}$ plane, where $\rho_{\rm csm}$ is the CSM density and $R_{c,0,\rm ss}$ is the initial contact discontinuity radius for a fiducial model (Equation 3.4). Note that models of different shell fractional width (Equation 3.3) occupy the same position in this space. Lines of constant impact time, $t_{\rm imp}$ (orange), and maximum ejecta velocity, $v_{\rm ej,max,ss}$ (Equation 3.43; green), are derived from Equation 3.4. Shaded regions show where our assumptions would be violated: when the shock region is optically thick to electron scattering and traps photons ($t_{\rm diff} \geq 0.01 t_{\rm dyn}$), the shocked gas cools ($t_{\rm cool} \geq 100 t_{\rm dyn}$), the CSM impacts dense inner ejecta instead of outer ejecta layers ($v_{\rm ej,max,ss} > v_t$, Equation 2.5), or the light curve is altered by synchrotron self-absorption (SSA; $\tau_{\rm SSA} > 1$ for $T = 10^9$ K and $\nu = 4.9$ GHz, Equation 3.21).

Representative light curves are shown in Figure 3.3 for interactions with shells of various widths, impact radii, and CSM densities. The light curves initially rise as the shock moves through the shell and increases the volume of shocked material (the emission region). The

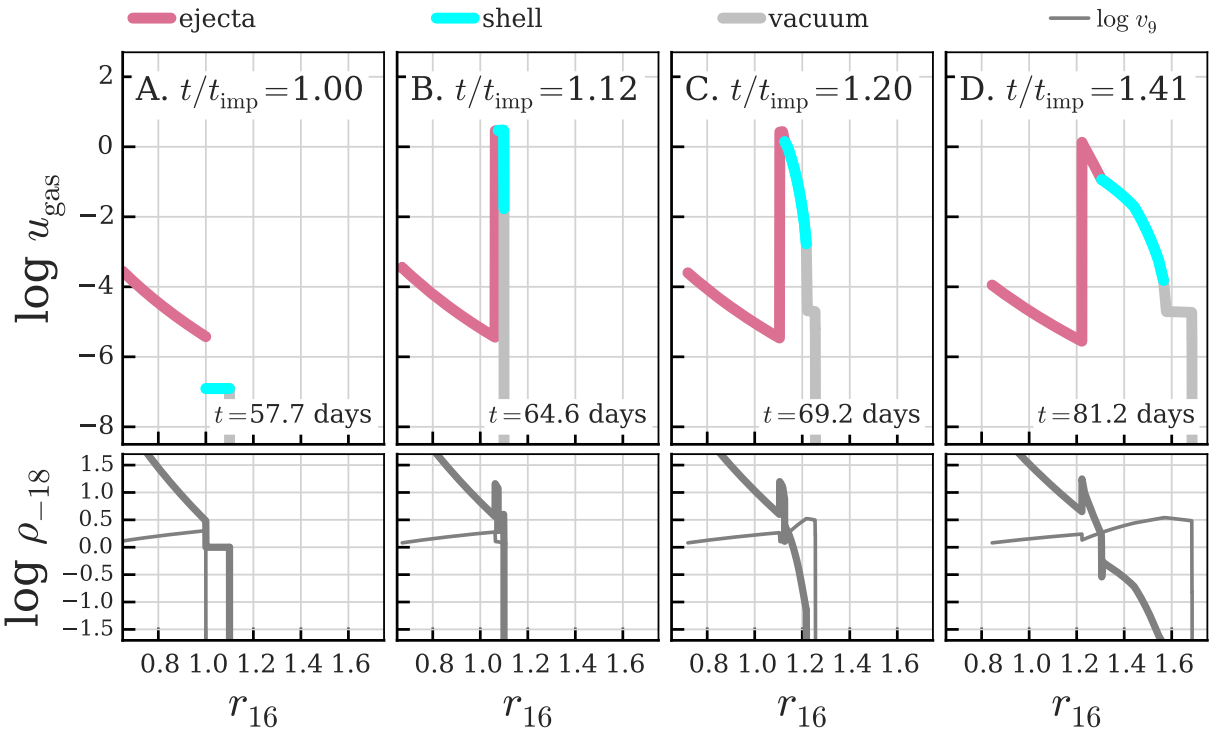

Figure 3.2: The evolution of internal energy density in erg cm^{-3} (log scale, log $u_{\rm gas}$; top), mass density per 10^{-18} g cm^{-3} (log scale, log ρ_{-18}; bottom; thick), and velocity per 10^9 cm s^{-1} (log scale, log v_9; bottom; thin) as a function of radius per 10^{16} cm (linear scale, r_{16}) in a fiducial thin shell impact model ($f_R = 0.1, v_{\rm ej,max} = 20,047$ km s$^{-1}, \rho_{\rm csm} = 10^{-18}$ g cm$^{-3}, R_{c,0} = 10^{16}$ cm). In the top panels, different regions of the model are color-coded: ejecta (pink), CSM (cyan; radiating region), and vacuum (grey). These regions do not mix in our simulations. The times shown are the initial state (A); the moment of shock breakout (B); after shock breakout, before all of the CSM has been accelerated (C); and after significant expansion (D). Labels refer to both the time relative to impact ($t_{\rm imp}$) and time since explosion (t). We see that energy density, which dominates the shell emissivity (Equation 3.15), is high while the shock front is in the shell and drops dramatically after shock breakout.

light curves reach a sharp peak, then rapidly decline. The peak occurs at shock breakout, which we define as the moment the radius of the forward shock front reaches the outer radius of the CSM. The rapid decline can be attributed to the plummeting internal energy of the gas as the shell suddenly accelerates (Figure 3.2, Equation 1.20). Changing only the shell width changes the time of shock breakout and therefore wider shells – in which breakout necessarily occurs later – produce broader, brighter light curves. Thinner shells follow the rise of the thicker shells until the time of shock breakout, as expected since the shock evolution should be the same while inside the shell.

In the left panel of Figure 3.3 we show how including the contribution of the reverse shocked ejecta affects the radio light curves. We use the same radiation parameters for the ejecta as for the CSM (except we assume metal-rich gas so $Z/A \approx 0.5$ in the calculation of electron density). We find that under these assumptions the reverse shock contributes negligibly (about 10%) to the light curve before shock breakout but becomes dominant at later times, when it has a much higher energy density than the CSM (see panel D of Figure 3.2). However, we stress that it is unclear whether the conditions in the postshock ejecta are the same as in the postshock CSM; emission from the postshock ejecta could be dimmer than we have calculated here if, for instance, this region has a lower value of ϵ_B. Because of the uncertainty in how to treat the ejecta relative to the CSM, in this work we do not include the ejecta when calculating the radio emission unless we explicitly state otherwise.

The distance of the shell from the supernova primarily affects the impact time, as one may expect, and has a small effect on the peak luminosity reached; the density of the shell primarily affects the luminosity and has a small effect on the impact time. When fractional width is held constant as is done when we vary impact radius and shell density, we see that the light curves have the same shape and are simply shifted around in $\log t - \log \mathcal{L}$ space, as can be seen in the middle and right panels of Figure 3.3.

In Figure 3.4 we show the light curves of our fiducial suite of numerical models (having different fractional widths, CSM densities, and impact times) normalized by their impact time and early-time luminosity. This view confirms that changing the impact radius and CSM density really does just shift the light curves in log-space and details of the light curve shape are governed by f_R alone.

For reference, we show in Figure 3.4 the slope of the radio light curve predicted by the self-similar model (Equation 3.38). While at later times the shell light curves approach the shallow slope of the self-similar model, at most times this slope does not describe the light curve. We also show the decay expected after peak from a simple analytic model that accounts for adiabatic losses in freely expanding gas (Equation 3.42). The analytic curve is shallower than the decline from our models, as the models accelerate and expand faster than free expansion immediately after shock breakout.

The similarity of the fiducial model set light curves is rooted in the fact that the models all have the same value of A_R, the initial ratio between the pre-shock CSM and ejecta density at the contact discontinuity (Equation 3.4). Our next step is to quantitatively define the family of light curves so that any light curve can be cheaply reconstructed for a given f_R and peak luminosity $\mathcal{L}_p$.

3.3.1 Parameterization of Light Curve Peak Time

First, we quantify how the fractional width of the shell, f_R, affects the timescale for the light curve to reach peak, t_p. The peak occurs when the forward shock radius (R_1) is equal to the outer shell radius, $[1 + f_R]R_{c,0}$ (see Equation 3.3). In the C82 self-similar solution, $R_1 = 1.131R_c$ and $R_c/R_{c,0} = (t/t_{\rm imp})^{0.7}$ for our choices of $n = 10$ and $s = 0$. This predicts

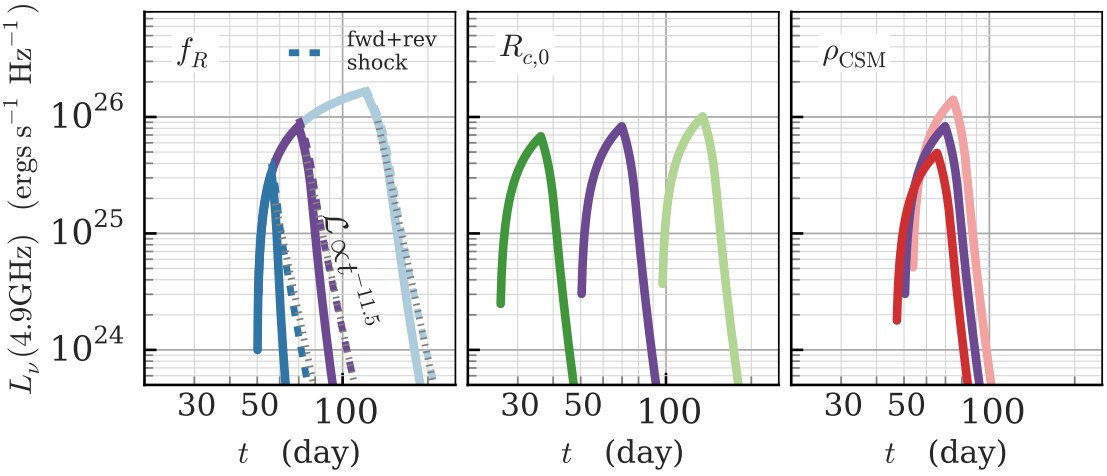

Figure 3.3: Dependence of the fiducial model radio light curves (at 4.9 GHz) on physical parameters. *Left panel:* Effect of varying the shell fractional widths from $f_R = \Delta R_{\rm CSM}/R_{c,0} = 0.1,\ 0.316,\ 1.0$. The light curve peak occurs at shock breakout, so wider shells reach higher luminosities and have broader light curves. The dashed lines show light curve calculations that include emission from the reverse shock region after peak. The dotted grey lines show the empirical fit described in § 3.3.2. *Center panel:* Effect of varying the initial impact radius from $R_{c,0} = 7.6 \times 10^{15},\ 1.2 \times 10^{16},\ 1.9 \times 10^{16}$ cm. Increasing $R_{c,0}$ increases the time of impact, but causes only a a small increases in the peak luminosity. *Right panel:* Effect of varying CSM density from $\rho_{\rm csm} = 3.8 \times 10^{-20},\ 6 \times 10^{-20},\ 9.6 \times 10^{-20}$ g cm^{-3}. Higher densities result in a higher peak luminosity, with a small effect on impact time (as expected from Equation 3.4).

that the time of peak is related to f_R through

$$f_R + 1 = 1.131 \left(\frac{t_p}{t_{\rm imp}}\right)^{0.7} \quad \Leftrightarrow \quad \frac{t_p}{t_{\rm imp}} = 0.839(f_R+1)^{1.43}. \tag{3.23}$$

If instead the shock is assumed to move at constant velocity (as is true in the early evolution before self-similarity is reached), $R_1/R_{c,0} = t/t_{\rm imp}$ so $t_p/t_{\rm imp} = 1 + f_R$.

Figure 3.5 shows $t_p/t_{\rm imp}$ versus (f_R+1) for our suite of numerical calculations, which we find are well fit with the power law

$$\frac{t_p}{t_{\rm imp}} = 1.11 \left(\frac{(f_R+1)}{1.1}\right)^{1.28}. \tag{3.24}$$

Unsurprisingly, the exponent $\alpha = 1.28$ lies between the self-similar ($\alpha = 1.43$) and free-expansion ($\alpha = 1$) predictions.

We find empirically that the peak luminosity depends on $R_{c,0}$ and $\rho_{\rm csm}$ in the way predicted by self-similar evolution (Equation 3.37) but with a different normalization than

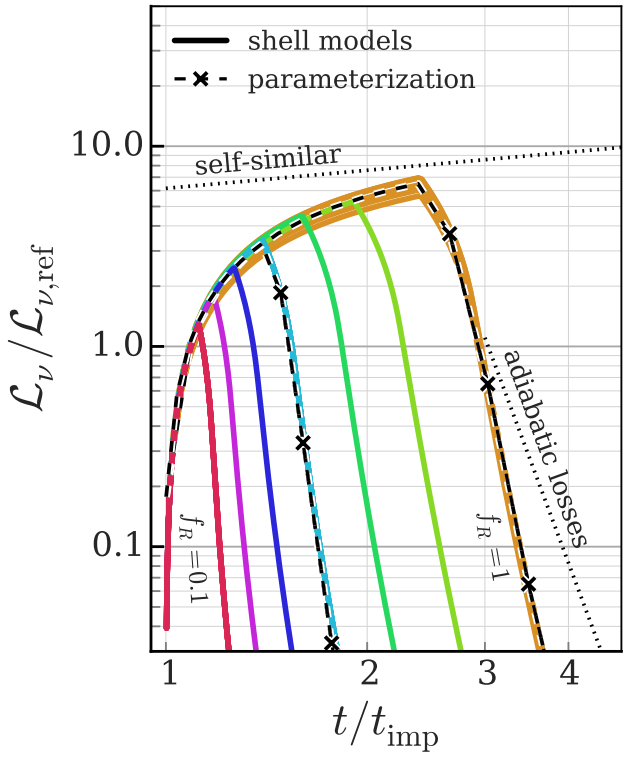

Figure 3.4: Light curves at 4.9 GHz with time normalized to the time of impact, $t_{\rm imp}$, and luminosity normalized to the luminosity at $1.09t_{\rm imp}$ ($\mathcal{L}_{\nu,\rm ref}$), when all light curves are rising. Curves are color coded by shell fractional width, $f_R = \Delta R_{\rm CSM}/R_{c,0}$, with logarithmic spacing between $f_R = 0.1$ and $f_R = 1$. Multiple models of varying $\rho_{\rm csm}$ and $t_{\rm imp}$ are shown for $f_R = 0.1, 0.316, 1.0$ (red, cyan, and orange, respectively) to demonstrate that the normalized light curves are nearly identical. Reconstructed light curves based on the empirical parameterization described in §3.3 are shown for $f_R = 0.316, .01$ (black dashed lines), and provide an excellent approximation to the hydrodynamical model light curves. The slopes predicted for self-similar evolution ($\mathcal{L} \propto t^{0.3}$, § 3.3.3) and for free expansion with adiabatic energy loss ($\mathcal{L} \propto t^{-9}$, § 3.3.3) are shown as dotted lines with arbitrary normalization; they do not capture the shape of these light curves.

predicted by that relation. For the $f_R = 1$ light curves the best-fit peak luminosity is

$$\mathcal{L}_{\nu,p}|_{f_R=1} \approx (1.9 \times 10^{30}\ \mathrm{erg\ s^{-1}\ Hz^{-1}}) \left(\frac{\nu}{\mathrm{GHz}}\right)^{-1} \rho_{\mathrm{CSM},-18}^{8/7}\ R_{c,0,16}^{3/7}\ , \tag{3.25}$$

where $R_{c,0,16} = R_{c,0}/(10^{16}\ \mathrm{cm})$ is the scaled initial contact discontinuity radius. The peak luminosity of thinner shells – which as we see in Figure 3.3 peak at a lower luminosity because shock breakout occurs sooner – can be found with a parameterization of the light curve rise, given below.

3.3.2 Parameterization of Light Curve Rise and Fall Times

To fit the light curve rise, we note that all light curves follow the same rise shape up until the time of peak. A function of the form $\mathcal{L} = a - b/t$ fits the rise of $f_R = 1$ light curves well, with

$$\mathcal{L}_\nu(t) = 1.705 \;\; \mathcal{L}_{\nu,p}|_{f_R=1} \left[1 - 0.985 \left(\frac{t}{t_{\rm imp}}\right)^{-1}\right] \;, \tag{3.26}$$

so using Equation 3.25 the rise of fiducial model light curves is

$$\mathcal{L}_\nu(t) = (3.2\times10^{28}\ {\rm erg\ s^{-1}\ Hz^{-1}}) \left(\frac{\nu}{\rm GHz}\right)^{-1} \rho_{\rm CSM,-18}^{8/7}\, R_{c,0,16}^{3/7} \left[1 - 0.985 \left(\frac{t}{t_{\rm imp}}\right)^{-1}\right] \;. \tag{3.27}$$

If desired, the peak luminosity of *any* fiducial model can be found by substituting Equation 3.24 into Equation 3.27,

$$\mathcal{L}_{\nu,p,\rm ss} \approx (3.2\times10^{28}\ {\rm erg\ s^{-1}\ Hz^{-1}}) \left(\frac{\nu}{\rm GHz}\right)^{-1} \rho_{\rm CSM,-18}^{8/7}\, R_{c,0,16}^{3/7} \left[1 - (1+f_R)^{-1.28}\right] \;. \tag{3.28}$$

To describe the light curve decline, we choose four characteristic times along the fall: the time to fall a factor of $10^{-1/4}$ ($\sim 50\%$), 10^{-1}, 10^{-2}, and 10^{-3} of $\mathcal{L}_{\nu,p}$. As demonstrated in Figure 3.5 for the $\mathcal{L} = 10^{-1}\mathcal{L}_{\nu,p}$, case, these characteristic times follow a power law in $(f_R + 1)$,

$$\frac{t}{t_{\rm imp}} = Q \left(\frac{f_R+1}{1.1}\right)^{\alpha} \;, \tag{3.29}$$

with fit parameters Q and α given in Table 3.1. Between characteristic points, we interpolate light curves linearly in $\log(\mathcal{L}) - \log(t)$ space (Figure 3.4).

Putting the parameterized rise and fall expressions together, one can create an approximate light curve for any peak luminosity and shell width; the reconstruction will be a good approximation to the full numerical calculation, as shown in Figure 3.4. Finally, as mentioned previously, the decline of the light curve is modified when one includes a contribution from the reverse shock (Figure 3.3). Empirically, we find that the light curve at times later than the characteristic point $10^{-1/4}\mathcal{L}_{\nu,p}$ declines like $\mathcal{L}_\nu \propto t^{-11.5}$, which when combined with the equation for time to decline to $10^{-1/4}\mathcal{L}_{\nu,p}$ (Table 3.1) yields

$$\mathcal{L}_{\nu,(\rm f+r)} = 0.67\mathcal{L}_{\nu,p}\ (f_R+1)^{16}\ (t/t_{\rm imp})^{-11.5} \;, \tag{3.30}$$

where the subscript "f+r" indicates the luminosity of the light curve including both the forward and reverse shock components while $\mathcal{L}_{\nu,p}$ is as given in Equation 3.28. We illustrate this fit in the left panel of Figure 3.3.

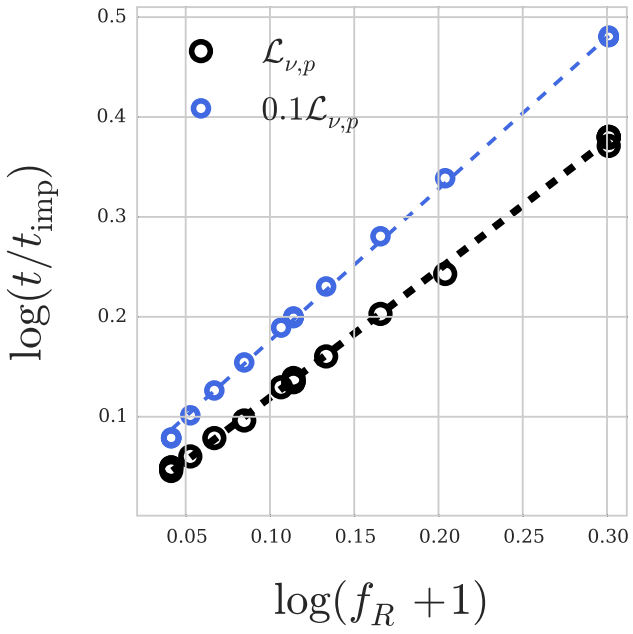

Figure 3.5: Time of peak (black) and time to fall to 10% $\mathcal{L}_{\nu,p}$ (blue) normalized to impact time versus the fractional width of the shell, f_R (Equation 3.3) for our fiducial model suite (open circles). Broader shells (i.e., higher f_R) have broader light curves (as illustrated in Figure 3.4). This trend is well fit by a power law (dashed lines), which forms the basis for the parameterization of a fiducial model light curve. Fit parameters for the power law of Equation 3.29 are given in Table 3.1.

3.3.3 Comparison to Other Predictions

Self-Similar Evolution Light Curve

Next we use the synchrotron emissivity to calculate the luminosity predicted from the C82 self-similar evolution. In the case of constant-density CSM, we can use our model parameters (see § 3.1, particularly Equation 3.1) in Equation 3 of C82 to derive that a self-similar shock has speed

$$R_1 = 1.131 R_c \tag{3.31}$$

$$\Rightarrow\ v_s = dR_1/dt = 0.792 R_c\ t^{-1} = 0.502\ (M_{\rm ej}\ v_t^7)^{1/7}\ R_c^{-3/7} \rho_{\rm csm}^{-1/7}\ , \tag{3.32}$$

where R_1 is the radius of the forward shock front, v_s is the shock velocity, and as usual $\rho_{\rm csm}$ is the preshock CSM density and R_c is the radius of the contact discontinuity. Substituting this into Equation 3.14,

$$u_{\rm gas} = 1.125\ \rho_{\rm csm} v_s^2 = 0.284\ (M_{\rm ej}\ v_t^7)^{2/7}\ R_c^{-6/7}\ \rho_{\rm csm}^{5/7}\ . \tag{3.33}$$

Table 3.1: Parameters for Equation 3.29

Luminosity	Q	α
peak ($\mathcal{L}_{\nu,p}$)	1.11	1.28
$\mathcal{L}_{\nu,p}/2$	1.16	1.39
$\mathcal{L}_{\nu,p}/10$	1.22	1.52
$\mathcal{L}_{\nu,p}/100$	1.32	1.62
$\mathcal{L}_{\nu,p}/1000$	1.48	1.70

Note: Using Q and α in Equation 3.29 will return the $t/t_{\rm imp}$, as a function of f_R, at which a given luminosity (first column) is reached.

Thus the emissivity (Equation 1.20, with $\rho = 4\rho_{\rm csm}$), assuming fully ionized hydrogen gas, evolves like

$$j_\nu = 0.092 \, \frac{\sigma_T m_p}{12\pi m_e^2 c^3} \, (M_{\rm ej} \, v_t^7)^{6/7} \, \epsilon_e^2 \, \epsilon_B \, \nu^{-1} \, R_c^{-18/7} \, \rho_{\rm csm}^{8/7} \, , \tag{3.34}$$

and the emitting volume increases like

$$V = \frac{4\pi}{3}(R_1^3 - R_c^3) = 1.871 R_c^3 \, , \tag{3.35}$$

which together produce

$$\mathcal{L}_{\nu,\rm ss} \sim j_\nu V \sim 0.17 \, \frac{\sigma_T m_p}{12\pi m_e^2 c^3} \, (M_{\rm ej} \, v_t^7)^{6/7} \, \epsilon_e^2 \, \epsilon_B \, \nu^{-1} \, R_c^{3/7} \, \rho_{\rm csm}^{8/7} \, . \tag{3.36}$$

For our model parameters of $M_{\rm ej} = 1.38 \, M_\odot$, $v_t = 1.022 \times 10^9$ cm s^{-1}, $\epsilon_e = \epsilon_B = 0.1$,

$$\mathcal{L}_{\nu,\rm ss} \sim (2.3 \times 10^{29} \text{ erg s}^{-1} \text{ Hz}^{-1}) \, \left(\frac{\nu}{\rm GHz}\right)^{-1} \, R_{c,16}^{3/7} \, \rho_{\rm CSM,-18}^{8/7} \, , \tag{3.37}$$

where $R_{c,16} = R_c/(10^{16} \text{ cm})$ is the current contact discontinuity radius and $\rho_{\rm CSM,-18} = \rho_{\rm csm}/(10^{-18} \text{ g cm}^{-3})$. From Equation 3.4, we see that $R_c^{3/7} \propto t^{3/10}$, so the scaling of luminosity with time is

$$\mathcal{L}_{\nu,\rm ss} \propto t^{0.3} \, . \tag{3.38}$$

Adiabatic Losses Light Curve

After several dynamical times (Equation 3.6) have passed since shock breakout, the system should have relaxed into a state of free expansion, with $R \propto t$. In this state, we expect

adiabatic evolution of the gas,

$$V \propto R^3 \propto t^3 \tag{3.39}$$

$$p \propto V^{-5/3} \Rightarrow u_{\rm gas} \propto V^{-5/3} \propto t^{-5} \ . \tag{3.40}$$

This produces a deline in the emissivity

$$j_\nu \propto \rho^{-1} \, u_{\rm gas}^3 \propto t^{-12} \ , \tag{3.41}$$

so in this state of free expansion we have

$$L_\nu \propto j_\nu V \propto t^{-9} \ . \tag{3.42}$$

This explains why the decline in the radio light curves is so steep after shock breakout.

3.4 Effect of Maximum Ejecta Velocity

In our simulations we must choose an initial radius (equivalently, velocity) at which to truncate the ejecta, $R_{c,0} = v_{\rm ej,max} t_{\rm imp}$. The fiducial model set is defined by $R_{c,0} = R_{c,0,\rm ss}$ (Equation 3.4), so the maximum velocity is

$$v_{\rm ej,max,ss} = R_{c,0,\rm ss} \, t_{\rm imp}^{-1} = (2 \times 10^9 \text{ cm s}^{-1}) \, R_{c,0,16}^{-3/7} \, \rho_{\rm CSM,-18}^{-1/7} \ , \tag{3.43}$$

with $R_{c,0,16} = R_{c,0,\rm ss}/(10^{16} \text{ cm})$. Early-time spectra of normal SNe Ia show ejecta with maximum velocities $v_{\rm ej,max} \approx 30,000$ km s^{-1} (Parrent et al., 2012; Silverman et al., 2015), and we take $v_{\rm ej,max} = 45,000$ km s^{-1} as an upper limit. One could constrain oneself to fiducial models in this velocity range, but as illustrated in Figure 3.1 that is a narrow band of models. Considering that the ejecta velocity is one of the most important constraints on SN Ia explosion models, we wanted to explore the effect of ejecta with $v > v_{\rm ej,max,ss}$ on our light curves. We call these "high-velocity models," although they could also be thought of as "super-A_R" models, as they have a higher initial CSM to ejecta density than the fiducial model value $A_R = 0.33$. Note that these models are not plotted on Figure 3.1, to avoid confusion regarding the reference lines that apply only to fiducial models.

Figure 3.7 shows the hydrodynamic evolution for a high-velocity model analogue of the model shown in Figure 3.2. The fiducial model of Figure 3.2 was initialized with $\rho_{\rm csm} = 10^{-18}$ g cm^{-3} and $R_{c,0} = 10^{16}$ cm, which implies $v_{\rm ej,max} \approx 20,000$ km s^{-1} and $t_{\rm imp} = 57.7$ days. The high-velocity model Figure of 3.7 has the same CSM properties but $v_{\rm ej,max} = 30,000$ km s^{-1}, thus it has $t_{\rm imp} \approx 38.6$ days ($A_R = 1.00$). The high-velocity model has a lower initial ram pressure, since at a fixed radius $\rho_{\rm ej} \propto t^7 \propto v^{-7}$ (Equation 3.1) and $p_{\rm ram} \propto \rho_{\rm ej} v^2 \propto v^{-5}$; therefore the forward shock is slower and the light curve takes a few hours longer to reach peak (time of shock breakout; Figure 3.7, panel B).

Example light curves of high-velocity models with varying f_R are presented in Figure 3.6, along with their fiducial model counterparts. Including the higher velocity ejecta leads to

light curves that are broader, dimmer, and peak earlier. As discussed, the effect on breadth is because the shock is slower so it takes longer to cross the shell. The dimming is also due to the lower shock speed (Equations 3.14 and 1.20). That the light curves peak earlier relative to explosion time is simply due to the earlier impact time.

The offsets in peak luminosity and time of peak are more pronounced in thinner shell models, both in absolute and relative terms. Therefore we decided to apply the fiducial model relations of §3.3 to see how well they recover shell properties from the $f_R = 0.1$ high-velocity model. If the $v_{\rm ej,max} = 30,000$ km s^{-1} light curve had been observed, one would calculate that $f_R = 0.2$ (Equation 3.24), $\rho_{\rm csm} = 1.2 \times 10^{-18}$ g cm^{-3}, and $R_{c,0} = 7.5 \times 10^{15}$ cm (Equations 3.4 and 3.28) – all correct to within a factor of a few.

Overall, we conclude that one can still apply the fiducial model relations to an observed light curve to reasonably estimate CSM properties even if the derived parameters yield a $v_{\rm ej,max,ss}$ that is below the observed ejecta velocity, $v_{\rm ej,o}$. Therefore, in the next section, we will take the liberty of applying the fiducial relations to the analysis of SNe Ia radio non-detections.

3.5 Observational Constraints

In this section we use the radio observations of SN 2011fe from Chomiuk et al. (2012, hereafter CSM12) and of SN 2014J from Pérez-Torres et al. (2014, hereafter PT14) to illustrate how our models can be used to interpret radio nondetections in SNe Ia. As detailed below, we do this by calculating a suite of parameterized light curves relevant to the observations, determining if each would be observed, then converting these observation counts into observation likelihoods.

The analysis begins by defining the set of observations. CSM12 observed SN 2011fe in two bands with effective frequency $\nu = 5.9$ GHz at times after explosion $t_{\rm exp} = 2.1 - 19.2$ days, with luminosity limits $\sim 10^{24}$ erg s^{-1} Hz^{-1} for each observation. To interpret these observational constraints, we generate 10^6 light curves corresponding to different interaction models by log-uniform randomly distributed sampling of peak luminosity, shell width, and impact time with values in the range $\mathcal{L}_{\rm p}(5.9\ {\rm GHz}) \in [10^{24}, 10^{27})$ erg s^{-1} Hz^{-1}, $f_R \in [0.1, 1)$, and $t_{\rm imp} \in [2, 19)$ days. For each light curve, we then determine if it was observed, i.e., if it was above the CSM12 luminosity limit for any single observation. We restrict ourselves this way since if the shell had been observed it would have affected the observation schedule; but using our models one could interpret stacked datasets as well. Finally, we bin the light curves in f_R and $\mathcal{L}_p$ and in each bin calculate the probability that it would have been observed (the ratio of the number of light curves observed to the number sampled). The probability of the light curve appearing in any single observation is shown in Figure 3.8.

CSM12 attempted to estimate, without using explicit shell light curve models, the probability of detecting a specific CSM shell. The shell they considered had fractional width $f_R \approx 0.1$, mass $6 \times 10^{-8}\ M_\odot$ (from a wind of $\dot{M} = 2 \times 10^{-7}\ M_\odot$ yr^{-1}), and sat at $R \approx 5 \times 10^{15}$ cm; the authors estimated a 30% chance of detecting the shell. The preshocked CSM density

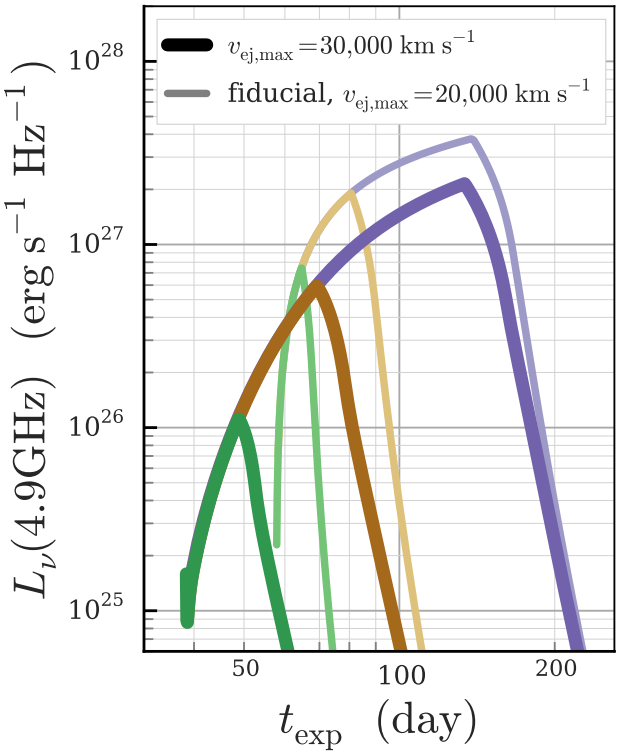

Figure 3.6: Light curves at 4.9 GHz, comparing fiducial models (§3.1; $t_{\rm imp} = 57.7$ days, $v_{\rm ej,max} = 20,000$ km s^{-1}, light thin) to "high-velocity ejecta" models (§3.4; $v_{\rm ej,max} = 30,000$ km s^{-1}, $t_{\rm imp} = 38.6$ days, dark thick). The CSM shell widths shown are: $f_R = 0.1$ (green, narrowest light curves), $f_R = 0.316$ (brown), and $f_R = 1$ (purple, broadest light curves). All models have $\rho_{\rm csm} = 10^{-18}$ g cm^{-3}. Decreasing the ejecta density relative to CSM (i.e., increasing maximum velocity) lowers the peak luminosity and causes the light curve to peak at an earlier time since explosion. However, the effect is negligible for thick shells, and even for thinner shells the fiducial relations can estimate shell properties.

is

$$\rho_{\rm csm} = (4.7 \times 10^{-24}\ {\rm g\ cm^{-3}})\ M_{-8}\ R_{16}^{-3}\left[(1+f_R)^3 - 1\right]^{-1}\ , \tag{3.44}$$

where $M_{-8} = M_{\rm CSM}/(10^{-8}\ M_\odot)$ and $R_{16} = R/(10^{16}$ cm). We estimate that the shell described by CSM12, which has $M_{-8} = 6$, $R_{16} = 0.5$, and $\rho_{\rm csm} \approx 7 \times 10^{-22}$ g cm^{-3}, would have a peak luminosity (Equation 3.28) $\mathcal{L}_{\nu,p}(5.9\ {\rm GHz}) \approx 6 \times 10^{22}$ erg s^{-1} Hz^{-1}, and would be undetected in their observations. For reference we note that at our assumed distance and width, a shell would need to have $M_{-8} \approx 600$ to have $\sim 50\%$ chance of detection.

For SN 2014J, we will demonstrate how one can instead analyze the probability of observing a shell of a given density, rather than peak luminosity. The observations of SN 2014J by Pérez-Torres et al. (2014) span the range 8.2-35.0 days. Using the observation times,

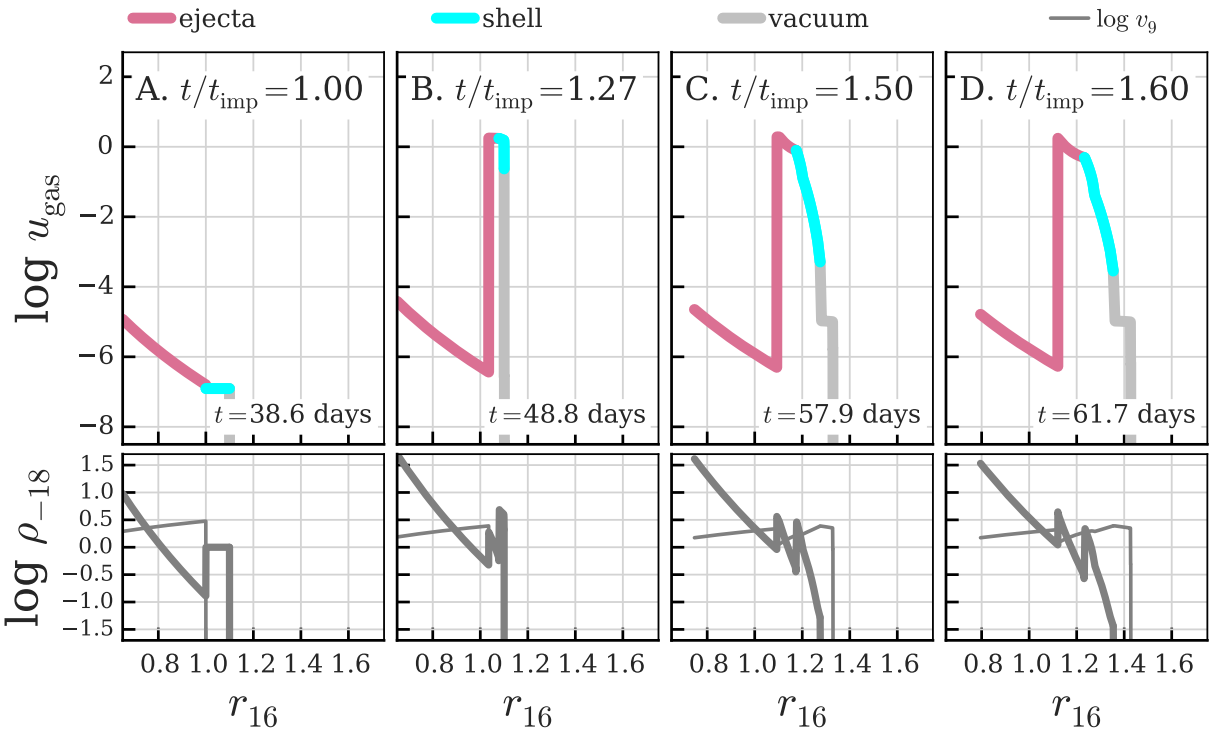

Figure 3.7: Same as Figure 3.2 but for a "high-velocity" initial conditions model with $v_{\rm ej,max} = 30,000$ km s^{-1} ($t_{\rm imp} = 38.6$ days) and the same CSM as in Figure 3.2. Compared to a fiducial model, the ejecta are less dense at the initial point of contact; so the shock is slower, shock breakout happens later, and the CSM does not gain as much energy.

frequencies, and limits from PT14 Table 1, we perform the same random sampling test as for SN 2011fe described above, but with a peak luminosity range 10^{23-28} erg s^{-1} Hz^{-1} at 1.55 GHz (their lowest frequency band) and impact times between 2 and 35 days. Isolating the $f_R = 0.1$ bin, we can convert luminosity to density and analyze the probability that the authors would have observed an impact with a shell of a given $\rho_{\rm csm}$ that occurred during their observations, illustrated in Figure 3.9. The same shell considered for CSM12 but at $R = 10^{16}$ cm, to account for the later observation time, would again escape detection at $\rho_{\rm csm} \approx 10^{-22}$ g cm^{-3}.

As we have shown here, by using the parameterized light curves and fiducial model relations one can easily quantify the probability of detecting shells spanning a range of f_R and $\rho_{\rm csm}$ for a given set of observations. Alternatively, one could constrain for instance the ejecta velocity and f_R, and use Equation 3.43 to analyze the likelihood of detecting shells of varying radii and densities.

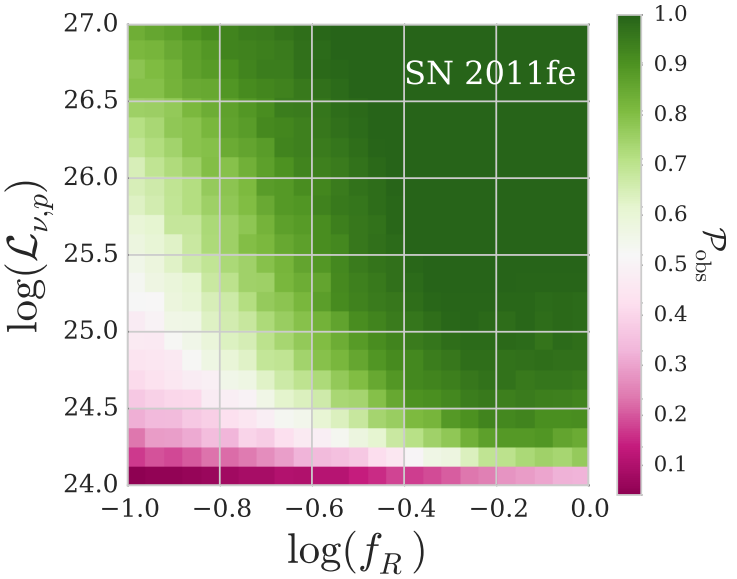

Figure 3.8: Probability that the CSM12 cadence would observe a light curve ($\mathcal{P}_{\rm obs}$) with peak luminosity $\mathcal{L}_{\nu,p}$(5.9 GHz) from a shell of fractional width f_R (Equation 3.3) for a set of light curves that have log-uniform randomly assigned values of $\mathcal{L}_{\nu,p} \in [10^{24}, 10^{27})$ erg s^{-1} Hz^{-1}, $f_R \in [0.1, 1)$, and $t_{\rm imp} \in [2, 19)$ days. For a given f_R and initial shell radius, peak luminosity can be converted into CSM density using Equation 3.28 as is done in Figure 3.9 for SN 2014J.

3.6 Multiple Shell Collisions

We have demonstrated that the light curves of ejecta impacting a single shell form a family of solutions that can be straightforwardly applied to the interpretation of radio observations. In these simulations, we assume that there is negligible CSM interaction prior to the interaction being considered – i.e., the space between the supernova progenitor and the CSM shell is empty. However, it is natural to wonder how it would look if one shell collision were followed by another: could we simply add the light curves, preserving their convenient properties? In this section we perform this experiment and show that the light curves from multiple shell collisions differ dramatically from a simple addition of two single-shell light curves.

Imagine a system with two thin ($f_R = 0.1$) CSM shells: Shell 1 at 9.2×10^{14} cm with $\rho_{\rm csm} = 8.8 \times 10^{-15}$ g cm^{-3} and Shell 2 at 7.7×10^{15} cm with $\rho_{\rm csm} = 4.7 \times 10^{-18}$ g cm^{-3}. The ejecta impact Shell 1 at 5 days in a self-similar model, and if Shell 1 were not present the ejecta would impact Shell 2 at 50 days; therefore, models of the *single-shell* impact with these shells are called "1sh5" (Shell 1) and "1sh50" (Shell 2). The double-shell model ("2sh27") is the same as 1sh5 until Shell 1 impacts Shell 2 on day 27. Note that the earlier impact time (27 days versus 50 days) is due to the fact that this second interaction starts not when the

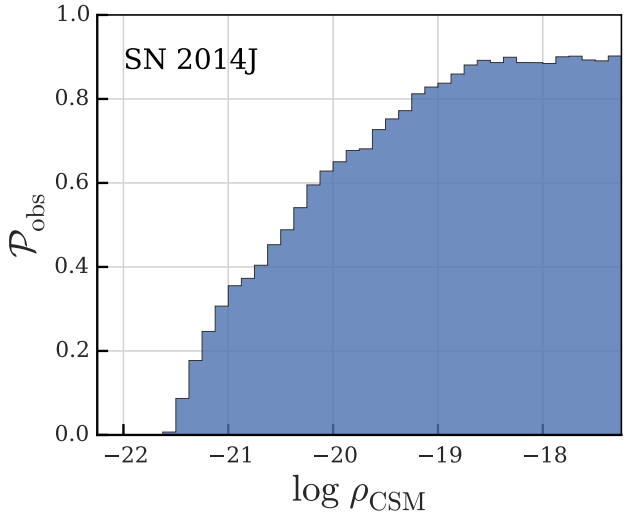

Figure 3.9: Probability ($\mathcal{P}_{\rm obs}$) that any single radio observation of Pérez-Torres et al. (2014) would detect a thin CSM shell ($f_R = 0.1$) of a given mass density ($\rho_{\rm csm}$) around SN 2014J if impact occurred during their observation window, 8.2-35.0 days.

ejecta impact Shell 2 but rather when *Shell 1* does, which happens earlier since Shell 1 is exterior to the ejecta. The initial condition of 2sh27 is the day-27 state of 1sh5 for $r < R_{1-2}$ plus the initial state of 1sh50 for $r > R_{1-2}$, where R_{1-2} is the contact discontinuity radius between the shells. The number of zones in the 1sh50 CSM was adjusted to match the mass resolution of 1sh5.

Figure 3.10 shows that the 2sh27 light curve is dramatically different than those of 1sh5 and 1sh50. First, the 2sh27 light curve is strikingly flat and broad, maintaining a luminosity similar to the peak luminosity of 1sh50 for nearly twenty days. Second, the light curve has an elbow at $t_{\rm exp} = 41$ days (time C; corresponding to panel C of Figure 3.11). Note that in this figure, the 1sh5 light curve would in fact be subject to synchrotron self-absorption, an effect that we neglect here because it is not the interesting part of the evolution.

Since our 1-D simulations do not have mixing, we can calculate the luminosity contribution from the Shell 1 and Shell 2 zones separately (which zones belong to each shell is known by construction, as illustrated in Figure 3.11). When separated into the contribution from each shell, we see that the light curve is dominated by the signal from Shell 1. This is simply because of the chosen frequency of $\nu_{\rm obs} = 4.9$ GHz; in our model the ratio of cyclotron frequency in Shell 2 to Shell 1 is $\nu_{c,{\rm sh2}}/\nu_{c,{\rm sh1}} \sim 2\%$, thus $L_{\nu,{\rm sh2}}/L_{\nu,{\rm sh1}} \sim 2\%$. The Shell 2 light curve also has an elbow (time E; $t_{\rm exp} = 44$ days) that occurs later than the Shell 1 elbow. Finally, both the Shell 1 and Shell 2 light curves start their final decline at $t_{\rm exp} = 49$ days (time F).

This complicated light curve is caused by "sloshing" of shocks in Shell 1 which re-energize

the gas for ~ 27 days, the dynamical time (§ 3.1.1) This "sloshing" can be seen in snapshots of the simulation at critical times (Figure 3.11). Remember that Shell 1 dominates the signal in the following narrative of the interaction: (A) *Impact.* Shell 1 is much less dense than either the ejecta or Shell 2, and it is approaching Shell 2 at high speeds. (B-C) *Shock moves leftward through Shell 1.* When Shell 1 hits the "wall" of Shell 2, a shock forms. It energizes Shell 2 in a way reminiscent of single-shell evolution, breaking out quickly. (D) *Shock forms at ejecta-Shell 1 boundary and re-energizes Shell 1.* Because of the new shock, $u_{\rm gas}$ increases and the light curve has another small rise. (E) *Shock forms at the Shell 1-Shell 2 boundary, re-energizing both shells.* We see that when the shock moving through Shell 1 (seen in panel D) hits Shell 2, a new shock forms. The Shell 2 light curve begins a dramatic second rise and Shell 1 is able to maintain its luminosity. (F) *After a dynamical time the system has had time to adjust and the light curve begins to decline.* This panel shows a snapshot just before the decline of both light curves. Minor shocks continue to slosh inside Shell 1 between the ejecta and Shell 2, causing the more gradual light curve fall compared to single-shell models.

This is just one possible configuration of a double-shell system and its evolution probably does not generalize to the whole class of such collisions; however, it illustrates that the evolution of these systems is distinct from single-shell model evolution and so produces a radically different light curve. Note that higher-dimensional simulations may be required for investigating this class further because the significance of the "shock slosh" could be diminished by turbulence.

3.7 Conclusions

In order to quantitatively interpret the radio light curves and spectra of interacting SNe, one needs to understand the evolution of the shocked gas. One popular model for shock evolution is the Chevalier (1982a, "C82") one-dimensional self-similar interaction model, which assumes a continuous CSM. Here we explored moving beyond these models to the case of CSM shells (e.g., due to novae) in the low-density case where the shocked CSM does not cool and is optically thin. This removes the self-similar model assumption that the interaction has had time to reach self-similarity (i.e. that the CSM is close to the progenitor star or is very extended).

We created a suite of models to explore the parameter space of shell properties, focusing on shell density, thickness, and time of impact. In our "fiducial" models, we enforce an initial CSM-to-ejecta density ratio of $A_R = 0.33$ at the contact discontinuity (motivated by C82; Equation 3.4) . If the shell were infinite, these models would evolve to the C82 self-similar solution (§3.1); however, because of the finite extent of the shells, self-similarity is never reached in our models.

We calculated synchrotron radio light curves for these models, since this emission traces the evolution of the shocked region only. We found a similar behavior among the radio light curves of fiducial models – they peak at a predictable time (Equation 3.24), have the same shape (Equation 3.27), and peak at a luminosity that can be calculated from shell

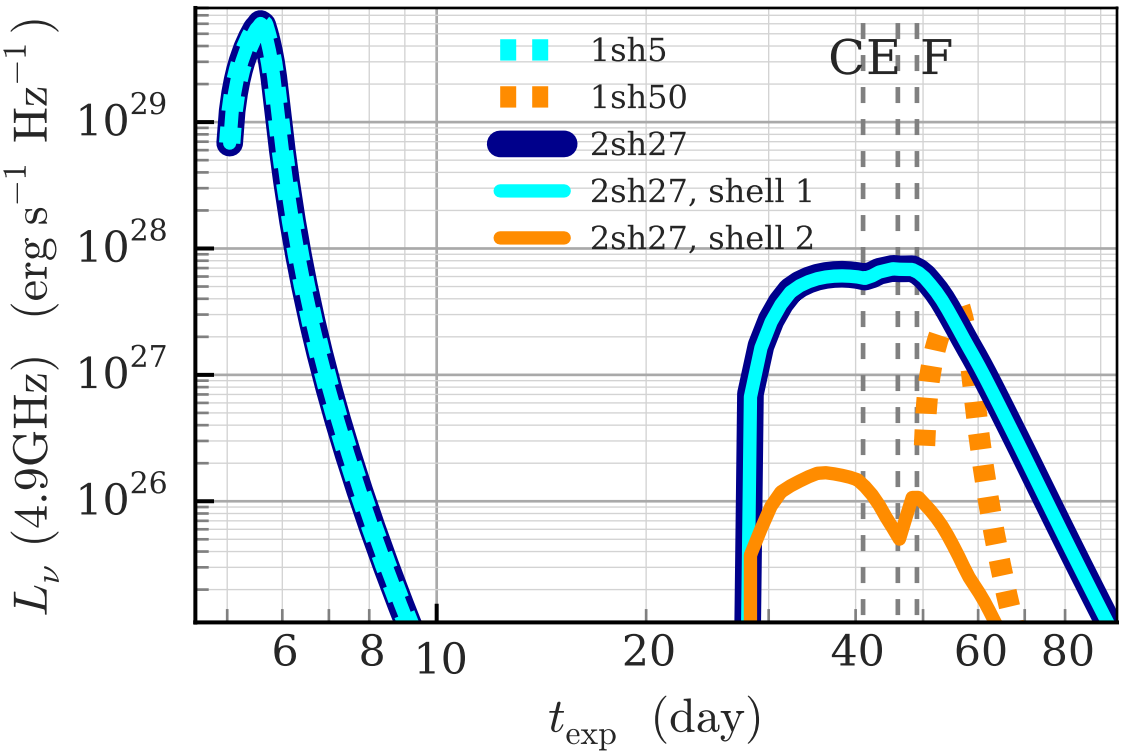

Figure 3.10: 4.9 GHz light curve of the two-shell model 2sh27 (navy). It can be broken down into the radiation from Shell 1 (cyan thin) and Shell 2 (orange thin); after impact with Shell 2, the signal from Shell 1 dominates in this band because the Shell 2 synchrotron spectrum peaks at a much lower frequency than Shell 1. Thick dashed lines show single-shell models: the light curves that would result from assuming that Shell 1 (1sh5; cyan; assuming optically thin to SSA) or Shell 2 (1sh50; orange) was the only shell in the system; simply summing these light curves is not at all a good approximation to the behavior of the two-shell system after impact with Shell 2. Compared to 1sh50, 2sh27 has a longer-lived and brighter light curve, with a plateau that lasts a couple of weeks and a more gradual decline. Dashed vertical lines indicate important features in the light curve: the elbow in Shell 1 (C), elbow in Shell 2 (E), and time of final descent (F), with letters corresponding to panels in Figure 3.11.

characteristics (Equation 3.28). Therefore these light curves can be parameterized in a way that allows CSM properties to be inferred readily from an observed light curve (§3.3). In fact, we find that shell properties can be approximated even if there is a higher initial density ratio (i.e., faster, lower-density ejecta colliding with the shell) than is assumed in the fiducial set (§3.4).

We then showed how one can use the fiducial models to better interpret radio non-detections of SNe Ia by applying our work to the radio observations of SN 2011fe and SN

2014J (§3.5).

We presented a two-shell model to illustrate that our single shell light curves do not apply in that case, as a double shell light curve is much longer lived because of an effect that we call "shock sloshing" that occurs in the first shell (§3.6). Shock sloshing produces elbows in the light curve that may be an observable signature of this behavior; exploring the diversity in multiple shell collisions is an enticing direction for future work.

Our fiducial model set is a new tool for studying the interaction of SNe Ia with a CSM, with the goal of constraining the supernova progenitor system. With the fiducial set, one can easily make observational predictions and analyze radio observations. Future work will focus on calculations of the radiation transport in the optical and x-ray, to show how data at those wavelengths can reinforce radio constraints on supernovae interaction.

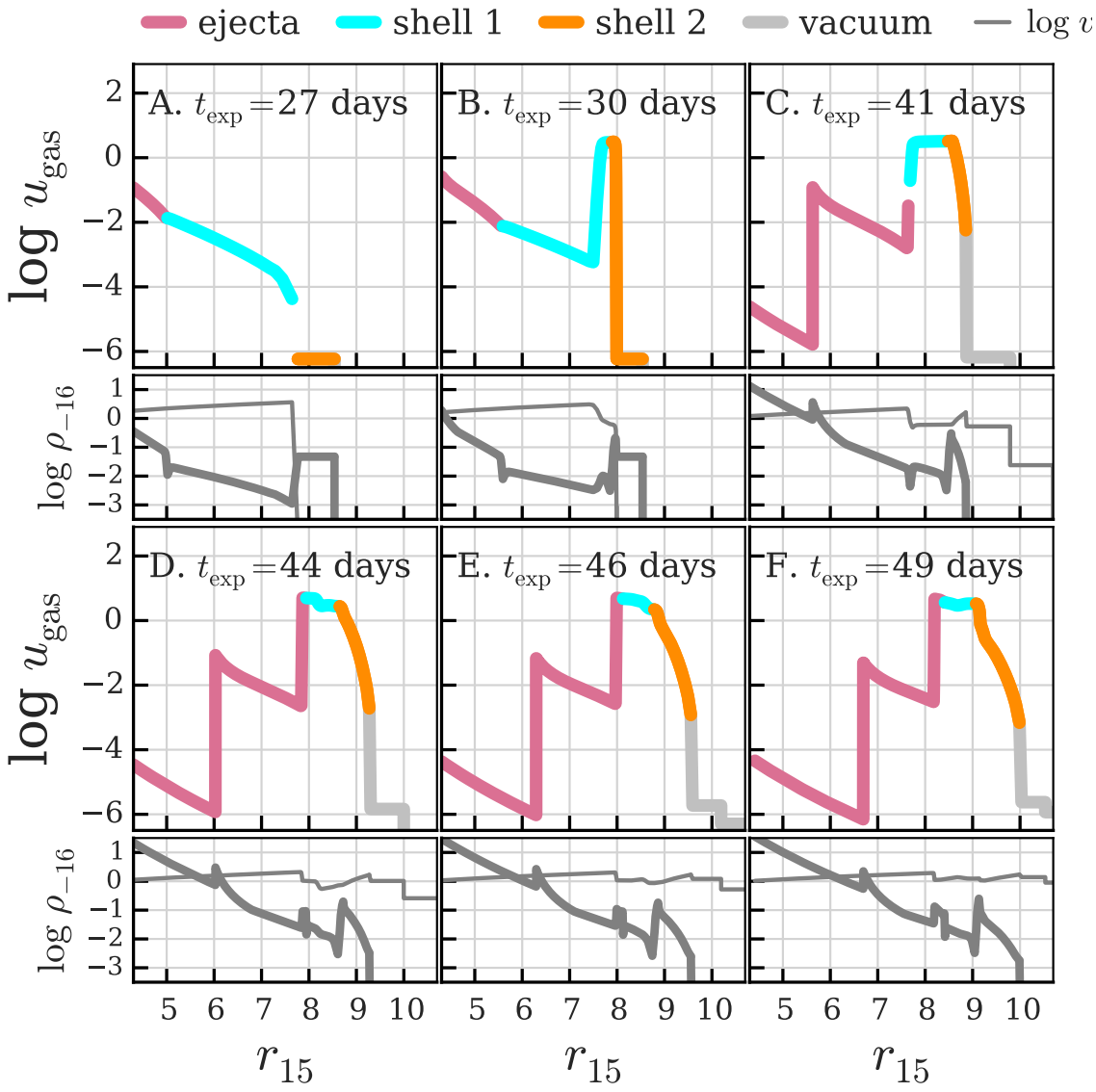

Figure 3.11: Like Figure 3.2. Snapshots of 2sh27 (two-shell model) at important times in its evolution, showing $u_{\rm gas}$ in the ejecta (pink), Shell 1 (cyan), Shell 2 (orange), and the vacuum (light grey). The energy density in Shell 1 stays high because of "shock sloshing": the recurring formation of shocks in Shell 1 caused by a shock front reaching either the ejecta on the left or Shell 2 on the right and forming a new shock front in Shell 1 that travels the opposite direction.

Chapter 4

What the H? Modeling the Type Ia;n Supernova PTF11kx at Late Times

I first journeyed out of the radio to explore the data of PTF11kx. This chapter will describe my work published in Graham et al. (2017b), in which I explored how the x-ray emission from hot ejecta could continue to heat post-shock CSM. This is a brief chapter, but the modeling I performed to investigate the late-time emission for PTF11kx informed the observational efforts for SN 2015cp which will be the subject of the next chapter.

4.1 Surprising Detections of PTF11kx at 3.5 Years

PTF11kx was the first SN Ia;n whose delayed interaction was observed both photometrically and spectroscopically (Dilday et al., 2012, hereafter D12). Taking its peak to be 13 days after explosion (first light), the onset of interaction was around 50 days [post-explosion]. The lack of radio emission prior to 50 days supports the idea that the CSM was in a shell at $\approx 10^{16}$ cm, with an evacuated cavity interior to the shell, like the situations I model. D12 present multi-band photometry, low-resolution and high-resolution spectra for PTF11kx from nearly the time of explosion to 103 days, with spectra starting at 12 days. They also report an early time radio non-detection.

Silverman et al. (2013b) subsequently observed PTF11kx from 137 days to 693 days with low-resolution optical spectroscopy. The behavior of the Hα line was of particular interest. Hα had two components, narrow and broad, with the broad component being only $\sim 4,000$ km s^{-1} in width at zero intensity. In Figure 3 of that paper, it is clear that the broad-line luminosity rises between 137 and 283 days. Between 283 days and 449 days, the luminosity plateaus. The 693 day observation shows that it has once again dropped to a value slightly lower than its 137 day value. The authors take this as evidence that interaction is over: the shock has swept over the majority of the CSM. The reasoning is that the broad Hα is the product of cooling post-shock CSM, so its luminosity will decline unless the store of hot gas is replenished (to cool). This then limits the interaction of PTF11kx to have

ended sometime between 449 and 693 days after explosion.

Graham et al. (2017b) obtained a spectrum of PTF11kx at 1355 days after explosion, nearly two years after the last Silverman et al. (2013b) spectrum. It was a surprise – at least in some quarters – to find that Hα was still visible at this epoch, which required the line luminosity decline rate to have slowed since the last observation. However, it is not entirely unheard of in the case of SNe IIn: the authors show that the decline rate of PTF11kx between 693 and 1355 days is similar to that observed for the Type IIn SN 1988Z and SN 1998S.

Typically, the continued Hα emission is explained as continued interaction (e.g., Smith et al., 2017). I thought this scenario was worth investigating, however, because invoking continued interaction necessarily increases the CSM mass, and has important consequences for the interpretation of the progenitor. Also, for PTF11kx there was no evidence besides the optical to support a claim that interaction was ongoing; and as I alluded to in §1.3 optical lines are the most difficult to interpret of all shock signatures. What piqued my interest was the fact that in the radio I had found that, unlike what had been naïvely assumed before, the emission persisted after the shock had swept through the CSM because it traced the reverse shock which continued to slowly propagate through the ejecta. My thought was that perhaps similarly the ejecta continues to ionize the hydrogen in the CSM to force continued recombination in the CSM.

4.2 Obtaining Model Initial Conditions from Optical Observations

D12 use high-resolution spectra of PTF11kx obtained at peak brightness, before the onset of interaction, to measure the equivalent width ($W_{\rm CaII}$) of the blueshifted, saturated Ca II H & K lines ($\lambda_{\rm CaII,H} = 3968.47$, $\lambda_{\rm CaII,K} = 3933.66$), from which they estimate the column density of calcium to be $N_{\rm CaII} \approx 5 \times 10^{18}$ cm^{-2}. They show that, assuming the CSM is of solar abundance and in a spherical shell of $R \approx 10^{16}$ cm, this implies a total CSM mass of $M_{\rm csm} \approx 5.36$ M$_\odot$. As this is much larger than expected for a recurrent nova progenitor system, D12 infer that the CSM must be distributed in a ring geometry instead of a spherically symmetric shell. Since this is a significant conclusion regarding the progenitor system, in Graham et al. (2017a) we reassess this measure of column density from the Ca II absorption feature in the pre-maximum spectra after reconsidering the appropriate regime on the curve-of-growth and incorporating turbulence effects, with additional analysis of the Na I D lines and the optical depth of the CSM . We find that the column density of Ca II could be as low as $N_{\rm Ca} \approx (1-4) \times 10^{16}$ cm^{-2}, two orders of magnitude lower than estimated in D12. Under the assumption of solar abundance (i.e., that the number ratio of Ca to H is approximately 1 to 5×10^5) this is a total particle column density of $N_{\rm CSM} \approx 5 \times 10^{21}$ cm^{-2}.

In order to translate a column density into a particle density we must first estimate the radial extent of the CSM. The integrated luminosity of broad Hα decreases steeply around 500 days after explosion, indicating the end of interaction (the end of energy deposition) –

i.e., that the shock has swept over the CSM. Using this observation and the inferred impact time of ~ 40 days after explosion, one can estimate the CSM extent from Equation 3.24 to be $\Delta R_{\rm CSM} \approx 4R_{\rm imp}$. This is in agreement with the estimate of Silverman et al. (2013b). We note, however, that it neglects possible re-energization from a collision with the second shell (§3.6). We combine our revised CSM column density and this CSM depth to estimate that the CSM particle density is $n_{\rm csm} = N_{\rm csm}/\Delta R_{\rm csm} \approx (1.3-5) \times 10^5$ cm^{-3}. We consider $N_{\rm csm} \approx 10^{23}$ cm^{-2}, as estimated by D12, to be an upper limit that gives $n_{\rm csm} \lesssim 1.0 \times 10^7$ cm^{-3}.

If we assume a solar abundance (average mass per atomic particle of $\sim 1.3 m_p$) and a spherical shell geometry for the CSM in the PTF11kx system, our revised estimates for the density and radial extent of the material lead to a total mass estimate of $M_{\rm CSM} \approx 0.06 - 0.24$ M$_\odot$. This value is significantly lower than the estimate in D12 but similar to derived estimates of CSM mass for other SNe Ia such as Kepler 1604 (Katsuda et al., 2015) and SN 2003du (Gerardy et al., 2004). It is much larger than the 2×10^{-6} M$_\odot$ estimated by mass build-up models (Moore and Bildsten, 2012), and may indicate a phase of rapid mass loss by the companion in the years before the white dwarf explodes.

4.3 Continued Ionization of the CSM from the Reverse Shock

Though after about 500 days the forward shock has passed over the CSM and thus no longer powers broad Hα, the reverse shock lives on and continues to produce ionizing photons that propagate into the cooled, fast CSM. Thus, some of the observed broad Hα luminosity may be the result of continued photoionization and photo-recombination powered by the reverse shock.

To investigate this, I evolve a model like those described in §3.1 with an impact time of 50 days after explosion, CSM density 10^{-18} g cm^{-3} intermediate between our estimate and that of D12, and CSM depth $\Delta R = 4R_{\rm imp}$. This CSM has a mass of 0.2 $M_\odot$, nearly the same as the outer ejecta, so the reverse shock enters the inner ejecta at about the time the forward shock overtakes the edge of the CSM. For these CSM properties the maximum ejecta speed is $20,000$ km s^{-1}. To calculate the free-free luminosity from the reverse shock I assume $Z = 7$ (to mimic half carbon, half oxygen), that at all times that the shocked ejecta are fully ionized and free of hydrogen, and that the electrons are thermally distributed.

To estimate the plausibility that the reverse shock powers Hα through photoionization equilibrium, here I naïvely estimate that one Hα photon is produced per ionizing photon absorbed. Then the broad Hα luminosity is related to the ionizing photon production rate, $\dot{Q}_{\rm ion}$, simply by

$$L_{\rm H\alpha} = E_{\rm H\alpha} \dot{Q}_{\rm ion} \ , \tag{4.1}$$

where $E_{\rm H\alpha}$ is the energy of an Hα photon. The ionizing photon production rate is defined

by

$$\dot{Q}_{\rm ion} = \int_{{\rm Ry}/h}^{\nu_{\rm abs}} \frac{L_{\nu,{\rm ff}}\left(\nu\right)}{h\nu} d\nu \ , \tag{4.2}$$

where, $\nu_{\rm abs}$ is the frequency at which the bound-free optical depth of the CSM is 2/3 (single scatter) and depends on the structure of the CSM. In fact, $\dot{Q}_{\rm ion}$ is rather insensitive to $\nu_{\rm abs}$ because the frequency dependence of free-free emission is $L_{\nu,{\rm ff}} \propto e^{-h\nu/kT}$ (h is Planck's constant, k the Boltzmann constant, and T the gas temperature) and so is nearly constant up to $h\nu \approx kT$, which in our simulations is $kT \gtrsim 10$ keV. We note that in our simulations $\nu_{\rm abs} \lesssim 10$ keV even at early times, so the gamma rays being produced in the supernova core easily free-stream through the CSM and do not contribute to the Hα luminosity. The free-free luminosity is calculated with the optically thin method described in §2.5.

We find that the late-time x-ray (*Swift* 0.2-10 keV band) luminosity is similar to that of the observed Hα luminosity, with a slower evolution similar to the forward-shock dominated SN 1988Z at this epoch. The UV luminosity absorbed by the CSM is also similar to the observed Hα luminosity; but this does not translate to a matching Hα luminosity.

As an upper limit to the possible Hα luminosity that can be generated, we can simply calculate $\dot{Q}_{\rm ion}$ from each mass resolution element in the shocked ejecta and convert it to $L_{\rm H\alpha}$. In Figure 4.1, this is represented by the green and orange curves. Because we do not include cooling in our hydrodynamic evolution, for reference we show the budget from just the inner 30% of the shocked ejecta as well as from the entirety of the shocked ejecta. To actually estimate the reprocessing from the shocked CSM in our simulations requires estimating the absorbed fraction of these photons. To do this we first estimate the frequency at which the bound-free optical depth is 2/3, using the hydrogenic approximation for the bound-free cross section:

$$\sigma_{\rm bf} = \frac{\pi q_e^2}{m_e c \nu_{\rm Ry}} \left(\nu/\nu_{\rm Ry}\right)^{-3} \ , \tag{4.3}$$

where ν is the photon frequency, $\nu_{\rm Ry} = 13.6$ eV$/h$, and other constants as defined in Table 2.1. We then calculate the ionizing photon production rate up to this frequency and compare it to the hydrogen photorecombination rate of the whole CSM (analogous to a Stromgren sphere calculation for ionization state) and take the minimum of the two values to be the number of recombinations occurring per second. This is shown as the bold black curve in Figure 4.1 (ionizing photons from all of the shocked ejecta), and it falls short of the available budget once the CSM begins to freely expand (due to the decline in optical depth). The luminosity decline is more rapid than is observed for PTF11kx, like reverse-shock-dominated SN 1993S.

4.4 Conclusions for the CSM of PTF11kx

The CSM parameters suggested by observations of PTF11kx are a shell of density $\rho_{\rm csm} \approx 10^{-18}$ g cm^{-3}, $t_{\rm imp} \approx 50$ days, and $f_R \approx 4$. Though interaction with the main mass of CSM ended around 500 days, the broad Hα line is still visible at 3.5 years post explosion and at

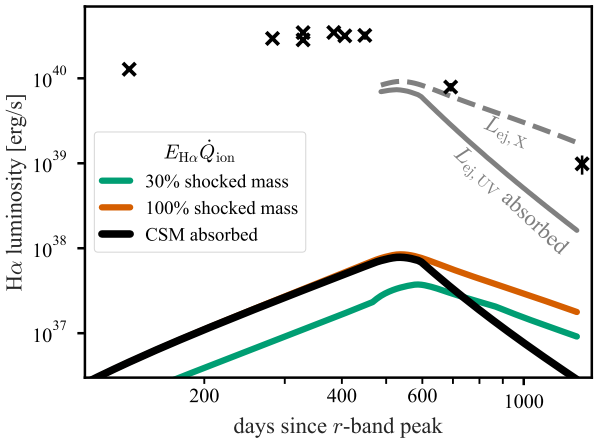

Figure 4.1: Predicted Hα luminosity in a scenario where SN ejecta impact CSM with density 10^{-18} g cm^{-3} and fractional width $\Delta R = 4R$, 50 days after explosion, as described in § 4.2 compared to the observed Hα luminosity (black crosses). The grey curves show the high-energy radiation from the reverse shock, which dominates after the end of interaction (only shown after end of interaction): the 0.2-10 keV luminosity (dashed grey) and the luminosity of extreme-UV photons absorbed by the expanding CSM (solid grey). If the CSM were not expanding, the UV would match the x-ray luminosity at all times. The black curve shows the actual reprocessing in this model, which drops sharply after the CSM enters a state of free expansion due to declining optical depth to ionizing photons. For reference we show Hα luminosity upper limits: reprocessing all photons from the shocked ejecta (orange), as well just photons produced in the inner 30% of shocked mass (green) to account for the lack of cooling in our model. Reprocessing of UV photons from the shocked ejecta cannot account for the observed Hα luminosity.

a higher luminosity than would have been extrapolated from prior observations. I simulated interaction with the CSM to determine whether ionizing radiation from the reverse shock could be powering this emission. The total mass of the CSM is $\approx 0.2\ M_\odot$, more than the mass in the outer ejecta; therefore the reverse shock will enter the inner CSM before the end of interaction and the calculation of x-ray emission requires numerical modeling.

My analysis shows that the reverse shock does produce approximately the Hα luminosity in soft x-ray emission. Due to the expansion of the CSM after the shock sweeps over it, in my models the optical depth of the CSM to ionizing radiation drops steeply after interaction. The observed decline of the Hα luminosity is between the decline rates of the unabsorbed x-ray and absorbed UV luminosities from my model.

For SNe II, Chevalier and Fransson (1994) calculate that the Hα emission ought to be about half of the x-ray emission from interaction. While this is approximately true comparing the x-ray of my model to the observed Hα luminosity, if each ionizing photon produces one Hα photon then my model necessarily cannot reproduce the observed Hα luminosity. From my

simple treatment of the line luminosity, the reverse shock *cannot* power the Hα luminosity. However, if somehow the reprocessing of the UV and higher-energy photons is more efficient, it may be possible. This highlights the need for a more sophisticated simultaneous treatment of x-ray and optical radiation processes for shocked gas.

Chapter 5

Don't Blink: The Unseen Interaction of the Type Ia;n SN 2015cp

5.1 The Near-UV Discovery of Interaction in SN 2015cp

To measure how frequently 91T-like SNe Ia interact at late times, the *Hubble Space Telescope* (HST) Snapshot survey GO-14779 (PI M. Graham) surveyed seventy-one (71) one- to three-year-old SNe (nearly all SNe Ia with some SNe IIn) throughout the year 2017 in the near-ultraviolet (NUV). The target list of eighty (80) objects prioritized 91T-like SNe and those with blueshifted Na I D absorption. This program discovered delayed interaction in SN 2015cp (a.k.a. PS15dpq, PTF15fel), confirmed by the presence of broad Hα emission in a follow-up optical spectrum. From the photometric fit, SN 2015cp exploded on November 11, 2015 (day of first light) and thus the NUV detection was on day 676. In this chapter, all times are relative to the day of explosion unless stated otherwise. The only pre-interaction optical spectrum available for this event was its 60 day classification spectrum, which shows no signs of CSM. Details of the full survey and the NUV/optical observations of SN 2015cp will be presented by Graham et al. (2018).

This chapter is about the radio and x-ray follow-up observations of SN 2015cp. I analyzed the radio data using the models of Harris et al. (2016) as described in Chapters 2 and 3. This analysis translates the radio upper limits into limits on the total mass of CSM and other properties. In §5.2 we present the observations of SN 2015cp taken ≈ 80 days after the NUV detection with the Arcminute Microkelvin Imager (AMI), Very Large Array (VLA), and *Swift* observatories. We analyze the radio non-detections §5.3 and limit the CSM mass to be, at most, similar to that of PTF11kx ($< 2\ M_{\odot}$). In §5.4 we summarize our results, contextualize the constraints with SN Ia progenitor theory, and outline how to systematically find and characterize SNe Ia;n.

The work in this chapter borrows extensively from a manuscript currently being prepared for submission, Harris et al. (2018). I would like to outline the contributions of the co-authors

of that manuscript to this chapter. Assaf Horesh and Joe Bright led the radio observations and reduced those data; Peter Nugent and I obtained the x-ray observations, which were reduced by Nathan Butler; Melissa Graham, Peter Nugent, Kate Maguire, Mark Sullivan, and Stefano Valenti led the efforts to obtain and reduce the NUV and optical data used in the manuscript; Graham and Nugent worked closely with me in the initial preparation of the manuscript; and the rest of the NUV HST team (Alex Filippenko, Ori Fox, Ariel Goobar, Patrick Kelly, and Ken Shen) are also collaborators on the manuscript and either have or will contribute comments to various versions of the manuscript.

5.2 Radio and X-ray Observations

My radio and x-ray modeling of the nearest analog to SN 2015cp, PTF11kx, indicated that a PTF11kx-like event at the distance of PTF15fel (≈ 170 Mpc) would be visible in the radio and x-rays, though fading. We therefore pursued observations with AMI, VLA, and *Swift*. The model and resulting non-detections are shown in Figure 5.1.

SN 2015cp was observed by AMI (Zwart et al., 2008; Hickish et al., 2018) on 04-Dec-2017/19:30:17.7 (MJD 58091.82) with a total integration time of 4.96 hours. The AMI-LA is equipped with a digital correlator (Hickish et al., 2018) with a central frequency of 15.5 GHz and a 5 GHz bandwidth spread across 4096 channels. The data were calibrated using the custom reduction pipeline REDUCE_DC (see, e.g., Perrott et al., 2013), which also performs flagging for antenna shadowing, instrumentation errors, and radio frequency interference (RFI). At this stage the data were binned into 8 frequency channels and imported into the Common Astronomy Software Applications (CASA) package, where additional RFI flagging and then cleaning were performed to produce an image, which contained a single unresolved source. Fitting this source with the CASA task IMFIT gives its location as RA: 03:09:13.18(2), Dec: +027:34:16.8(5) with a flux density of 1.24 ± 0.08 mJy. Given that this position is ~ 3 arcminutes from the phase center and the synthesized beam for this observation has major and minor axes of ~ 40 and 30 arcseconds (respectively), we conclude that this is not SN 2015cp. This conclusion is further supported by the position being consistent with a known source in the NVSS archive (Condon et al., 1998). The root-mean-square (RMS) at the phase center of the AMI-LA image is $\sim 30\,\mu$Jy and so we set a 3σ upper limit on the 15.5 GHz radio emission from SN 2015cp of $\sim 90\,\mu$Jy.

On UT 24-Dec-2017, we observed SN 2015cp with the Jansky Very Large Array (VLA; under program 17B-434, PI Horesh) at a central frequency of 6 GHz (C-band) and undertaken in the B configuration. We used J0329+2756 and 3C138 for phase and flux calibration, respectively, and reduced the data using standard CASA calibration and imaging routines. The observation resulted in a null-detection with a 5.8 μJy RMS, corresponding to a 3σ upper limit of 17.4 μJy.

From UT 8-Dec-2017 through 9-Dec-2017, we observed SN 2015cp with the UVOT and XRT instruments on board *Swift*. No source is detected in a 4.9 ks UVOT exposure using the UVW1 filter, nor are any counts detected near the source position in the 6.1 ks (livetime, 0.5-

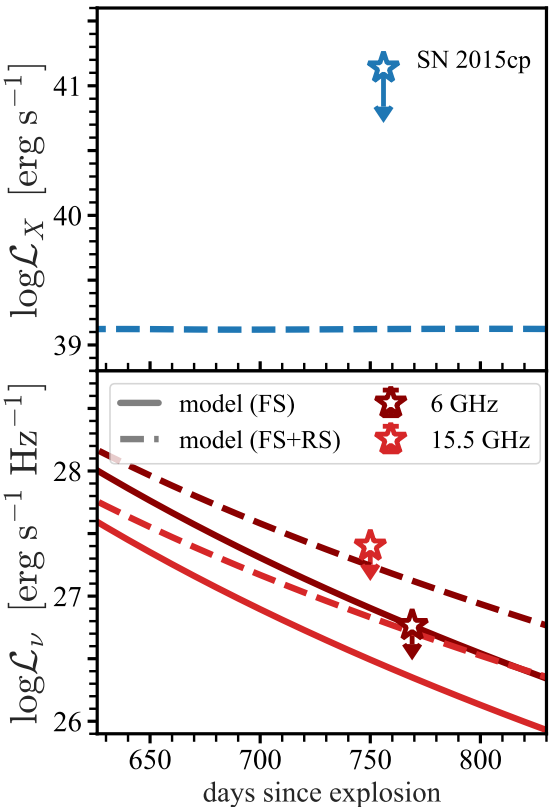

Figure 5.1: Observations of SN 2015cp (stars) in x-ray (top panel; 0.5-8 keV *Swift*) and radio (bottom panel; AMI at 15.5 GHz, bright red; VLA at 6 GHz, dark red) compared to a model with $\rho_{\rm csm} = 10^{-19}$ g cm^{-3}, $f_R = 4$, $t_{\rm imp} = 50$ days created for PTF11kx both including (solid) and excluding (dashed) contribution from the reverse shock. Models like this one, which are just under the detection threshold, represent the maximum-mass CSM that would be undetected for its particular value of $t_{\rm imp}$ and f_R.

8 keV) XRT exposure. Using the *Swift*UVOT zeropoints[1], we derive a 3σ limiting magnitude of 23 in the AB system. Assuming only absorption by the Galaxy in the direction of the SN (with $N_H = 1.1 \times 10^{21}$ cm^{-2}; Kalberla et al., 2005) and assuming a spectrum with photon index $\Gamma = 2$, we derive a 3σ limiting X-ray flux of 4.1×10^{-14} erg cm^{-2} s^{-1} (0.5-8 keV).

5.2.1 Constraining the Duration of Interaction with Optical and NUV Data

In §5.3.2 we will see that constraining the time interaction ends (t_p) or time of impact ($t_{\rm imp}$) increases the utility of the radio data. To this end, we compare SN 2015cp to its nearest

[1]https://swift.gsfc.nasa.gov/analysis/uvot_digest/zeropts.html

Table 5.1: SN 2015cp Radio and X-ray Observations

UT Date	Instrument	Frequency	3σ upper limit
2017-12-04	AMI-LA	15.5 GHz	90 μJy
2017-12-24	VLA	6 GHz	17.4 μJy
2017-12-08	Swift-UVOT	4.8 eV	2.3 μJy
2017-12-08	Swift-XRT	1 keV	6.1 nJy

analog PTF11kx using the metric that indicated the interaction history of that object: the integrated luminosity of the broad Hα line ($\mathcal{L}_{\rm H\alpha}$) from Silverman et al. (2013b). In Figure 5.2 we show $\mathcal{L}_{\rm H\alpha}$ for PTF11kx and SN 2015cp. For SN 2015cp we also include the line luminosity of the Ca II near-infrared triplet, which matches Hα at all times, and the NUV detection and upper limit, which may have been Mg II (Graham et al., 2018) and is consistent with the decline rate of the optical lines. No broad SN features are seen in the spectrum; all of these lines are powered by interaction.

The two SNe have very different coverage: PTF11kx has more regular sampling throughout its interaction, but SN 2015cp has excellent sampling of the $\mathcal{L}_{\rm H\alpha}$ decline. For PTF11kx, we know $\mathcal{L}_{\rm H\alpha}$ increased until 285 days, plateaued for the next 160 days, and started to decline sometime between 450 and 695 days. The decline indicated that the reservoir of cooling gas was depleted, constraining 450 days $\leq t_p \leq$ 690 days and leaving the $\mathcal{L}_{\rm H\alpha}$ decline rate highly uncertain. In contrast, SN 2015cp has no spectra between its classification spectrum ($\approx$ 60 days) and the X-Shooter spectrum (690 days), so its impact time and peak times are poorly constrained; but its decline is well observed by the follow-up campaign. Over the observed one hundred days, SN 2015cp has $\mathcal{L}_{\rm H\alpha} \propto t^{-8.6}$. The fortuitous observation of both SNe with optical spectra at 690 days allows us at least to say that these SNe are not twins: SN 2015cp is an order of magnitude fainter in Hα than PTF11kx at this age. If PTF11kx followed the same decline as SN 2015cp then its interaction ended at 588 days and $f_{R,\rm 11kx} = 5.9$ (using $t_{\rm imp,11kx} = 50$ days).

If we knew the peak Hα luminosity reached by SN 2015cp, we would be able to constrain the time interaction ended. Since we do not have these data, in this work we instead consider two cases representing different conservative assumptions, illustrated in Figure 5.2:

- Case 1 assumes SN 2015cp was brightest in Hα at discovery, i.e., $t_p = 676$ days. This would not be as serendipitous as it may, at first, seem: detection favors the bright, and the Hα luminosity was likely highest just before interaction ended – when the reservoir of cooling shocked hydrogen is greatest.

- Case 2 assumes the observed $\mathcal{L}_{\rm H\alpha}$ decline rate is constant *and* that SN 2015cp had the same maximum $\mathcal{L}_{\rm H\alpha}$ as PTF11kx, resulting in $t_p = 505$ days. Furthermore, if PTF11kx and SN 2015cp had the same CSM density then, like PTF11kx, SN 2015cp would have needed 282 days to reach the plateau luminosity, so for this case $t_{\rm imp} \leq 223$ days.

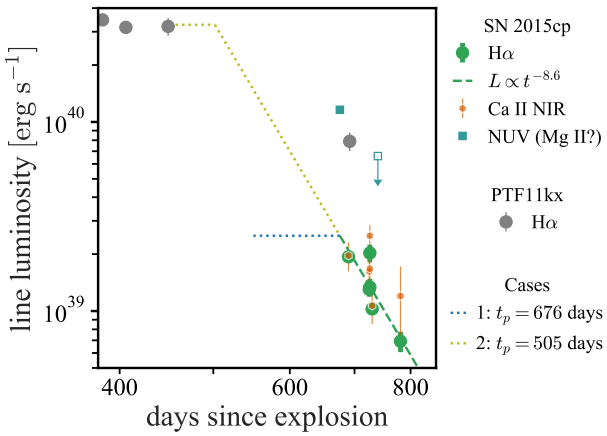

Figure 5.2: We use the evolution of the broad Hα emission line luminosity to constrain the duration of interaction for SN 2015cp (green circles), as was done for PTF11kx (Silverman et al., 2013b, grey circles). Monthly spectra reveal the steep decline of this emission that indicates interaction was over by the NUV detection at 676 days. Also shown are the integrated Ca II NIR emission (orange hexagons) and the NUV data (teal squares) that may have been line emission from Mg II. The decline rates of both are consistent with the decline rate of Hα, which follows $\mathcal{L} \propto t^{-8.6}$ (green dashed line). At the same age (690 days), SN 2015cp is an order of magnitude dimmer than PTF11kx. Based on this difference, we consider two scenarios (dotted): Case 1 (blue), that we discovered SN 2015cp just as interaction ended ($t_p = 676$ days), and this event is intrinsically fainter in Hα than PTF11kx; and Case 2 (yellow), that SN 2015cp had the same Hα luminosity as PTF11kx and its interaction ended at $t_p = 505$ days.

Case 1 is our favored scenario because it has fewer assumptions, since Case 2 relies on both extrapolation and a comparison to PTF11kx that may not be appropriate. If the extrapolation is appropriate, however, then CSM limits obtained in Cases 1 and 2 bound the limits that would be obtained from assuming any $\mathcal{L}_{\mathrm{H}\alpha}$ peak between 3×10^{39} and 3×10^{40} erg s^{-1}.

5.3 Constraints on the CSM

In this section we describe the constant-density, finite-extent CSM radio light curve models of Chapter 3 and use them to limit the CSM properties. The direct observational considerations in this analysis are: (1) impact occurred at > 60 days, (2) interaction ended by the time of the NUV detection at 676 days, (3) our *earliest* radio limit is at 750 days, and (4) our *deepest* radio limit is at 769 days.

5.3.1 Model Summary

The radio light curves used here are the same as those in Chapter 3, but we will recall the equations relevant to this work in particular. The inner CSM radius ($R_{\rm in}$), impact time ($t_{\rm imp}$), and CSM density ($\rho_{\rm csm}$) are related through the requirement that the ejecta and CSM be similar density, and so (Equation 3.4)

$$R_{\rm in} \propto t_{\rm imp}^{0.7}\ \rho_{\rm csm}^{-0.1} \quad . \tag{5.1}$$

Because the shells have constant density, the mass of a shell is determined by $R_{\rm in}$, $\rho_{\rm csm}$, and the CSM fractional width ($f_R \equiv \Delta R/R_{\rm in}$) simply by

$$M_{\rm csm} \propto \rho_{\rm csm} R_{\rm in}^3 \left[(1+f_R)^3 - 1\right] \quad . \tag{5.2}$$

Given in Equation 3.24, the time that interaction ends (the time of the radio peak luminosity, t_p) is related to $t_{\rm imp}$ and f_R by

$$t_p \propto t_{\rm imp}\ (1+f_R)^{1.28} \tag{5.3}$$

and the optically thin peak specific luminosity ($\mathcal{L}_{\nu,\rm p}$) is related to $\rho_{\rm csm}$, $R_{\rm in}$, f_R, and frequency ν in Equation 3.28,

$$\mathcal{L}_{\nu,\rm p} \propto \nu^{-1}\ \rho_{\rm csm}^{8/7}\ R_{\rm in}^{3/7}\ \left[1-(1+f_R)^{-9/7}\right] \tag{5.4}$$

where the exponent of 9/7 is an approximation of the fit value 1.28 to elucidate the relative importance of each factor. As in Chapter 3, we use $\epsilon_B = 0.1$.

Because our radio observations are after the light curve peak, we are using the parameterization for the light curve post-peak decline including only the shocked CSM (Equation 3.29, solid line in Figure 5.1), which describes the decline from $\mathcal{L}_{\nu,\rm p}$ to $10^{-3}\mathcal{L}_{\nu,\rm p}$ using only $t_{\rm imp}$, f_R, and $\mathcal{L}_{\nu,\rm p}$. Thus we cannot comment on early impacts with thin shells because they would have declined below $10^{-3}\mathcal{L}_{\nu,\rm p}$ by the time of observation. In using these models we are assuming the synchrotron emission is optically thin at the time of observation, which is likely accurate considering the rapid rarefaction of the CSM as soon as it has been swept over.

5.3.2 Mass Limits from Radio Data

Using these parameterized light curves described in the previous section we can determine the maximum CSM mass allowed by our VLA and AMI non-detections, with particular consideration given to the two cases forwarded in §5.2. The analysis procedure is the same that we employed in §3.5.

The methodology is straightforward: We create a grid of models varying $t_{\rm imp}$ and f_R, determine for each the maximum $\mathcal{L}_{\nu,\rm p}$ allowed by the AMI and VLA limits (separately), and translate this into a mass limit. From observations, $t_{\rm imp} \geq 60$ days and $t_p \leq 676$ days, and

we assume $f_R \geq 0.1$. These criteria set our explored parameter space to $t_{\rm imp} \in [60, 609]$ days and $f_R \in [0.1, 5.72]$. Cases 1 and 2 fix t_p to a particular value and represent a specific contour in $t_{\rm imp}$-f_R space (and in Case 2, $t_{\rm imp} \leq 223$ days, i.e., $f_R \geq 0.9$; Equation 5.3).

The mass limits resulting from this analysis are shown in Figure 5.3. It is important to acknowledge that the mass constraints from the VLA and the AMI data are nearly the same, highlighting the power of rapid follow-up observations for these steeply declining light curves. The VLA limit is eleven times deeper than that of AMI, after accounting for the spectral energy distribution (SED) and the observed frequency, but the AMI limit is as effective just by virtue of occurring three weeks earlier. For reference, we also present how the maximum allowed mass would decrease if the VLA non-detection were four times deeper, to simulate a longer exposure time or closer object and to indicate that these are upper limits.

Given an f_R, there is a maximum possible impact time that satisfies the requirement $t_p < 676$ days, setting the latest $t_{\rm imp}$ for each f_R curve. The thickest possible shell has only one valid impact time, while thinner shells span more of the domain. For curves thinner than $f_R \approx 1$ the shaded regions also appear to have an earliest possible impact time, but this is simply due to the limitations of the parameterized light curves (§5.3.1). The steep slope of each f_R curve reflects the steep decline of the light curves.

The degeneracy between f_R and $t_{\rm imp}$ as well as the sensitive dependence of the mass limit on $t_{\rm imp}$ are obvious in this figure and motivated the search for additional constraints on the duration of interaction described in §5.2.1. We consider two cases: Case 1, the radio light curves peak at $t_p = 676$ days; and Case 2, $t_p = 505$ days. A fixed t_p gives a relation between f_R and $t_{\rm imp}$ rather than a constraint on either parameter alone (Equation 5.3); therefore these cases create curves spanning all values of $t_{\rm imp}$ and f_R in Figure 5.3. Knowing t_p actually constrains the CSM mass very well almost independent of the inaccuracy in $t_{\rm imp}$ and f_R. For this reason, we identify it as the key parameter to constrain in future efforts to characterize SNe Ia;n.

The VLA non-detection constrains the CSM mass to $M_{\rm csm} < 0.5\ M_\odot$ for Case 1 and $M_{\rm csm} < 2\ M_\odot$ for Case 2. Particularly in Case 1, these limits are similar to the mass measured for PTF11kx (Graham et al., 2017a), as shown. We show both the reported $M_{\rm csm,11kx} = 0.06\ M_\odot$ as well as a higher estimate of $M_{\rm csm,11kx} = 0.42\ M_\odot$ that results from assuming the four-times higher column density reported by the authors as well as the result from this work that the CSM may have been thicker than previously assumed (§5.2.1).

5.3.3 The Constraining Power of Pre-Impact Spectra

For PTF11kx, the saturated narrow absorption lines in the pre-impact optical spectra alerted observers to the unique nature of the event. Borkowski et al. (2009) identify the narrow Na D features as a good metric for CSM shell properties when considering shells at $> 10^{17}$ cm, and we expect the same is true for nearer cases. So in this section, we translate the VLA upper limit into limits on quantities other than the total CSM mass that can be cross-validated by panchromatic datasets. We look at the CSM column density $N_{\rm csm}$ and its constituent

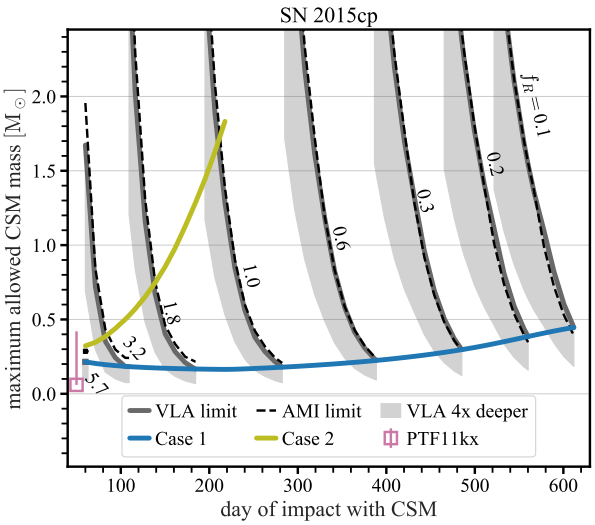

Figure 5.3: Upper limits on the CSM mass of SN 2015cp as a function of the impact time ($t_{\rm imp}$) and shell width (f_R) for select f_R, using radio models of interaction with a finite-extent, constant-density shell. Constraints from the 769 day VLA 6 GHz non-detection (grey line) and the 750 day AMI 15.5 GHz non-detection (dashed black line) are similar, highlighting the power of obtaining observations as quickly as possible. For reference and intuition, we illustrate how the constraints would change if the VLA non-detection were four times deeper (grey shading). Cases 1 (blue line) and 2 (yellow line) constrain the time of radio peak to 676 and 505 days, respectively. The VLA limit constrains the CSM mass to be $M_{\rm csm} < 0.5\ M_\odot$ for Case 1 and $M_{\rm csm} < 2\ M_\odot$ for Case 2 *despite large uncertainties in the CSM location and extent*, showing the importance of constraining t_p. For comparison we show the mass limit for PTF11kx (open square).

factors f_R, $R_{\rm in}$, and $\rho_{\rm csm}$:

$$N_{\rm csm} = n_{\rm csm} f_R R_{\rm in} = \rho_{\rm csm} f_R R_{\rm in}/(\mu m_p) \quad . \tag{5.5}$$

This analysis is relevant for future observations rather than SN 2015cp itself, whose only pre-impact spectrum is too late to have seen such features.

In Figure 5.4 we show these constraints for Cases 1 and 2 again as a function of $t_{\rm imp}$. As in Figure 5.3, shaded bands represent a simulated VLA non-detection up to four times deeper than the actual non-detection. We also show the value of each parameter for PTF11kx as derived in Graham et al. (2017a), noting both the higher and lower reported values for the column density. The equations provided in §5.3.1 are a helpful reference when interpreting the behavior of the curves in Panels *a-c*.

Panel *a* simply illustrates the relationship between f_R and $t_{\rm imp}$ for a fixed t_p and is independent of the VLA limit. Earlier $t_{\rm imp}$ require wider shells to peak at a given time.

Panel *b* shows our upper limit on CSM density. The Case 2 limit is higher (weaker) than the Case 1 limit because the light curve has had longer to decline, so higher peak luminosities

and thus higher densities are permissible. Later impact times allow higher $\rho_{\rm csm}$ (for a given t_p) because thinner shells have a lower peak luminosity and faster decline rate than thicker shells. For PTF11kx this value is derived using measurements of f_R, $t_{\rm imp}$, and $N_{\rm csm}$.

In Panel *c* we plot the limit on $R_{\rm in}$, which is actually a lower limit. While generally the behavior of this curve is intuitive (one would expect a later impact time to imply a more distant shell), the weak dependence of $R_{\rm in}$ on $\rho_{\rm csm}$ actually requires that higher-density shells be nearer to the SN for interaction to begin at a given time resulting in a maximum $R_{\rm in}$. The dependence on $\rho_{\rm csm}$ is also why a deeper VLA limit (shaded band), which would constrain the CSM to lower densities, would imply a higher $R_{\rm in}$. The value for PTF11kx comes from $t_{\rm imp}$ and assuming a maximum ejecta speed, but is consistent with the HNK16 value given its $t_{\rm imp}$ and $\rho_{\rm csm}$.

Finally, in Panel *d* we use Equation 5.5 to translate our radio non-detections into an upper limit on $N_{\rm csm}$. As with the mass constraint previously, fixing t_p results in limits on $N_{\rm csm}$ that are almost independent of $t_{\rm imp}$, particularly for Case 1.

While $N_{\rm csm}$ is not single-valued, we see that a reliable measurement of $N_{\rm csm}$ from a spectrum near maximum *B*-band brightness could constrain t_p by making Case 1 (i.e. late values of t_p) less likely. The Ca K absorption line in PTF11kx that was used to measure $N_{\rm csm}$ was strong up to at least 20 days after maximum light, so this metric does not necessarily require very early-time spectra (but does benefit from high-resolution spectra).

5.4 Summary and Guidelines for Future Observations of SNe Ia;n

SN 2015cp is the third case of an SN Ia interacting with CSM located $\sim 10^{16}$ cm from the progenitor system, what we call an SN Ia;n. To conclude this chapter, I will summarize our radio and x-ray non-detections and the constraints on the circumstellar environment of SN 2015cp obtained by applying my thin shell interaction toolset. I will then put these limits in context of SN Ia progenitor theory and other known interacting SNe Ia. Finally, I will highlight the need for a systematic search for SNe Ia;n and make suggestions based on the lessons learned from our analysis of both PTF11kx and SN 2015cp.

At 167 Mpc, SN 2015cp was a good candidate for radio and x-ray follow-up observations once interaction was discovered. Models of its nearest analog PTF11kx suggested SN 2015cp could still be visible even if (like PTF11kx) interaction had ceased – that interaction had ended for SN 2015cp was unknown at the time of the observations. Therefore we observed this target with the VLA, AMI, and *Swift* observatories. All observations resulted in non-detections.

Nevertheless, the radio upper limits can be interpreted in the framework of Harris et al. (2016) to give limits on the CSM properties. We assess two scenarios: Case 1, in which the radio light curve peaked at the time of near-UV discovery (676 days); and Case 2 in which the radio light curve peaked at 505 days, under the assumption that the Hα luminosity of

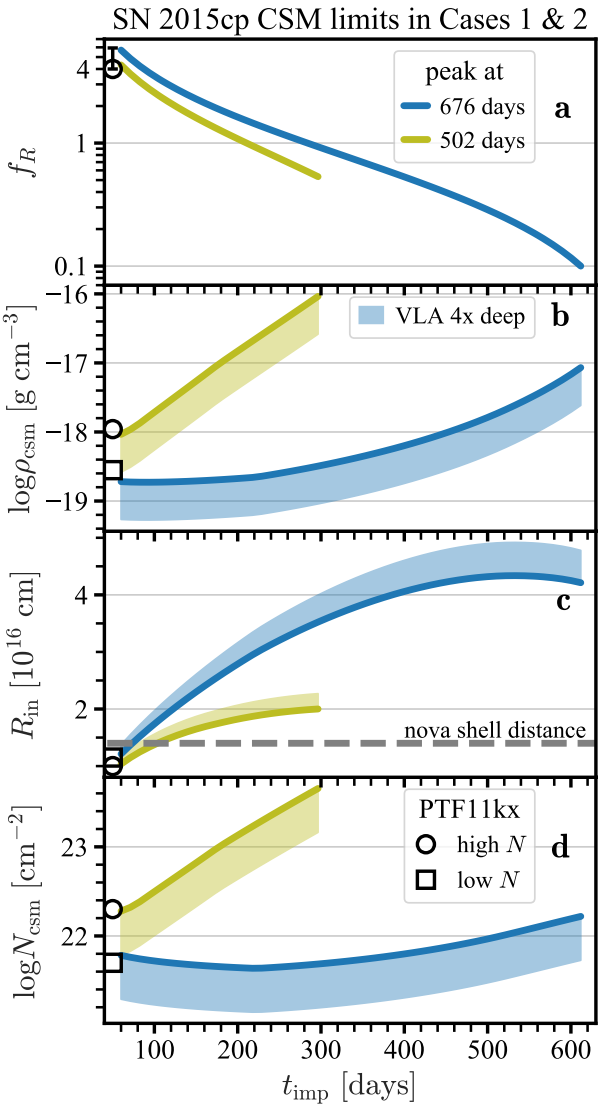

Figure 5.4: Constraints on CSM properties for Case 1 (blue; radio peak at 676 days) and Case 2 (yellow; peak at 505 days), with a comparison to PTF11kx (open markers). Shaded bands represent the analysis with a non-detection up to four-times deeper to illustrate limits. Legends apply to all panels. The panels are (a) fractional width, (b) mass density, (c) inner radius, and (d) column density. Our limits on the inner radius are similar to the expected location of nova shells. Panel *d* shows that a measurement of column density from an optical spectrum near the SN *B*-band maximum could be leveraged: if the column density were measured to be 3×10^{22} cm^{-2}, it would rule out Case 1, though Case 2 would be allowed – recalling that these lines are upper limits as allowed by the VLA non-detection.

SN 2015cp was the same as that of PTF11kx. Without these assumptions there is too large an uncertainty in $t_{\rm imp} - f_R$ space to draw conclusions, as the extent of the CSM is a key parameter. We find that the CSM has a mass $M_{\rm csm} < 0.5\ M_\odot$ for Case 1. Case 2 is less constraining because it implies our observations occur longer after peak radio brightness than in Case 1; in Case 2, $M_{\rm csm} < 2\ M_\odot$. Figure 5.5 summarizes how the various observations of SN 2015cp have been employed to constrain the CSM properties.

Our mass limits are near to the inferred CSM mass of PTF11kx, but far higher than the estimated mass from a single nova shell eruption which for the symbiotic recurrent nova RS Ophiuchi was observed to be $\sim 10^{-6}\ M_\odot$ (O'Brien et al., 1992).

In line with SNe Ia-CSM, SNe Ia;n are associated with 91T-like SNe Ia, which may represent the single-degenerate progenitor channel. A possible scenario that links non-interacting 91T-like SNe Ia, SNe Ia;n, and SNe Ia-CSM is that there is a relatively brief period (perhaps 10^5 years) of mass transfer in which relatively continuous heavy mass loss is punctuated by eruptive episodes. This kind of scenario is analogous to symbiotic recurrent novae, and in those systems Moore and Bildsten (2012) show that the outbursts quickly sweep up the mass from the steady phase, slow down, and pile up at $R \sim 10^{16}$ cm. In this picture, SNe Ia-CSM occur just before or after an outburst at which time CSM is still near the stellar surface, while SNe Ia;n occur months to years after an outburst when an evacuated cavity still exists. If the SN Ia does not occur during the phase of mass transfer with heavy losses, but instead occurs $\gtrsim 10^6$ years after, the CSM shell will have mixed into the ISM and we will see a non-interacting 91T-like SN Ia. Alternatively, some authors have also suggested that the existence of diverse interaction timescales is a result of a CO WD merging with the core of a post-AGB star (e.g., Soker, 2013).

It is difficult to explore either of these hypotheses with the current data on SNe Ia;n. SN 2002ic lacks early-time spectra, PTF11kx lacks radio or x-ray observations owing to its distance, and SN 2015cp has poor early-time and near-maximum coverage. Therefore, determining the origin of the CSM in SNe Ia;n and possibly thus the progenitors of 91T-like SNe Ia relies partially on increasing our sample of SNe Ia;n with a systematic observation strategy.

From our analyses of PTF11kx and now SN 2015cp, some guidelines emerge. The first suggestion is to ensure that nearby 91T-like SNe Ia are monitored over a years-long baseline. Photometrically this is possible with the Zwicky Transient Facility survey (and, in the future, the Large Synoptic Space Telescope) because Hα holds the R-band magnitude constant months after SN peak (Wood-Vasey et al., 2004; Dilday et al., 2012). This step would discover the onset of interaction, after which regular spectroscopy or imaging with a narrow Hα filter to measure the Hα line strength is strongly encouraged: our analysis shows that the two-year gap in observations of SN 2015cp creates huge uncertainties on t_p which severely limits our ability to use the radio non-detections *a priori*. We also show that in the radio, observations should prioritize being *early* over being *deep*: the AMI non-detection was nearly as constraining as that of the VLA. In the case of a radio detection, of course, the capability of the VLA to provide a spectrum would be crucial and a time series useful. (In this case also an x-ray observation would help constrain the CSM mass; the x-rays would likely be thermal

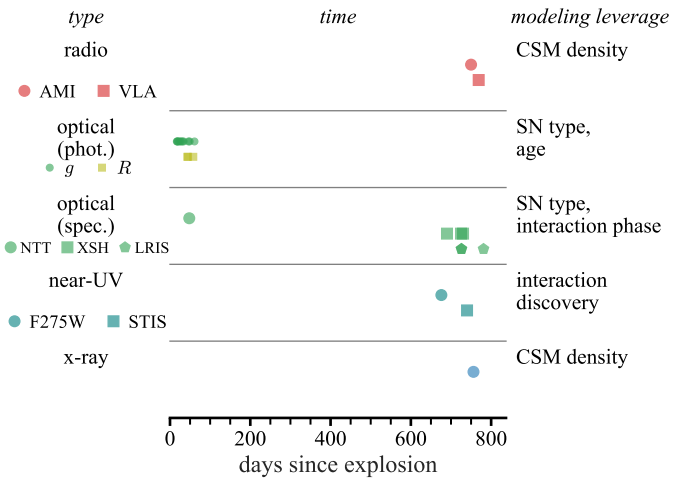

Figure 5.5: A summary of the panchromatic data available for SN 2015cp. The two-year gap between the initial discovery and classification of this supernova and the discovery of its interaction creates large uncertainties in its CSM properties.

free-free and therefore independent of ϵ_B.) Therefore, we suggest that continual monitoring of 91T-like SNe Ia with a plan for rapid combined radio and optical follow-up observations is the path forward for growing our sample of SNe Ia;n and understanding the progenitors of 91T-like SNe Ia.

Chapter 6

Sister from Another Mister: Applying the SN Ia;n Interaction Models to the Type Ib;n SN 2014C

After I had begun modeling interaction with detached CSM, I felt like I was just waiting for the right SN Ia to come along with a radio *detection* that I could use to exercise my models. But as luck would have it, these observations came to me not from an SN Ia but from an SN Ib: SN 2014C.

6.1 The Transformation of SN 2014C

SN Ia researchers do not hold exclusive rights to the headache of mass loss – the process by which massive stars lose their hydrogen and helium envelopes to produce the sequence of SNe II, IIb, Ib, and Ic is still unknown, and it is unclear what the relationship of these classes is to the heavily blanketed SNe IIn (Smith, 2016). Initially it was thought that the envelope stripping and the occurrence of SNe IIn could be neatly described by massive star winds. However, how the strength of the wind depends on the mass and metallicity of the star is unknown, and how it changes in the final centuries of stellar evolution when the core is rapidly changing is likewise unknown. But SN imposters like SN 2009ip seem to suggest that mass loss occurs in eruptive episodes rather than as a steady-state process. Also growing in theoretical importance is the fact that most massive stars are in mass-donating (interacting) binary systems; thus both the stripping of the stellar envelopes and the presence of dense CSM, even the eruptive episodes, may be due to binary processes. As with SNe Ia, constraining the CSM of stripped-envelope SNe to trace the mass-loss history just before explosion is a way to distinguish between these progenitor scenarios.

SN 2014C occurred only 14.7 Mpc away, making it an excellent target for late-time, panchromatic follow-up observations. The metamorphosis of Type Ib SN 2014C into an SN IIn was first described in Milisavljevic et al. (2015, hereafter M15) through optical spectra.

Margutti et al. (2017, hereafter M17) then presented x-ray spectra, a VLA radio spectral energy distribution (SED), the VLA 7.1 GHz light curve, and optical photometry. High-cadence radio observations at 15.7 GHz with AMI (see §5.2) were presented by Anderson et al. (2017, hereafter A17). From M17, I take the date of explosion for SN 2014C to be UT 2018-Dec-30, putting the date of V-band peak at 14 days (M15). As usual, I will report times relative to explosion in this chapter unless otherwise stated.

Now I will summarize the data from these studies relevant to my modeling.

Pre-impact. There is a gap in the M15 spectroscopy between 10 and 127 days, when the object was not observable. The 10-day spectrum is normal for an SN Ib, while the 127-day spectrum is that of an SN IIn; it is also photometrically normal up to 21 days (M17). The 10-day spectrum shows a broad hydrogen component that suggests the envelope of SN 2014C was not *completely* stripped. The authors note that hydrogen can dominate in the spectrum with just 0.03 $M_\odot$ present; therefore I assume there is at least 0.03 $M_\odot$ of hydrogen in the outermost layers of SN 2014C. From a fit to the near-maximum light curve, M17 constrain $M_{\rm ej} = 1.7\ M_\odot$ and $E_{\rm K,ej} = 1.75 \times 10^{51}$ erg. A17 detected radio emission from SN 2014C from $\approx 30 - 200$ days that is consistent with a mini-shell evolution in a wind – the light curve rises until day 80, presumably the effect of decreasing optical depth. Without knowing the absorption mechanism via multi-wavelength data, the authors could not measure the CSM density of this inner region. However, from an x-ray non-detection at about one week after explosion, M17 use a wind model to constrain the density in this "bubble" to have $\dot{M}/v_w < 10^{-5}\ M_\odot\ {\rm yr}^{-1}/(10^3\ {\rm km\ s}^{-1})$.

Onset of interaction. We know that there are signs of interaction by 127 days, from the optical light curve. But this optical transformation does not necessarily imply that by 127 days there was significant energy imparted to the CSM to create a radio signal. In fact between 100 and 200 days, the AMI radio data have quite a lot of scatter and are almost flat; the radio brightness does not begin to rise until 190 days. This is consistent with the picture in which at some point between about 100 and 130 days the outermost ejecta crash into a wall of CSM that they cannot energize until 190 days (when ejecta of approximately the CSM density reaches the wall). The shock traveling through the low-density wind ahead of the ejecta would reflect off the wall of CSM, re-energizing the wind.

Evolution of interaction. The AMI data rise between 190 and 400 days, then begin to decline. A17, stuck in the habit of using a wind model, attributed the rise to a decreasing optical depth. We will see from data provided by A. Kamble and R. Margutti for this work that in fact the 15.7 GHz light curve was well into the optically thin regime by 300 days; the AMI rise actually reflects an increasing energy density in the CSM, as in my prior models. The 7.1 GHz light curve shown in M17 is also rising between 130 and 500 days, though in this case the VLA SED at 400 days shows the flux is absorbed and the rise is due to a decreasing optical depth. M17 show x-ray spectra between 300 and 500 days. By fitting the spectra with an absorbed thermal Bremsstrahlung model, they are able to create an unabsorbed 0.3-100 keV light curve. The integrated, unabsorbed x-ray luminosity is approximately constant over these 200 days.

M17 analyzed the x-ray and radio re-brightening of SN 2014C, as well as its optical trans-

formation, in the framework of an SN interacting with a circumstellar "bubble" surrounded by a dense "wall" as in Chevalier and Liang (1989). In this scenario, a low-density cavity created by a fast stellar (Wolf-Rayet) wind is surrounded by a thin but high-density shell of CSM formed when the fast wind swept up a previously existing slow wind. A major difference between the hypothesized scenario and the observations is that theoretically this wall should be at $\sim 10^{18}$ cm, with interaction occurring after several years. In the initial analysis of SN 2014C (by both M17 and A17), it was overlooked that the self-similar solution of Chevalier (1982a) does not describe the shock propagation into the wall. As noted by Chevalier and Liang (1989), this is because at first the forward shock reflects off of the wall, and then once the shell (wall) can be energized the shock front sweeps over it too quickly to reach the self-similar solution. The analysis of A17 also suffered from the lack of multi-frequency data which caused the authors to assume that the rise to the second peak represented a decreasing optical depth (which is usually the case for radio SNe), whereas in reality the synchrotron emission was optically thin during the rise.

In this chapter I perform the numerical simulations of the hydrodynamics and radiation transport required to constrain the CSE of SN 2014C. For each simulation I simultaneously compute the radio and x-ray emission of the shocked gas due to synchrotron and Bremsstrahlung processes, including absorption. As far as I am aware, this type of modeling has never been done before for an SN X;n. The methods for performing these calculations are described in §2.5. The model space I explore is described in §6.2.

With an appropriate model, I can constrain the density profile of the CSM and thus its total mass. I am also interested in the possibility that the CSM is aspherical. This would be indicated by a one-dimensional model that fits the data well but is simply too luminous, naïvely demanding that the approximation of full coverage by the CSM is incorrect (i.e., the emitting area is not the total surface area of a sphere).

The main conclusions from my modeling of SN 2014C are as follows.

1. Applying the self-similar solution to the transitional interaction phase overestimates the CSM density and extent, and thus the mass.

2. The dense CS shell to which M17 attributed the radio increase was actually responsible only for energizing the ejecta at early times, and the radio peak is from a more extended lower-density region of CSM beyond the wall.

3. Modeling the x-ray and radio light simultaneously is extremely important for checking the two free parameters of the synchrotron radiation calculation.

4. Interaction with $< 0.3\ M_\odot$ of CSM can produce the observed radio and x-ray signal of SN 2014C.

5. My modeling does not show evidence for asymmetric CSM.

6.2 Modeling Methods

Because we are in the low-density regime, the hydrodynamics and radiation calculations are decoupled in our models. This work uses the equations and code described in Chapter 2.

6.2.1 Hydrodynamic Calculations

Here we will review the modeling assumptions specific to modeling of SN 2014C.

We assume that the outer ejecta have a density profile $\rho_{\rm ej} \propto r^{-9}$, normalized by their total mass and kinetic energy $M_{\rm ej} = 1.7\ M_\odot$ and $E_{\rm ej} = 1.8 \times 10^{51}$ erg (respectively) as derived from the optical light curve. The inner zone does not extend to $r = 0$ cm: the simulation only tracks ejecta that will be traversed by the reverse shock by the end of the simulation, typically truncating at a velocity coordinate of about $5,000$ km s^{-1}. The velocity profile of these zones is that of free expansion, and the temperature is assumed to be 10^4 K.

Outside of the ejecta are the CSM zones, which in this work have either a constant density, steeply declining density $\rho \propto r^{-18}$, or wind profile ($\rho \propto r^{-2}$). They expand at a constant, low velocity and are taken to be at a temperature of 10^4 K.

Finally, outside of the CSM zones is a static "vacuum" zone of density $\rho = 10^{-24}$ g cm^{-3}, similar to the interstellar medium. The vacuum zone exists to ensure that the forward shock front and CSM are fully captured within the simulation grid at all times.

Since the CSM slows the ejecta, a Rayleigh-Taylor instability can exist at the interface between the ejecta and CSM in our simulations if the ejecta have higher density. Although a prescription for including this instability in a one-dimensional simulation now exists (Duffell, 2016), this is not used in our calculation for this work. However, between approximately days 100 and 200, the ejecta have lower density than the CSM and so the instability is not expected.

The output of the hydrodynamic code is "snapshots" of the simulation at specified linear time intervals (much longer than the time step taken in the calculation). For this work we store a snapshot every 10 [simulated] days. We then identify the shock fronts and calculate the radio and x-ray luminosity for each snapshot.

6.2.2 Radiation Transport Calculations

The synchrotron radiation parameters ϵ_B and $f_{\rm nt}$ that are most frequently used in the literature are $\epsilon_B = 0.1$ and $f_{\rm nt} = 1$; however, in this work, we treat these as unknown parameters and explore $\epsilon_B = \{0.01, 0.1\}$ and $f_{\rm nt} = \{0.01, 0.1, 1\}$. Thus there are six synchrotron configurations which we label: a, b, and c for $\epsilon_B = 0.1$ and $f_{\rm nt} = 0.01, 0.1$, and 1, respectively; and d, e, and f for $\epsilon_B = 0.01$ and the same sequence of $f_{\rm nt} = \{0.01, 0.1, 1\}$.

We stress that these parameterizations are primarily empirical and simplify (possibly, misrepresent) the true and complex physics of magnetic field amplification in shocks and electron acceleration. Chevalier (1996) makes the point that the ϵ_B parameterization is appropriate if the magnetic field is generated by turbulent motions in the gas. And while

most work assumes $f_{\rm nt} = 1$, that implies the free-free processes ought to also be from this non-thermal population, but thermal free-free is nearly always assumed.

We perform radiation transport with these emission processes with the time-independent ray-tracing method including only cells representing shocked ejecta, shocked CSM, and unshocked CSM. The labels "FS" and "FS+RS" distinguish whether we include or exclude postshock ejecta in the radiation transport calculation, respectively. Photoelectric absorption is not included in the modeled x-ray spectra but accounts for the absorption at < 3 keV in the observed spectra (the reported x-ray luminosities of Margutti et al. (2017), however, are unabsorbed). We assume that all material has solar composition and is fully ionized. One may be concerned that, because the gas can be distributed over vast distances, the travel time of light across the sphere could create an observed light curve and SED that is the *combination* of earlier-time and later-time light representing the far- and near-side gas, respectively. However, even at the latest phases we find that the light crossing time is shorter than the hydrodynamic timescale of the gas, so the SED evolution is insignificant over a light crossing time. Our calculations therefore do not account for the light travel time across the sphere.

6.2.3 The Three-Zone CSM Model

In §2.2 I described the hydrodynamic models of this work as contiguous "zones" in which gas density obeys a fixed power law radial profile. In this section I explain why the CSM configurations presented in this work consist of three zones: a thin high-density wall, an extended low-density shell, and an outer wind.

The radio light curve of A17 demonstrates that there was a low-density, wind-like CSM surrounding SN 2014C interior to the high-density region that caused the transition to a SN IIn spectrum. This low-density innermost wind is excluded from our model because, having such low mass ($\approx 10^{-4}\ M_\odot$) it does not affect the properties of the ejecta that interact with the higher-density material. The shock that was traveling through this low-density wind would reflect off of, rather than continue into, the high-density CSM region. This may explain why the radio light curve flattens between 100 and 200 days after explosion – such flattening was seen in §3.6 in models with reflected shocks (Figure 3.10).

As our first attempt to describe SN 2014C, we explored models with a single constant-density shell. Not only is this the model proposed by M17, we also have a general description for the optically thin radio light curves for such a case (Chapter 3). The model of M17 is shown in the left panel of Figure 6.2. As demonstrated in Figure 6.1, the HNK16 model with an impact time of 190 days and fractional width $f_R \equiv \Delta R/R_{\rm in} = 0.86$ fits the $t > 190$ days *rise* of the radio light curve well. Given the peak luminosity, impact time, fractional width, and frequency, this translates to a shell density $\rho_{\rm csm} \approx (4{\times}10^{-18}\ {\rm g\ cm^{-3}})\ (\epsilon_B/0.1)^{-10/11}\ f_{\rm nt}^{10/11}$ (from Equation 3.28, algebraically manipulated to use $t_{\rm imp}$ instead of inner radius). However, it is clear that this model is not a good fit to the observations overall – we identify two main issues.

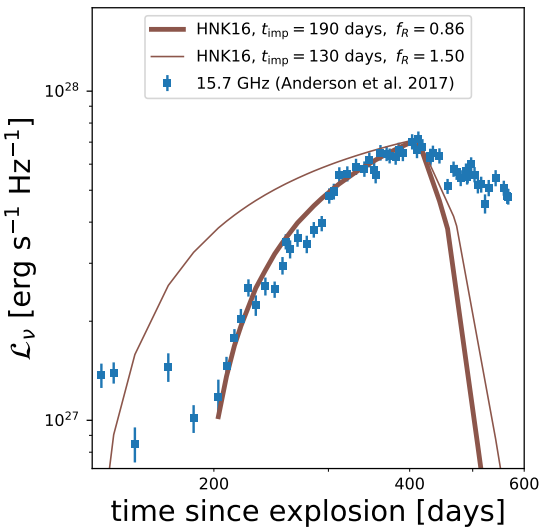

Figure 6.1: The rise of the 15.7 GHz light curve of SN 2014C (blue squares) closely matches the constant-density shell optically thin light curves, guiding the construction of the models in this work. In addition to a low-density shell responsible for the main rise, observations require a dense inner shell to obtain an impact time of 130 days without appreciable radio signal and an outer wind to match the slow decline rate.

First, the fit requires an impact time of 190 days while optical observations clearly show signs of interaction by 130 days, and a model with a 130 day impact time with the same peak luminosity does not fit. The "impact time" of these models is in fact the time that the ejecta begin to impart significant energy into the CSM – i.e. the time at which ejecta of approximately the same density as the CSM reach the CSM. So what if we include the effect of higher-velocity ejecta, such that the impact time is 130 days but the radio luminosity is lower? This does not work because, as demonstrated in §3.4, including higher-velocity ejecta leads to a more gradual rise, which would not fit the steeply-rising data better. What if the assumption that the 15.7 GHz light curve is optically thin does not hold before 190 days, such that between 130 and 190 days the radio light is simply absorbed? We simulated this possibility (increasing the shell density) and found that the rise in this case is nearly a power law and very gradual, a worse fit to the data. The failure of a single constant-density shell model to explain the 60-day delay led to the hypothesis that a thin, high-density zone of CSM interior to the constant-density shell is required. For ≥ 60 days, the ejecta pile up outside this wall, throughout which time the energy density gained by the wall is too low and the optical depth too high to result in appreciable radio signal. Once sufficiently dense ejecta have reached the wall, the wall is finally breached and an appreciable shock wave is able to energize the lower-density shell beyond.

The second failure of the single-shell models to explain the data is that the 15.7 GHz

light curve declines much more gradually than the model. The interpretation here is straightforward: the CSM shell does not have a sharp outer edge, but declines gradually into the vacuum; i.e., interaction does not "end" at the radio peak, though the radio peak does represent the shock front passing over the constant-density region.

In summary, the models presented here for SN 2014C have three CSM zones in order to match the optical and radio observations simultaneously. The innermost is a thin, high-density zone with either a constant density and sharp transition to the next zone, or a steeply declining density with no density discontinuity between the innermost and middle zones. The middle zone is responsible for the main radio signal and is a low-density constant. The outermost CSM zone is a wind profile, with no density discontinuity between it and the middle zone. An example of this profile with a steeply declining wall is shown in the right panel of Figure 6.2.

In the steeply declining wall models, there are five free parameters in the initial conditions: the impact time $t_{\rm imp}$, shell density $\rho_{\rm sh}$, and the fractional width of each zone. Figure 6.3 demonstrates the variety of these parameters explored in the models shown in this work. The color coding in this figure applies to all figures where multiple models are shown.

While it is the aim of this work to describe the CSM of SN 2014C rather than to explain how it was formed, there is precedent for such a density profile. Generally, three zones are set up in any shock or eruption: two zones of post-shock material and an outer zone of pre-shock material. The Wolf-Rayet wind-blown "bubbles" calculated by **?** are like a less compact (more distant and lower density) analog, particularly of our two inner zones. And the eruptive mass-loss episodes (novae in a symbiotic system) modeled by Dimitriadis et al. (2014) result in dense walls that are relics of the shocks. For SN 2014C perhaps there was only one eruption, in which case the outermost portion of the density profile is of interest – at late times, this profile actually looks very similar to the one we are proposing here and is only slightly more distant. It is unlikely that the massive star progenitor of SN 2014C (which must be young) was donating its mass to a white dwarf (which must be very old), but presumably the hydrodynamics of any eruption into a wind profile would look similar. If the work of Dimitriadis et al. (2014) is a good analog, then the SN 2014C outburst was $\lesssim 100$ years ago based on its distance from the progenitor.

6.3 Results

As described in the previous section, the radiation transport is performed on each simulation in six different ways (a-f) representing combinations of ϵ_B and $f_{\rm nt}$. The synchrotron emission coefficient is proportional to $\epsilon_B f_{\rm nt}^{-1}$, and the extinction coefficient is proportional to $\epsilon_B^{5/4} f_{\rm nt}^{-1}$. (The non-thermal electron fraction does not factor into the free-free emission or absorption calculation, which assumes all electrons are thermal.) It is counterintuitive that the emission increases when $f_{\rm nt}$ decreases, but this arises naturally in the normalization of the electron population (§1.3). It may be better to think of $f_{\rm nt}$ as simply a free parameter in the electron population rather than a physical quantity.

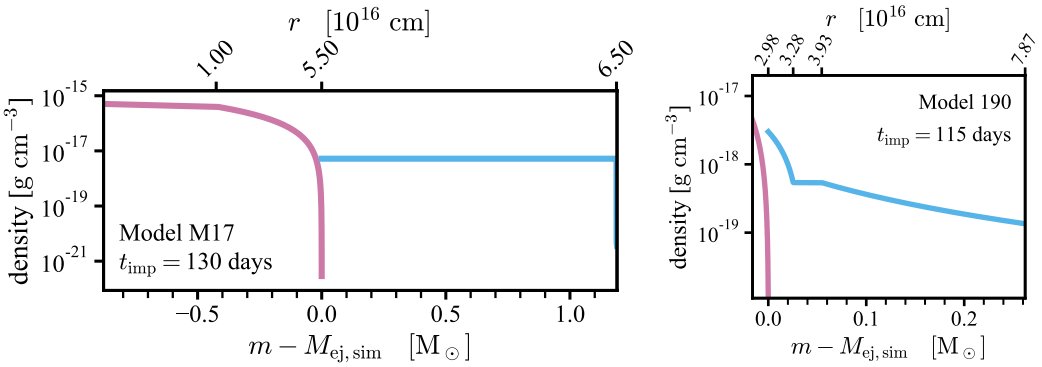

Figure 6.2: Initial mass density (ρ) profile (i.e., at time at the time of SN impact with the CSM, $t_{\rm imp}$) as a function of enclosed mass for the models presented in detail. The bottom axis gives the enclosed mass in the model, centered at the contact discontinuity between the ejecta (pink) and CSM (blue). The vacuum zones lying outside the CSM are not shown. The top axis notes the outer radius of each zone for reference – a "zone" is a region in which $\rho \propto r^{\alpha}$ for fixed α. See §6.2 for details.

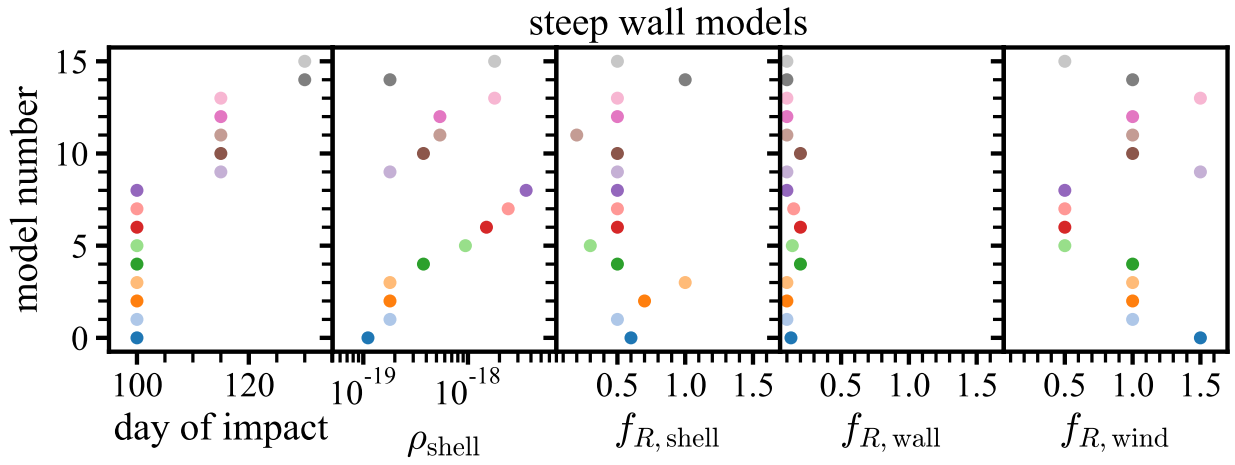

Figure 6.3: The three-zone models have five free parameters, shown here for the model suite of $s = 18$ walls. The models are ordered by their impact time, shell density, and shell fractional width.

Figures 6.4 and 6.5 show how the models in Figure 6.3 compare to the data for SN 14C, for the six different radiation assumptions. The models are labeled by their ID number in the NERSC database (§2.2). Figure 6.4 shows the ratio of the model 0.3-100 keV luminosity to the M17 unabsorbed x-ray luminosity at three epochs, showing only the calculation with the reverse shock gas included. Figure 6.5 shows the comparison in the radio for 7.1 GHz and 15.7 GHz, this time showing the comparison without (solid; preferred model) and with

(open) the shocked ejecta included in the calculation. I consider a good model to be one that is within a factor of three of the observations at most times in all three plots – i.e., I consider a model that fits the x-ray *and* radio decently to be better than a model that fits the radio perfectly but the x-ray not at all, or vice versa.

The x-ray plot would be the same for all radiation cases if the synchrotron did not contribute to the radio luminosity. The trend for case-a radiation to be higher than the other cases shows that in this case the x-ray data are dominated by synchrotron, contrary to observations (M17). In fact a general trend for case-a radiation models is that they do not simultaneously match x-ray and radio data. I was able to find a model that fit the radio data very well if the luminosity was scaled down by 5% (representing a small covering fraction of CSM). But the same reduction in luminosity then makes the x-ray luminosity far too low. Thus these figures show that radiation cases b-f are favored over case a.

Another interesting result from Figure 6.5 is that there is a degeneracy between cases b and d, and between cases c and e. I find that for the model space I explored, cases b & d perform best overall. This is interesting because they are the two cases in which $\epsilon_B = f_{\rm nt}$. Radio observations of interaction tend to focus on constraining ϵ_B alone. Furthermore, past studies have assumed case c, which in the parameter space I have explored does not match the radio evolution well because they are optically thin at 7.1 GHz.

Rules about how to assess the goodness of a model fit have emerged from this study, and it would be an interesting next step (but beyond the scope of this work) to automate the process of finding the *best* match to a set of radio and x-ray data. But the difficulty is that x-ray and radio observations must both be in hand to use the model, which is rarely realized for SNe.

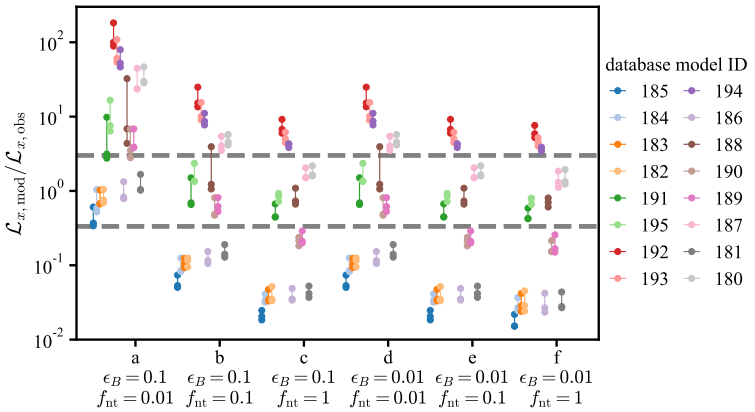

Figure 6.4: Comparison of the models presented in Figure 6.3 (color coded as in that figure) with x-ray observations for three epochs, according to the six different radiation cases a-f, including both forward and reverse shock radiation. Dashed lines indicate a luminosity three times larger or smaller than the data; the criterion for a "good" match to the x-ray is all three epochs being within this range.

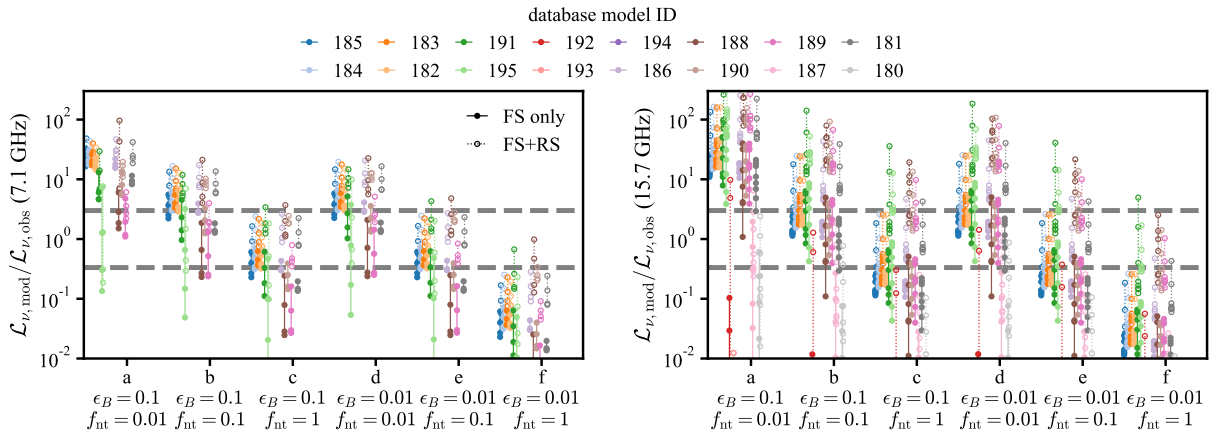

Figure 6.5: Like Figure 6.4 but for the radio light curves between 190 and 600 days. The AMI data are so frequently sampled that for clarity in this figure we only show the comparison every 50 days. Filled markers connected by solid lines are for a radio calculation using only the CSM cells, while open markers (connected by dotted lines) are the calculation with the shocked ejecta as well.

Now I will focus on one model that meets the criteria for a "good match": Model 190b. The initial conditions for Model 190 are shown in Figure 6.2. Model 190 has $M_{\mathrm{csm}} \approx 0.28\ M_\odot$, impact time of 115 days, and a thin ($f_R = 0.2$) low-density ($\rho_{\mathrm{csm}} \approx 5 \times 10^{-19}$ g cm^{-3}) middle shell. With the given f_{nt} and ϵ_B of case b, the middle shell density agrees extremely well with the shell density estimate obtained by fitting the 15.7 GHz peak with one of my parameterized radio light curves (§6.2). Its nearest $t_{\mathrm{imp}} = 100$ days analog is Model 195.

The case-b radiation of this model is shown in Figures 6.6 and 6.7; in these figures, the times that the shock moves into the middle shell and then into the wind are indicated by dashed lines. In the radio, we favor the calculation that includes only the CSM, because the ejecta should not be turbulent at early times and therefore should not have a magnetic field enhancement described by the ϵ_B parameterization. In the x-ray, which is thermal, we favor the calculation that includes the shocked ejecta.

The comparison is not astoundingly good: the radio is somewhat high and the x-ray somewhat low. This model is dominated by free-free absorption in the radio, which is sensitive to the total amount of CSM outside of the shock region, so the radio SED at 295 days looks like a worse match than it is. However, the general shape of the light curve, particularly the time at which the 7.1 GHz light curve intersects the 15.7 GHz light curve (an indicator of optical depth evolution), the steepness of the radio rise, and the slope of the x-ray decline, are all decent matches to the data. This indicates that the CSM of SN 2014C may resemble that of Model 190.

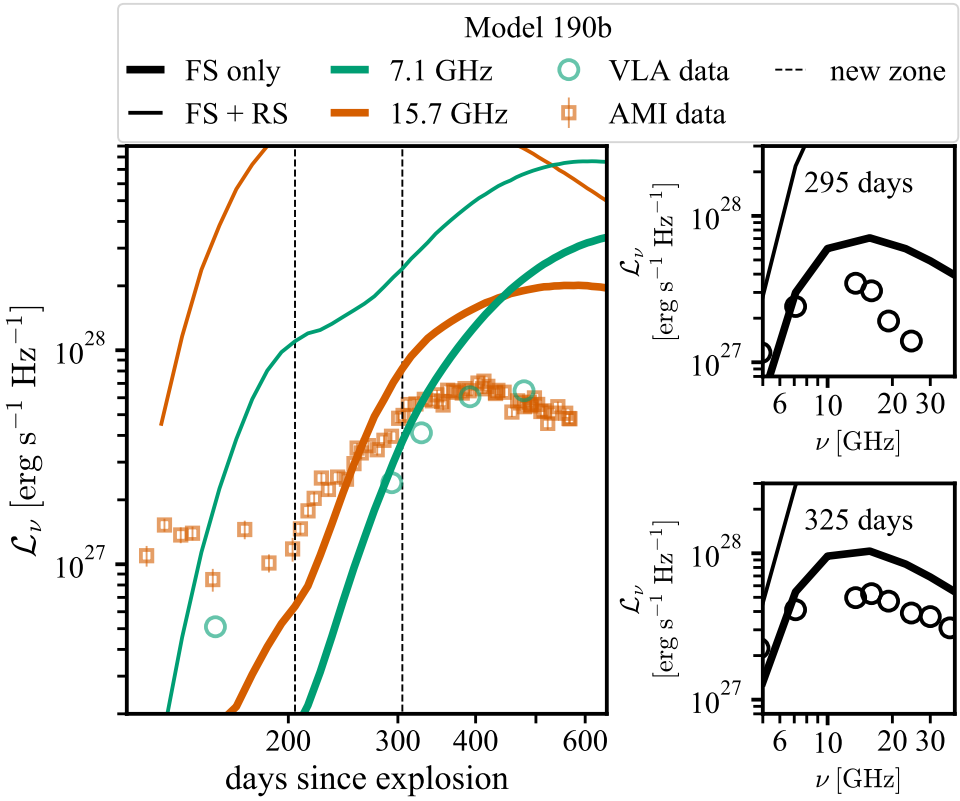

Figure 6.6: The radio light curves of Model 190b (light brown in Figures 6.3, 6.4, and 6.6). Our preferred model is to consider the luminosity of the forward shock only, since it is unclear to what extent magnetic fields are amplified in the ejecta at early times. Though not an exact match, the model does a decent job of recovering the luminosity normalization, the evolution of the optically thin 15.7 GHz light curve, the evolution of the optical depth (tracked by comparing the 7.1 and 15.7 GHz light curves), and the shape of the radio SEDs (though absorption is too high at 300 days).

6.4 Conclusions

I ran simulations of SN Ib ejecta interacting with a complex CSM structure at $\approx 10^{16}$ cm from the progenitor with the aim of constraining the CSM of SN 2014C. The CSM I consider consists of a very thin dense wall of material that steeply falls into a constant-density region, outside of which is a wind. The existence of a thin, high-density wall approximately ten times more dense than the outlying material is consistent with this CSM being shaped by an eruption, and the wall being a remnant cool dense shell.

The optical transformation is caused by the SN ejecta impacting the dense wall, while the radio rise occurs later when the ejecta are finally able to drive a shock through the wall and into the less dense middle shell. X-ray data between 100 and 300 days would have been

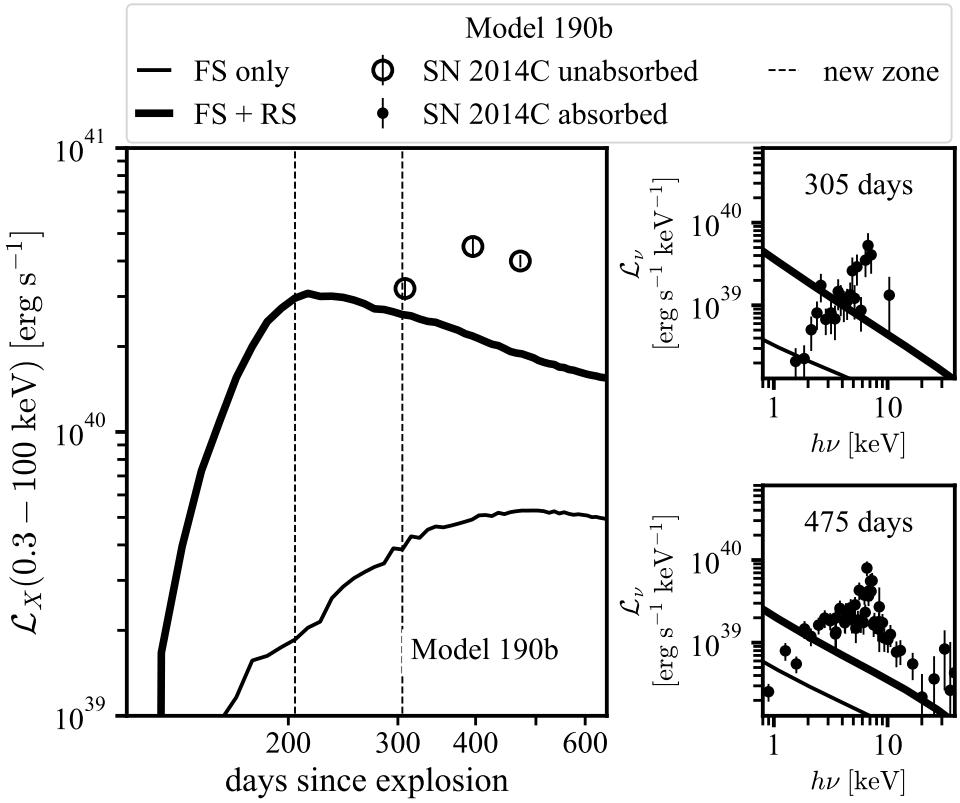

Figure 6.7: The x-ray light curves of Model 190b (light brown in Figures 6.3 - 6.5). Our preferred model is to consider the luminosity of the forward and reverse shocks together, since this is thermal radiation. While not a perfect match, the luminosity is within a factor of three of observations.

a valuable test of this hypothesis.

For each model I calculate the radiation from synchrotron and bremsstrahlung processes to simultaneously calculate x-ray and radio light curves. This is the first instance of such analysis for a delayed-interaction SN. I perform the calculation both including and excluding the shocked ejecta, and in six different radiation cases representing different combinations of $\epsilon_B = 0.01, 0.1$ and $f_{\rm nt} = 0.01, 0.1, 1$. In the literature it is typically assumed that $\epsilon_B = 0.1$ and $f_{\rm nt} = 1$.

From the ensemble of model light curves, I find that

1. The best matches to the radio and x-ray data simultaneously are achieved with $\epsilon_B = f_{\rm nt} = 0.1$ or $\epsilon_B = f_{\rm nt} = 0.01$.

2. Because the free-free emission is largely independent of the synchrotron parameters, it is a good initial diagnostic of a model's viability.

3. The radio light curves fit best when the reverse shock is excluded, because otherwise the radio luminosity is too high before 200 days to match the observations. Excluding the reverse shock is physically motivated by the fact that the ejecta should not be turbulent for the first ≈ 100 days while the ejecta have lower density than the CSM, and turbulence is the driver of magnetic field amplification in the ϵ_B parameterization.

4. The thermal free-free emission would be relevant for the reverse shock, however. Thus, the best fits presented here imply that between 100 and 200 days, which was unobserved in the x-ray, the x-ray would have been bright while the radio was dim. This may be an important diagnostic for future studies of delayed-interaction supernovae to study the growth of the shock.

A goal for future work would be to use the model suite now in hand to create an actual fitting routine rather than attempting to continue finding the best match by human review.

Model 190b is one of the best overall matches to the data of SN 2014C that I found and weighs in at only 0.28 $M_\odot$, only about 10% of which is in the dense wall. This is in contrast to the model of M17, which used the self-similar asymptotic solution for shock evolution to analyze the radio and x-ray data and posited approximately 1 $M_\odot$ of material in the dense wall. However, it is in excellent agreement with the optically thin models of Chapter 3, which when applied to the 15.7 GHz light curve estimated that the low-density shell was responsible for the radio rise and had a density $(4\times10^{-18}$ g cm$^{-3})(\epsilon_B/0.1)^{-10/11} f_{\rm nt}^{10/11}$ (Model 190b has $\epsilon_B = f_{\rm nt} = 0.1$).

Chapter 7

Conclusion: Where Do We Go Now?

The focus of this thesis is to discover new tools for constraining the existence and properties of CSM around SNe I, with the primary aim of understanding the progenitors of SNe Ia. For SNe Ia, the CSE elucidates the nature of the mass donor binary companion to the CO WD that explodes. The CSM may be shaped by violent mass-loss episodes that create a cavity around the SN and a thin, dense shell of CSM outside the cavity. In this case, normal SN signatures will be visible for the first month(s), and then interaction with the CSM will begin and the observed radiation will reflect the interaction. I label SNe with such an interaction timeline as SNe X;n – i.e., such an SN Ia would be called an SN Ia;n.

Interaction of SNe Ia had only been newly confirmed when I began my doctoral work, the debate settled by PTF11kx. But several things were known: the majority of normal SNe Ia do not have CSM from MS or RG stellar winds; only 91T-like SNe Ia are observed to interact with CSM (SNe Ia-CSM); interaction in SNe Ia can begin weeks after maximum light; and promptly interacting SNe Ia seem to have very dense CSM, but the density estimates from different indicators give different results.

The CSM properties are deduced through observations of the radiation from the shock wave that forms when the SN collides with the CSM. Shock waves heat the CSM and ejecta, and the magnetic fields in a shocked gas may be amplified to create populations of non-thermal electrons. The radiation from shocks is panchromatic. The easiest signatures to interpret are the radio synchrotron and thermal x-ray emission. Yet the signatures that are most likely to be observed are those in the optical, because this is where the SN itself radiates. Atomic lines in the optical spectra are particularly useful indicators of the gas composition and kinematics, but require sophisticated transport calculations to interpret with confidence.

Indeed, all translation of shock observations into CSM constraints relies on theoretical modeling of the shock evolution, even the radio and x-ray. Thus, the most popular framework for interpretation is that which is flexible, easy to apply to many observations at once: the Chevalier (1982a) self-similar model. Particularly for radio and x-ray data, this model was essentially the only one ever applied to the interpretation of x-ray and radio data to quantitatively constrain the CSM of SNe I. It worked well for core-collapse SNe, including

SNe Ibc, for which a wind CSM described the data. However, the model has limited application because it is an asymptotic solution, applicable only if the ejecta and CSM densities can each be described by a single power law in radius and observations are at times long after the interaction began. This means that the self-similar model does not apply to SNe X;n, where observations are taken shortly after the start of interaction. It also does not apply to observations after interaction has ended, or when the CSM density profile changes. Both of these limitations made the self-similar model inapplicable for constraining the presence and properties of nova shells around SNe Ia. Finally, the self-similar solution only applies while the shocked CSM mass is a small fraction ($\approx 10\%$) of the total ejecta mass, such that the reverse shock front is within the outer ejecta. For SNe Ia, the outer ejecta mass is only $\approx 0.15\ M_{\odot}$.

Thus although the hydrodynamic and radiation transport calculations I have presented in this thesis are one-dimensional and quite parameterized as described in Chapter 2, they actually represent the state of the art in studies of delayed interaction supernovae. In my doctoral work I focus on what I call transitional phases of interaction – i.e., times when the shock is newly formed or encountering a new density profile. The shock may even completely sweep over the CSM and dissipate, leaving the shocked CSM to expand into a vacuum.

The first contribution I made to the field with these models was a tool for studying radio observations (including non-detections) of nova shell interaction (Chapter 3). These shells have such low densities that the synchrotron radio light is optically thin. I discovered a family of models whose synchrotron light curves are determined by three parameters: the time of impact, width of the shell, and shell density. The peak luminosity, time of peak, shape of the rise, and decline rate after peak are all described by a simple set of analytic expressions. This tool is as easy to use as the self-similar model light curves. In the chapter introducing these models, I applied them to analyze the multi-epoch radio non-detections of SN 2011fe and SN 2014J. I found that nova shells were unlikely to have been detected in either of these datasets, and demonstrated how the probability of detection varies as a function of the shell properties.

I then extended the models to late times and thicker shells to study PTF11kx. In this case, I wanted to know whether the reverse shock produced enough ionizing radiation to stimulate an Hα line long after the shock had swept through the bulk of the CSM. This challenges the assumption that the Hα line strength is a diagnostic for continued interaction, as had been assumed in studies of interacting core-collapse supernovae. I found that the x-ray luminosity (and the hydrogen ionizing luminosity) was approximately the same as the Hα luminosity; this had been previously suggested by a model of high-energy emission stimulating Hα. No x-ray observations exist to confirm or refute the predicted level of x-ray emission. I found that the expansion of the CSM after interaction has ended causes a decrease in the optical depth such that less ionizing radiation is absorbed over time; if the Hα luminosity tracks the luminosity of these photons, then it too will have a steeper decline than the x-ray light. However, I found that with the simplest treatment of the reprocessing of the ionizing emission, I could not reproduce the observed Hα luminosity. This could still be because the reprocessing calculation was overly simplistic.

My work on PTF11kx led to my involvement in an effort to discover more SNe Ia;n using the *Hubble Space Telescope*. Such a survey was made possible in part by my models, which promised an avenue that had not previously existed for interpreting the results of such a study. The program design was to obtain single-epoch photometric observations in the near-UV of nearby 1- to 3-year-old SNe Ia, with 91T-like SNe Ia highly represented in the sample. This program discovered interaction in SN 2015cp (a 91T-like SN Ia) at 676 days post-explosion. After discovery of interaction, we executed panchromatic follow-up observations of this object including radio and x-ray. My modeling of PTF11kx informed us that radio and x-ray observations were sufficient to observe a PTF11kx analog, even though at this age the interaction would be over. Yet the radio and x-ray observations resulted in deep non-detections. These data could still be used, however, because my radio analysis tools apply to non-detections, as previously demonstrated. My analysis showed that while the extent of the CSM in SN 2015cp is highly uncertain, with my preferred conservative assumption for the time interaction ended my modeling limits the CSM mass to $M_{\rm csm} < 0.5\ M_\odot$. One important result of my analysis was to show that obtaining radio follow-up data as quickly as possible is key for future campaigns. This indicates a preference for using a flexible instrument like AMI over a more sophisticated but bureaucratically cumbersome instrument like the VLA.

Finally, I showed how my models perform when applied to radio *detections*. In this case it was of the Type Ib;n SN 2014C. As a stripped-envelope CC SN, SN 2014C had an ejecta density profile very similar to that of an SN Ia. The timescale of its interaction was also similar to that of SNe Ia;n. However, the CSM of SN 2014C was likely shaped by physical processes quite different from those at play in SNe Ia. In fact, the disparity between the emergence of interaction signatures at optical and radio wavelengths suggests that the CSM of SN 2014C consisted of a high-density, thin wall of material with a lower density, more extended shell beyond it. The challenge for SN 2014C was to simultaneously reproduce the panchromatic dataset from a single model. As far as I am aware, this has never before been attempted; rather, panchromatic datasets are used to create a bolometric light curve for comparison to theoretical models, which not only wastes the physical information from different wavelengths but also introduces errors from creating the bolometric light curve. For these models, therefore, I explored a new parameter space of CSM configurations and compared the model synchrotron and x-ray light curves to the data. Another novel extension in this work was to calculate the synchrotron emission with different assumptions for the radiation parameters. While typically $\epsilon_B = 0.1$ and $f_{\rm nt} = 1$ are employed (including in my own work), I find that $\epsilon_B = f_{\rm nt} = 0.1$ or 0.01 generally matched best for the models I explored. I also found that a model with just 0.3 $M_\odot$ of material can reproduce the x-ray and radio luminosities. Finally I applied my single-shell radio light curve parameterization to the optically thin AMI radio light curve of SN 2014C to estimate the density of the main shell. The density returned by my parameterized light curve formulae is in very good agreement with one of my best-matching complex-CSM models.

To conclude this thesis, I would like to share my view of what the future holds for SNe Ia;n. First of all, I think the picture is emerging that 91T-like SNe Ia are associated with CSM and thus may represent SNe Ia from the SD channel. Determining whether this is the

case ought to be top priority for SN Ia research over the next decade.

This must be in part the responsibility of observers, to doggedly pursue all 91T-likes in the nearby universe. Though 91T-likes are rare, large-sky surveys like that of the *Zwicky Transient Facility* (ZTF) and that of the *Large Synoptic Survey Telescope* (LSST) will increase the number known. Efforts for these large-scale surveys are focusing intently on classifying SNe through photometry alone. Because the calcium deficiency of SN 1991T may be important, part of the study of these objects must be obtaining spectra of them. I think that one of the reasons SNe Ia;n have not been observed more often, aside from their association with 91T-likes, is that the interaction begins after most observations of SNe have ended. ZTF and LSST will revolutionize this, because these surveys automatically obtain photometry of sources over years-long baselines. Interaction is revealed in R-band photometry as an extreme flattening of the light curve after peak. Studies of the ensemble datasets themselves will allow us to constrain the frequency of delayed interaction. But more can be done by triggering follow-up observations of such errant SNe Ia, as they are found. Our analysis of SN 2015cp shows how much can be done with three monthly optical spectra and rapid AMI follow-up observations of a nearby source, and that was in the extremely unfavorable case where there was a years-long gap in observations for the object and interaction was discovered only after the CSM had been swept over. So I think that the next decade will see a large increase in the number of SNe X;n discovered, due to these untargeted wide-field surveys.

From the theoretical side, I would like to create tools for accurately interpreting optical observations of SNe Ia-CSM. One of my main goals in this is to understand the evolution of the Hα line strength. As we saw in my analysis of PTF11kx, lacking an understanding of line excitation after interaction has ended severely limits our ability to determine the extent of the CSM. (This may be true for SNe IIn as well.) But more importantly, SN Ia research is largely in the optical, particularly emphasizing photometric observations, on account of SN cosmology. I think it is important to bring the interaction theory into line with how SN observations are performed. If I could create a tool to constrain CSM properties from optical photometry alone, it would probably be the single biggest contribution to our understanding of interaction in the next decade.

Once we have seen more SNe Ia;n and we know what their CSM looks like, the real fun will be for the stellar evolution theorists to figure out how the CSM is formed! Here again my simulations can be straightforwardly adapted to testing the viability of models by calculating their radiation signatures.

Bibliography

Alsabti, A. W. and P. Murdin
2017. *Handbook of Supernovae*.

Anderson, G. E., A. Horesh, K. P. Mooley, A. P. Rushton, R. P. Fender, T. D. Staley, M. K. Argo, R. J. Beswick, P. J. Hancock, M. A. Pérez-Torres, Y. C. Perrott, R. M. Plotkin, M. L. Pretorius, C. Rumsey, and D. J. Titterington
2017. The peculiar mass-loss history of SN 2014C as revealed through AMI radio observations. MNRAS, 466:3648–3662.

Arnett, W. D.
1968. Explosive Ignition of Carbon in Stars of Intermediate Mass. Nature, 219:1344–1346.

Bianco, F. B., D. A. Howell, M. Sullivan, A. Conley, D. Kasen, S. González-Gaitán, J. Guy, P. Astier, C. Balland, R. G. Carlberg, D. Fouchez, N. Fourmanoit, D. Hardin, I. Hook, C. Lidman, R. Pain, N. Palanque-Delabrouille, S. Perlmutter, K. M. Perrett, C. J. Pritchet, N. Regnault, J. Rich, and V. Ruhlmann-Kleider
2011. Constraining Type Ia Supernovae Progenitors from Three Years of Supernova Legacy Survey Data. ApJ, 741:20.

Bloom, J. S., D. Kasen, K. J. Shen, P. E. Nugent, N. R. Butler, M. L. Graham, D. A. Howell, U. Kolb, S. Holmes, C. A. Haswell, V. Burwitz, J. Rodriguez, and M. Sullivan
2012. A Compact Degenerate Primary-star Progenitor of SN 2011fe. ApJ, 744:L17.

Bochenek, C. D., V. V. Dwarkadas, J. M. Silverman, O. D. Fox, R. A. Chevalier, N. Smith, and A. V. Filippenko
2018. X-ray emission from SN 2012ca: A Type Ia-CSM supernova explosion in a dense surrounding medium. MNRAS, 473:336–344.

Boffi, F. R. and D. Branch
1995. Radio Emission from Type IA Supernovae as a Test of Symbiotic Star Progenitor Systems. PASP, 107:347.

Borkowski, K. J., J. M. Blondin, and S. P. Reynolds
2009. Circumstellar Shells in Absorption in Type Ia Supernovae. ApJ, 699:L64–L67.

Botyánszki, J., D. Kasen, and T. Plewa
2018. Multidimensional Models of Type Ia Supernova Nebular Spectra: Strong Emission Lines from Stripped Companion Gas Rule Out Classic Single-degenerate Systems. ApJ, 852:L6.

Branch, D., A. Fisher, and P. Nugent
1993. On the relative frequencies of spectroscopically normal and peculiar type IA supernovae. AJ, 106:2383–2391.

Branch, D., M. Livio, L. R. Yungelson, F. R. Boffi, and E. Baron
1995. In Search of the Progenitors of Type IA Supernovae. PASP, 107:1019.

Branch, D. and K. Nomoto
1986. Supernovae of Type Ib as off-center explosions in accreting white dwarfs? A&A, 164:L13–L15.

Branch, D. and J. C. Wheeler
2017. *Supernova Explosions*.

Bulla, M., A. Goobar, and S. Dhawan
2018. Resolving the Type Ia supernova extinction puzzle: dust location found. *ArXiv e-prints*.

Cao, Y., S. R. Kulkarni, D. A. Howell, A. Gal-Yam, M. M. Kasliwal, S. Valenti, J. Johansson, R. Amanullah, A. Goobar, J. Sollerman, F. Taddia, A. Horesh, I. Sagiv, S. B. Cenko, P. E. Nugent, I. Arcavi, J. Surace, P. R. Woźniak, D. I. Moody, U. D. Rebbapragada, B. D. Bue, and N. Gehrels
2015. A strong ultraviolet pulse from a newborn type Ia supernova. Nature, 521:328–331.

Castor, J. I.
2007. *Radiation Hydrodynamics*.

Chevalier, R. A.
1982a. Self-similar solutions for the interaction of stellar ejecta with an external medium. ApJ, 258:790–797.

Chevalier, R. A.
1982b. The radio and X-ray emission from type II supernovae. ApJ, 259:302–310.

Chevalier, R. A.
1996. The Circumstellar Interaction Model for Radio Supernovae. In *Radio Emission from the Stars and the Sun*, A. R. Taylor and J. M. Paredes, eds., volume 93 of *Astronomical Society of the Pacific Conference Series*, P. 125.

Chevalier, R. A.
1998. Synchrotron Self-Absorption in Radio Supernovae. ApJ, 499:810–819.

Chevalier, R. A. and C. Fransson
1994. Emission from circumstellar interaction in normal Type II supernovae. ApJ, 420:268–285.

Chevalier, R. A. and C. Fransson
2006. Circumstellar Emission from Type Ib and Ic Supernovae. ApJ, 651:381–391.

Chevalier, R. A. and E. P. Liang
1989. The interaction of supernovae with circumstellar bubbles. ApJ, 344:332–340.

Chomiuk, L., A. M. Soderberg, R. A. Chevalier, S. Bruzewski, R. J. Foley, J. Parrent, J. Strader, C. Badenes, C. Fransson, A. Kamble, R. Margutti, M. P. Rupen, and J. D. Simon
2016. A Deep Search for Prompt Radio Emission from Thermonuclear Supernovae with the Very Large Array. ApJ, 821:119.

Chomiuk, L., A. M. Soderberg, M. Moe, R. A. Chevalier, M. P. Rupen, C. Badenes, R. Margutti, C. Fransson, W.-f. Fong, and J. A. Dittmann
2012. EVLA Observations Constrain the Environment and Progenitor System of Type Ia Supernova 2011fe. ApJ, 750:164.

Chugai, N. N. and I. J. Danziger
1994. Supernova 1988Z - Low-Mass Ejecta Colliding with the Clumpy Wind. MNRAS, 268:173.

Churazov, E., R. Sunyaev, J. Isern, I. Bikmaev, E. Bravo, N. Chugai, S. Grebenev, P. Jean, J. Knödlseder, F. Lebrun, and E. Kuulkers
2015. Gamma-rays from Type Ia Supernova SN2014J. ApJ, 812:62.

Colgate, S. A. and C. McKee
1969. Early Supernova Luminosity. ApJ, 157:623.

Colgate, S. A. and R. H. White
1966. The Hydrodynamic Behavior of Supernovae Explosions. ApJ, 143:626.

Condon, J. J., W. D. Cotton, E. W. Greisen, Q. F. Yin, R. A. Perley, G. B. Taylor, and J. J. Broderick
1998. The NRAO VLA Sky Survey. AJ, 115:1693–1716.

Couch, S. M.
2017. The mechanism(s) of core-collapse supernovae. *Philosophical Transactions of the Royal Society of London Series A*, 375:20160271.

Diehl, R., T. Siegert, W. Hillebrandt, M. Krause, J. Greiner, K. Maeda, F. K. Röpke, S. A. Sim, W. Wang, and X. Zhang
2015. SN2014J gamma rays from the ^{56}Ni decay chain. A&A, 574:A72.

Dilday, B., D. A. Howell, S. B. Cenko, J. M. Silverman, P. E. Nugent, M. Sullivan, S. Ben-Ami, L. Bildsten, M. Bolte, M. Endl, A. V. Filippenko, O. Gnat, A. Horesh, E. Hsiao, M. M. Kasliwal, D. Kirkman, K. Maguire, G. W. Marcy, K. Moore, Y. Pan, J. T. Parrent, P. Podsiadlowski, R. M. Quimby, A. Sternberg, N. Suzuki, D. R. Tytler, D. Xu, J. S. Bloom, A. Gal-Yam, I. M. Hook, S. R. Kulkarni, N. M. Law, E. O. Ofek, D. Polishook, and D. Poznanski
2012. PTF 11kx: A Type Ia Supernova with a Symbiotic Nova Progenitor. *Science*, 337:942–.

Dimitriadis, G., A. Chiotellis, and J. Vink
2014. Early X-ray emission from Type Ia supernovae originating from symbiotic progenitors or recurrent novae. MNRAS, 443:1370–1380.

Duffell, P. C.
2016. A One-Dimensional Model for Rayleigh-Taylor Instability in Supernova Remnants. ApJ, 821:76.

Dwarkadas, V. V. and J. Gruszko
2012. What are published X-ray light curves telling us about young supernova expansion? MNRAS, 419:1515–1524.

Eck, C. R., J. J. Cowan, D. A. Roberts, F. R. Boffi, and D. Branch
1995. Radio Observations of the Type IA Supernova 1986G as a Test of a Symbiotic-Star Progenitor. ApJ, 451:L53.

Elias, J. H., K. Matthews, G. Neugebauer, and S. E. Persson
1985. Type I supernovae in the infrared and their use as distance indicators. ApJ, 296:379–389.

Fermi, E.
1949. On the Origin of the Cosmic Radiation. *Physical Review*, 75:1169–1174.

Ferretti, R., R. Amanullah, M. Bulla, A. Goobar, J. Johansson, and P. Lundqvist
2017. No Evidence of Circumstellar Gas Surrounding Type Ia Supernova SN 2017cbv. ApJ, 851:L43.

Filippenko, A. V.
1988. Supernova 1987K - Type II in youth, type Ib in old age. AJ, 96:1941–1948.

Filippenko, A. V.
1997. Optical Spectra of Supernovae. ARA&A, 35:309–355.

Filippenko, A. V., M. W. Richmond, T. Matheson, J. C. Shields, E. M. Burbidge, R. D. Cohen, M. Dickinson, M. A. Malkan, B. Nelson, J. Pietz, D. Schlegel, P. Schmeer, H. Spinrad, C. C. Steidel, H. D. Tran, and W. Wren
1992. The peculiar Type IA SN 1991T - Detonation of a white dwarf? ApJ, 384:L15–L18.

Finzi, A. and R. A. Wolf
1967. Type i Supernovae. ApJ, 150:115.

Fox, O. D. and A. V. Filippenko
2013. The Late-time Rebrightening of Type Ia SN 2005gj in the Mid-infrared. ApJ, 772:L6.

Fox, O. D., A. V. Filippenko, M. F. Skrutskie, J. M. Silverman, M. Ganeshalingam, S. B. Cenko, and K. I. Clubb
2013. Late-time Circumstellar Interaction in a Spitzer Selected Sample of Type IIn Supernovae. AJ, 146:2.

Fransson, C.
1982. X-ray and UV-emission from supernova shock waves in stellar winds. A&A, 111:140–150.

Fransson, C.
1984a. Comptonization and UV emission lines from Type II supernovae. A&A, 133:264–284.

Fransson, C.
1984b. Line profiles from supernovae. A&A, 132:115–126.

Garavini, G., G. Folatelli, A. Goobar, S. Nobili, G. Aldering, A. Amadon, R. Amanullah, P. Astier, C. Balland, G. Blanc, M. S. Burns, A. Conley, T. Dahlén, S. E. Deustua, R. Ellis, S. Fabbro, X. Fan, B. Frye, E. L. Gates, R. Gibbons, G. Goldhaber, B. Goldman, D. E. Groom, J. Haissinski, D. Hardin, I. M. Hook, D. A. Howell, D. Kasen, S. Kent, A. G. Kim, R. A. Knop, B. C. Lee, C. Lidman, J. Mendez, G. J. Miller, M. Moniez, A. Mourão, H. Newberg, P. E. Nugent, R. Pain, O. Perdereau, S. Perlmutter, V. Prasad, R. Quimby, J. Raux, N. Regnault, J. Rich, G. T. Richards, P. Ruiz-Lapuente, G. Sainton, B. E. Schaefer, K. Schahmaneche, E. Smith, A. L. Spadafora, V. Stanishev, N. A. Walton, L. Wang, W. M. Wood-Vasey, and Supernova Cosmology Project
2004. Spectroscopic Observations and Analysis of the Peculiar SN 1999aa. AJ, 128:387–404.

Gerardy, C. L., P. Höflich, R. A. Fesen, G. H. Marion, K. Nomoto, R. Quimby, B. E. Schaefer, L. Wang, and J. C. Wheeler
2004. SN 2003du: Signatures of the Circumstellar Environment in a Normal Type Ia Supernova? ApJ, 607:391–405.

Graham, M. L., C. E. Harris, O. D. Fox, P. E. Nugent, D. Kasen, J. M. Silverman, and A. V. Filippenko
2017a. PTF11kx: A Type Ia Supernova with Hydrogen Emission Persisting after 3.5 Years. ApJ, 843:102.

Graham, M. L., S. Kumar, G. Hosseinzadeh, D. Hiramatsu, I. Arcavi, D. A. Howell, S. Valenti, D. J. Sand, J. T. Parrent, C. McCully, and A. V. Filippenko
2017b. Nebular-phase spectra of nearby Type Ia Supernovae. MNRAS, 472:3437–3454.

Harris, C. E., P. E. Nugent, and D. N. Kasen
2016. Against the Wind: Radio Light Curves of Type Ia Supernovae Interacting with Low-density Circumstellar Shells. ApJ, 823:100.

Hayden, B. T., P. M. Garnavich, D. Kasen, B. Dilday, J. A. Frieman, S. W. Jha, H. Lampeitl, R. C. Nichol, M. Sako, D. P. Schneider, M. Smith, J. Sollerman, and J. C. Wheeler
2010. Single or Double Degenerate Progenitors? Searching for Shock Emission in the SDSS-II Type Ia Supernovae. ApJ, 722:1691–1698.

Hickish, J., N. Razavi-Ghods, Y. C. Perrott, D. J. Titterington, S. H. Carey, P. F. Scott, K. J. B. Grainge, A. M. M. Scaife, P. Alexander, R. D. E. Saunders, M. Crofts, K. Javid, C. Rumsey, T. Z. Jin, J. A. Ely, C. Shaw, I. G. Northrop, G. Pooley, R. D'Alessandro, P. Doherty, and G. P. Willatt
2018. A digital correlator upgrade for the Arcminute MicroKelvin Imager. MNRAS, 475:5677–5687.

Hosseinzadeh, G., D. J. Sand, S. Valenti, P. Brown, D. A. Howell, C. McCully, D. Kasen, I. Arcavi, K. Azalee Bostroem, L. Tartaglia, E. Y. Hsiao, S. Davis, M. Shahbandeh, and M. D. Stritzinger
2017. Early Blue Excess from the Type Ia Supernova 2017cbv and Implications for Its Progenitor. ApJ, 845:L11.

Hoyle, F. and W. A. Fowler
1960. Nucleosynthesis in Supernovae. ApJ, 132:565.

Immler, S., W. Pietsch, and B. Aschenbach
1998. Evidence for X-ray emission from the type IC supernova 1994I. A&A, 336:L1–L4.

Jones, F. C. and D. C. Ellison
1991. The plasma physics of shock acceleration. Space Sci. Rev., 58:259–346.

Kalberla, P. M. W., W. B. Burton, D. Hartmann, E. M. Arnal, E. Bajaja, R. Morras, and W. G. L. Pöppel
2005. The Leiden/Argentine/Bonn (LAB) Survey of Galactic HI. Final data release of the combined LDS and IAR surveys with improved stray-radiation corrections. A&A, 440:775–782.

Kasen, D.
2010. Seeing the Collision of a Supernova with Its Companion Star. ApJ, 708:1025–1031.

Katsuda, S., K. Mori, K. Maeda, M. Tanaka, K. Koyama, H. Tsunemi, H. Nakajima, Y. Maeda, M. Ozaki, and R. Petre
2015. Kepler's Supernova: An Overluminous Type Ia Event Interacting with a Massive Circumstellar Medium at a Very Late Phase. ApJ, 808:49.

Kromer, M., C. Fremling, R. Pakmor, S. Taubenberger, R. Amanullah, S. B. Cenko, C. Fransson, A. Goobar, G. Leloudas, F. Taddia, F. K. Röpke, I. R. Seitenzahl, S. A. Sim, and J. Sollerman
2016. The peculiar Type Ia supernova iPTF14atg: Chandrasekhar-mass explosion or violent merger? MNRAS, 459:4428–4439.

Leloudas, G., E. Y. Hsiao, J. Johansson, K. Maeda, T. J. Moriya, J. Nordin, T. Petrushevska, J. M. Silverman, J. Sollerman, M. D. Stritzinger, F. Taddia, and D. Xu
2015. Supernova spectra below strong circumstellar interaction. A&A, 574:A61.

Leonard, D. C.
2007. Constraining the Type Ia Supernova Progenitor: The Search for Hydrogen in Nebular Spectra. ApJ, 670:1275–1282.

Li, W., J. Leaman, R. Chornock, A. V. Filippenko, D. Poznanski, M. Ganeshalingam, X. Wang, M. Modjaz, S. Jha, R. J. Foley, and N. Smith
2011. Nearby supernova rates from the Lick Observatory Supernova Search - II. The observed luminosity functions and fractions of supernovae in a complete sample. MNRAS, 412:1441–1472.

Liu, Z.-W. and R. J. Stancliffe
2016. Constraining the progenitor of the Type Ia Supernova SN 2012cg. MNRAS, 459:1781–1789.

Livne, E., Y. Tuchman, and J. C. Wheeler
1992. Explosion of a supernova with a red giant companion. ApJ, 399:665–671.

Lundqvist, P., A. Nyholm, F. Taddia, J. Sollerman, J. Johansson, C. Kozma, N. Lundqvist, C. Fransson, P. M. Garnavich, M. Kromer, B. J. Shappee, and A. Goobar
2015. No trace of a single-degenerate companion in late spectra of supernovae 2011fe and 2014J. A&A, 577:A39.

Maguire, K., S. Taubenberger, M. Sullivan, and P. A. Mazzali
2016. Searching for swept-up hydrogen and helium in the late-time spectra of 11 nearby Type Ia supernovae. MNRAS, 457:3254–3265.

Margutti, R., A. Kamble, D. Milisavljevic, E. Zapartas, S. E. de Mink, M. Drout, R. Chornock, G. Risaliti, B. A. Zauderer, M. Bietenholz, M. Cantiello, S. Chakraborti,

L. Chomiuk, W. Fong, B. Grefenstette, C. Guidorzi, R. Kirshner, J. T. Parrent, D. Patnaude, A. M. Soderberg, N. C. Gehrels, and F. Harrison
2017. Ejection of the Massive Hydrogen-rich Envelope Timed with the Collapse of the Stripped SN 2014C. ApJ, 835:140.

Margutti, R., J. Parrent, A. Kamble, A. M. Soderberg, R. J. Foley, D. Milisavljevic, M. R. Drout, and R. Kirshner
2014. No X-Rays from the Very Nearby Type Ia SN 2014J: Constraints on Its Environment. ApJ, 790:52.

Margutti, R., A. M. Soderberg, L. Chomiuk, R. Chevalier, K. Hurley, D. Milisavljevic, R. J. Foley, J. P. Hughes, P. Slane, C. Fransson, M. Moe, S. Barthelmy, W. Boynton, M. Briggs, V. Connaughton, E. Costa, J. Cummings, E. Del Monte, H. Enos, C. Fellows, M. Feroci, Y. Fukazawa, N. Gehrels, J. Goldsten, D. Golovin, Y. Hanabata, K. Harshman, H. Krimm, M. L. Litvak, K. Makishima, M. Marisaldi, I. G. Mitrofanov, T. Murakami, M. Ohno, D. M. Palmer, A. B. Sanin, R. Starr, D. Svinkin, T. Takahashi, M. Tashiro, Y. Terada, and K. Yamaoka
2012. Inverse Compton X-Ray Emission from Supernovae with Compact Progenitors: Application to SN2011fe. ApJ, 751:134.

Marietta, E., A. Burrows, and B. Fryxell
2000. Type IA Supernova Explosions in Binary Systems: The Impact on the Secondary Star and Its Consequences. ApJS, 128:615–650.

Marion, G. H., P. J. Brown, J. Vinkó, J. M. Silverman, D. J. Sand, P. Challis, R. P. Kirshner, J. C. Wheeler, P. Berlind, W. R. Brown, M. L. Calkins, Y. Camacho, G. Dhungana, R. J. Foley, A. S. Friedman, M. L. Graham, D. A. Howell, E. Y. Hsiao, J. M. Irwin, S. W. Jha, R. Kehoe, L. M. Macri, K. Maeda, K. Mandel, C. McCully, V. Pandya, K. J. Rines, S. Wilhelmy, and W. Zheng
2016. SN˜2012cg: Evidence for Interaction Between a Normal Type Ia Supernova and a Non-degenerate Binary Companion. ApJ, 820:92.

Matheson, T., A. V. Filippenko, R. Chornock, D. C. Leonard, and W. Li
2000. Helium Emission Lines in the Type IC Supernova 1999CQ. AJ, 119:2303–2310.

Mattila, S., P. Lundqvist, J. Sollerman, C. Kozma, E. Baron, C. Fransson, B. Leibundgut, and K. Nomoto
2005. Early and late time VLT spectroscopy of SN 2001el - progenitor constraints for a type Ia supernova. A&A, 443:649–662.

Milisavljevic, D., R. Margutti, A. Kamble, D. J. Patnaude, J. C. Raymond, J. J. Eldridge, W. Fong, M. Bietenholz, P. Challis, R. Chornock, M. R. Drout, C. Fransson, R. A. Fesen, J. E. Grindlay, R. P. Kirshner, R. Lunnan, J. Mackey, G. F. Miller, J. T. Parrent, N. E.

Sanders, A. M. Soderberg, and B. A. Zauderer
2015. Metamorphosis of SN 2014C: Delayed Interaction between a Hydrogen Poor Core-collapse Supernova and a Nearby Circumstellar Shell. ApJ, 815:120.

Miller, A. A., Y. Cao, A. L. Piro, N. Blagorodnova, B. D. Bue, S. B. Cenko, S. Dhawan, R. Ferretti, O. D. Fox, C. Fremling, A. Goobar, D. A. Howell, G. Hosseinzadeh, M. M. Kasliwal, R. R. Laher, R. Lunnan, F. J. Masci, C. McCully, P. E. Nugent, J. Sollerman, F. Taddia, and S. R. Kulkarni
2018. Early Observations of the Type Ia Supernova iPTF 16abc: A Case of Interaction with Nearby, Unbound Material and/or Strong Ejecta Mixing. ApJ, 852:100.

Minkowski, R.
1941. Spectra of Supernovae. PASP, 53:224.

Moore, K. and L. Bildsten
2012. Circumstellar Shell Formation in Symbiotic Recurrent Novae. ApJ, 761:182.

Noebauer, U. M., M. Kromer, S. Taubenberger, P. Baklanov, S. Blinnikov, E. Sorokina, and W. Hillebrandt
2017. Early light curves for Type Ia supernova explosion models. MNRAS, 472:2787–2799.

Nugent, P., M. Phillips, E. Baron, D. Branch, and P. Hauschildt
1995. Evidence for a Spectroscopic Sequence among Type 1a Supernovae. ApJ, 455:L147.

Nugent, P. E., M. Sullivan, S. B. Cenko, R. C. Thomas, D. Kasen, D. A. Howell, D. Bersier, J. S. Bloom, S. R. Kulkarni, M. T. Kandrashoff, A. V. Filippenko, J. M. Silverman, G. W. Marcy, A. W. Howard, H. T. Isaacson, K. Maguire, N. Suzuki, J. E. Tarlton, Y.-C. Pan, L. Bildsten, B. J. Fulton, J. T. Parrent, D. Sand, P. Podsiadlowski, F. B. Bianco, B. Dilday, M. L. Graham, J. Lyman, P. James, M. M. Kasliwal, N. M. Law, R. M. Quimby, I. M. Hook, E. S. Walker, P. Mazzali, E. Pian, E. O. Ofek, A. Gal-Yam, and D. Poznanski
2011. Supernova SN 2011fe from an exploding carbon-oxygen white dwarf star. Nature, 480:344–347.

O'Brien, T. J., M. F. Bode, and F. D. Kahn
1992. Models for the remnants of recurrent novae. III - Comparison with the X-ray observations of RS Ophiuchi (1985). MNRAS, 255:683–693.

Olling, R. P., R. Mushotzky, E. J. Shaya, A. Rest, P. M. Garnavich, B. E. Tucker, D. Kasen, S. Margheim, and A. V. Filippenko
2015. No signature of ejecta interaction with a stellar companion in three type Ia supernovae. Nature, 521:332–335.

Panagia, N.
1985. Multifrequency observations of recent supernovae. In *Supernovae as Distance Indicators*, N. Bartel, ed., volume 224 of *Lecture Notes in Physics, Berlin Springer Verlag*, Pp. 14–33.

Panagia, N., S. D. Van Dyk, K. W. Weiler, R. A. Sramek, C. J. Stockdale, and K. P. Murata
2006. A Search for Radio Emission from Type Ia Supernovae. ApJ, 646:369–377.

Parrent, J. T., D. A. Howell, B. Friesen, R. C. Thomas, R. A. Fesen, D. Milisavljevic, F. B. Bianco, B. Dilday, P. Nugent, E. Baron, I. Arcavi, S. Ben-Ami, D. Bersier, L. Bildsten, J. Bloom, Y. Cao, S. B. Cenko, A. V. Filippenko, A. Gal-Yam, M. M. Kasliwal, N. Konidaris, S. R. Kulkarni, N. M. Law, D. Levitan, K. Maguire, P. A. Mazzali, E. O. Ofek, Y. Pan, D. Polishook, D. Poznanski, R. M. Quimby, J. M. Silverman, A. Sternberg, M. Sullivan, E. S. Walker, D. Xu, C. Buton, and R. Pereira
2012. Analysis of the Early-time Optical Spectra of SN 2011fe in M101. ApJ, 752:L26.

Pastorello, A., S. J. Smartt, S. Mattila, J. J. Eldridge, D. Young, K. Itagaki, H. Yamaoka, H. Navasardyan, S. Valenti, F. Patat, I. Agnoletto, T. Augusteijn, S. Benetti, E. Cappellaro, T. Boles, J.-M. Bonnet-Bidaud, M. T. Botticella, F. Bufano, C. Cao, J. Deng, M. Dennefeld, N. Elias-Rosa, A. Harutyunyan, F. P. Keenan, T. Iijima, V. Lorenzi, P. A. Mazzali, X. Meng, S. Nakano, T. B. Nielsen, J. V. Smoker, V. Stanishev, M. Turatto, D. Xu, and L. Zampieri
2007. A giant outburst two years before the core-collapse of a massive star. Nature, 447:829–832.

Patat, F., P. Chandra, R. Chevalier, S. Justham, P. Podsiadlowski, C. Wolf, A. Gal-Yam, L. Pasquini, I. A. Crawford, P. A. Mazzali, A. W. A. Pauldrach, K. Nomoto, S. Benetti, E. Cappellaro, N. Elias-Rosa, W. Hillebrandt, D. C. Leonard, A. Pastorello, A. Renzini, F. Sabbadin, J. D. Simon, and M. Turatto
2007. Detection of Circumstellar Material in a Normal Type Ia Supernova. *Science*, 317:924.

Patat, F., N. N. Chugai, P. Podsiadlowski, E. Mason, C. Melo, and L. Pasquini
2011. Connecting RS Ophiuchi to [some] type Ia supernovae. A&A, 530:A63.

Pérez-Torres, M. A., P. Lundqvist, R. J. Beswick, C. I. Björnsson, T. W. B. Muxlow, Z. Paragi, S. Ryder, A. Alberdi, C. Fransson, J. M. Marcaide, I. Martí-Vidal, E. Ros, M. K. Argo, and J. C. Guirado
2014. Constraints on the Progenitor System and the Environs of SN 2014J from Deep Radio Observations. ApJ, 792:38.

Perrott, Y. C., A. M. M. Scaife, D. A. Green, M. L. Davies, T. M. O. Franzen, K. J. B. Grainge, M. P. Hobson, N. Hurley-Walker, A. N. Lasenby, M. Olamaie, G. G. Pooley, C. Rodríguez-Gonzálvez, C. Rumsey, R. D. E. Saunders, M. P. Schammel, P. F. Scott, T. W. Shimwell, D. J. Titterington, E. M. Waldram, and AMI Consortium
2013. AMI Galactic Plane Survey at 16 GHz - I. Observing, mapping and source extraction. MNRAS, 429:3330–3340.

Phillips, M. M.
1993. The absolute magnitudes of Type IA supernovae. ApJ, 413:L105–L108.

Phillips, M. M., L. A. Wells, N. B. Suntzeff, M. Hamuy, B. Leibundgut, R. P. Kirshner, and C. B. Foltz
1992. SN 1991T - Further evidence of the heterogeneous nature of type IA supernovae. AJ, 103:1632–1637.

Piro, A. L. and V. S. Morozova
2016. Exploring the Potential Diversity of Early Type Ia Supernova Light Curves. ApJ, 826:96.

Podsiadlowski, P., J. J. L. Hsu, P. C. Joss, and R. R. Ross
1993. The progenitor of supernova 1993J - A stripped supergiant in a binary system? Nature, 364:509–511.

Raskin, C. and D. Kasen
2013. Tidal Tail Ejection as a Signature of Type Ia Supernovae from White Dwarf Mergers. ApJ, 772:1.

Roth, N. and D. Kasen
2015. Monte Carlo Radiation-Hydrodynamics With Implicit Methods. ApJS, 217:9.

Rybicki, G. B. and A. P. Lightman
1979. *Radiative processes in astrophysics*.

Sana, H., S. E. de Mink, A. de Koter, N. Langer, C. J. Evans, M. Gieles, E. Gosset, R. G. Izzard, J.-B. Le Bouquin, and F. R. N. Schneider
2012. Binary Interaction Dominates the Evolution of Massive Stars. *Science*, 337:444.

Sand, D. J., M. L. Graham, J. Botyánszki, D. Hiramatsu, C. McCully, S. Valenti, G. Hosseinzadeh, D. A. Howell, J. Burke, R. Cartier, T. Diamond, E. Y. Hsiao, S. W. Jha, D. Kasen, S. Kumar, G. H. Marion, N. Suntzeff, L. Tartaglia, C. Wheeler, and S. Wyatt
2018. Nebular Spectroscopy of the 'Blue Bump' Type Ia Supernova 2017cbv. *ArXiv e-prints*.

Schlegel, E. M.
1990. A new subclass of Type II supernovae? MNRAS, 244:269–271.

Shappee, B. J., A. L. Piro, K. Z. Stanek, S. G. Patel, R. A. Margutti, V. M. Lipunov, and R. W. Pogge
2018. Strong Evidence against a Non-degenerate Companion in SN 2012cg. ApJ, 855:6.

Shappee, B. J., K. Z. Stanek, R. W. Pogge, and P. M. Garnavich
2013. No Stripped Hydrogen in the Nebular Spectra of Nearby Type Ia Supernova 2011fe. ApJ, 762:L5.

Shen, K. J. and K. Moore
2014. The Initiation and Propagation of Helium Detonations in White Dwarf Envelopes. ApJ, 797:46.

Silverman, J. M., P. E. Nugent, A. Gal-Yam, M. Sullivan, D. A. Howell, A. V. Filippenko, I. Arcavi, S. Ben-Ami, J. S. Bloom, S. B. Cenko, Y. Cao, R. Chornock, K. I. Clubb, A. L. Coil, R. J. Foley, M. L. Graham, C. V. Griffith, A. Horesh, M. M. Kasliwal, S. R. Kulkarni, D. C. Leonard, W. Li, T. Matheson, A. A. Miller, M. Modjaz, E. O. Ofek, Y.-C. Pan, D. A. Perley, D. Poznanski, R. M. Quimby, T. N. Steele, A. Sternberg, D. Xu, and O. Yaron
2013a. Type Ia Supernovae Strongly Interacting with Their Circumstellar Medium. ApJS, 207:3.

Silverman, J. M., P. E. Nugent, A. Gal-Yam, M. Sullivan, D. A. Howell, A. V. Filippenko, Y.-C. Pan, S. B. Cenko, and I. M. Hook
2013b. Late-time Spectral Observations of the Strongly Interacting Type Ia Supernova PTF11kx. ApJ, 772:125.

Silverman, J. M., J. Vinkó, G. H. Marion, J. C. Wheeler, B. Barna, T. Szalai, B. W. Mulligan, and A. V. Filippenko
2015. High-velocity features of calcium and silicon in the spectra of Type Ia supernovae. MNRAS, 451:1973–2014.

Simon, J. D., A. Gal-Yam, O. Gnat, R. M. Quimby, M. Ganeshalingam, J. M. Silverman, S. Blondin, W. Li, A. V. Filippenko, J. C. Wheeler, R. P. Kirshner, F. Patat, P. Nugent, R. J. Foley, S. S. Vogt, R. P. Butler, K. M. G. Peek, E. Rosolowsky, G. J. Herczeg, D. N. Sauer, and P. A. Mazzali
2009. Variable Sodium Absorption in a Low-extinction Type Ia Supernova. ApJ, 702:1157–1170.

Smartt, S. J.
2009. Progenitors of Core-Collapse Supernovae. ARA&A, 47:63–106.

Smith, N.
2016. Interacting Supernovae: Types IIn and Ibn. *ArXiv e-prints*.

Smith, N., C. D. Kilpatrick, J. C. Mauerhan, J. E. Andrews, R. Margutti, W.-F. Fong, M. L. Graham, W. Zheng, P. L. Kelly, A. V. Filippenko, and O. D. Fox
2017. Endurance of SN 2005ip after a decade: X-rays, radio and Hα like SN 1988Z require long-lived pre-supernova mass-loss. MNRAS, 466:3021–3034.

Soker, N.
2013. The Core-Degenerate Scenario for Type Ia Supernovae. In *Binary Paths to Type Ia Supernovae Explosions*, R. Di Stefano, M. Orio, and M. Moe, eds., volume 281 of *IAU Symposium*, Pp. 72–75.

Sramek, R. A., N. Panagia, and K. W. Weiler
1984. Radio emission from a type I supernova - SN 1983.51 IN NGC 5236. ApJ, 285:L59–L62.

Stathakis, R. A. and E. M. Sadler
1991. What was supernova 1988Z? MNRAS, 250:786–795.

Sternberg, A., A. Gal-Yam, J. D. Simon, F. Patat, W. Hillebrandt, M. M. Phillips, R. J. Foley, I. Thompson, N. Morrell, L. Chomiuk, A. M. Soderberg, D. Yong, A. L. Kraus, G. J. Herczeg, E. Y. Hsiao, S. Raskutti, J. G. Cohen, P. A. Mazzali, and K. Nomoto
2014. Multi-epoch high-spectral-resolution observations of neutral sodium in 14 Type Ia supernovae. MNRAS, 443:1849–1860.

Van Dyk, S. D., K. W. Weiler, M. J. Montes, R. A. Sramek, and N. Panagia
2000. Radio Supernovae and the Square Kilometer Array. In *Perspectives on Radio Astronomy: Science with Large Antenna Arrays*, M. P. van Haarlem, ed., P. 241.

van Hoof, P. A. M., R. J. R. Williams, K. Volk, M. Chatzikos, G. J. Ferland, M. Lykins, R. L. Porter, and Y. Wang
2014. Accurate determination of the free-free Gaunt factor - I. Non-relativistic Gaunt factors. MNRAS, 444:420–428.

Warren, J. S., J. P. Hughes, C. Badenes, P. Ghavamian, C. F. McKee, D. Moffett, P. P. Plucinsky, C. Rakowski, E. Reynoso, and P. Slane
2005. Cosmic-Ray Acceleration at the Forward Shock in Tycho's Supernova Remnant: Evidence from Chandra X-Ray Observations. ApJ, 634:376–389.

Wheeler, J. C. and R. P. Harkness
1986. Physical models of supernovae and the distance scale. In *NATO Advanced Science Institutes (ASI) Series C*, B. F. Madore and R. B. Tully, eds., volume 180 of *NATO Advanced Science Institutes (ASI) Series C*, Pp. 45–54.

Wood-Vasey, W. M., L. Wang, and G. Aldering
2004. Photometry of SN 2002ic and Implications for the Progenitor Mass-Loss History. ApJ, 616:339–345.

Zwart, J. T. L., R. W. Barker, P. Biddulph, D. Bly, R. C. Boysen, A. R. Brown, C. Clementson, M. Crofts, T. L. Culverhouse, J. Czeres, R. J. Dace, M. L. Davies, R. D'Alessandro, P. Doherty, K. Duggan, J. A. Ely, M. Felvus, F. Feroz, W. Flynn, T. M. O. Franzen, J. Geisbüsch, R. Génova-Santos, K. J. B. Grainge, W. F. Grainger, D. Hammett, R. E. Hills, M. P. Hobson, C. M. Holler, N. Hurley-Walker, R. Jilley, M. E. Jones, T. Kaneko, R. Kneissl, K. Lancaster, A. N. Lasenby, P. J. Marshall, F. Newton, O. Norris, I. Northrop, D. M. Odell, G. Petencin, J. C. Pober, G. G. Pooley, M. W. Pospieszalski, V. Quy, C. Rodríguez-Gonzálvez, R. D. E. Saunders, A. M. M. Scaife,

J. Schofield, P. F. Scott, C. Shaw, T. W. Shimwell, H. Smith, A. C. Taylor, D. J. Titterington, M. Velić, E. M. Waldram, S. West, B. A. Wood, G. Yassin, and AMI Consortium 2008. The Arcminute Microkelvin Imager. MNRAS, 391:1545–1558.